UNIVERSITÀ
DEGLI STUDI
DI PADOVA

Administrative Headquarters: University of Padua
Department of Engineering and Management (DTG)

DOCTORAL SCHOOL: INDUSTRIAL ENGINEERING
AREA: INDUSTRIAL PRODUCTION ENGINEERING
CYCLE: XXV

MICROSTRUCTURAL AND TECHNOLOGICAL OPTIMISATION OF MAGNESIUM ALLOYS

School Director: Ch.mo Prof. Paolo Colombo
Area Coordinator: Ch.mo Prof. Enrico Savio
Supervisor: Ch.mo Prof. Franco Bonollo

PhD Candidate: Nicola Facchinelli

Sommario

Il magnesio è uno degli elementi più presenti in natura ed è caratterizzato da una densità inferiore a quella dell'alluminio. Queste caratteristiche conferiscono grandi potenzialità alle leghe di magnesio, che quindi vengono impiegate in contesti particolari, quali ad esempio l'ambito militare e aerospaziale. Sebbene alcune leghe di magnesio, tra cui la AM60B, siano storicamente associate alla pressocolata, per tali applicazioni i componenti vengono realizzati attraverso il processo di colata in gravità, al fine di minimizzare il contenuto di difetti e conferire migliori caratteristiche meccaniche all'oggetto risultante. Proprio per il fatto che tale combinazione di lega e processo rappresenta una nicchia all'interno del panorama dei processi di fonderia, in letteratura si avverte la mancanza di contenuti specifici sulle potenzialità della lega AM60B colata in gravità. Ne consegue la volontà di contribuire a colmare tale lacuna, attraverso lo studio e l'innovazione del processo di colata in gravità di leghe leggere e, in particolare, di magnesio. A tal fine è stato analizzato l'intero processo, e con l'ausilio di software per la simulazione numerica del processo di colata ne sono state individuate le criticità e le variabili su cui intervenire per ottimizzarlo. I dati prodotti da tale analisi sono poi stati utilizzati per progettare e realizzare un impianto sperimentale, per la colata in gravità di leghe leggere da fonderia, in seguito utilizzato per la realizzazione di getti di riferimento aventi geometria a gradini, caratterizzati da peso e spessori tipici di alcune tipologie di componenti prodotti dall'industria aerospaziale. Con l'obiettivo di mettere in relazione i parametri di processo, la microstruttura risultante e le proprietà finali dei getti realizzabili attraverso tale processo, sono stati ricavati e analizzati numerosi campioni in lega di magnesio AM60B. Alle prove di trazione su provette ricavate da tali campioni sono seguite indagini metallografiche, con lo scopo di ottenere sia una caratterizzazione meccanica sia una caratterizzazione microstrutturale, relativamente ad ogni spessore dei getti e quindi in funzione delle diverse condizioni di raffreddamento. I dati così raccolti sono stati successivamente elaborati e confrontati con quelli risultanti dalla simulazione numerica dell'intero processo, permettendo di stabilire un modello previsionale delle caratteristiche finali, di getti in lega di magnesio AM60B colati in gravità, conoscendo solamente i parametri di processo. E' stato quindi formulato un protocollo operativo per la produzione, la caratterizzazione e la previsione delle proprietà finali di getti in lega leggera colati in gravità, adattabile a geometrie più complesse ed estendibile a livello industriale.

Summary

Magnesium is one of the most abundance element in nature, and it's characterised by a lower density than aluminium. These characteristics confer great potential to magnesium alloys, which are so used for specialised applications, like for military purposes and in the aerospace industry. While some magnesium alloys, including the AM60B alloy, are historically associated to high pressure die casting, for such applications the magnesium alloy components are usually produced by the gravity casting process, in order to minimise the defect's content and to achieve better castings' mechanical properties. Due to the fact that the combination of alloy and casting process represents a niche in the foundry processes panorama, in the literature there's a lack of specific contents regarding these issues. Hence the aim to fill the gap by studying these thematics and by looking for innovations in the gravity casting process of magnesium alloys. For these purposes, the overall process was analysed with the support of specific software for the numerical simulation of the casting process, to identify the process criticalities and the optimisable variables. The data so obtained were then used to design and build an experimental casting equipment, for foundry light alloys casting, which was subsequently used for the production of reference steps castings by gravity casting. The geometry of the die was designed considering the typical weight and thicknesses of the components produced by the aerospace industry. With the aim to establish a correlation between the process parameters, the resulting microstructure and the castings' final properties, several reference castings were produced by using an AM60B magnesium alloys, and then analysed. Static tensile tests and metallographic investigations were carried out on the specimens obtained from different thickness steps of these castings, and the data thus collected were subsequently processed and compared with those resulting from the numerical simulation of the whole casting process, allowing to establish a model to predict the castings' final properties by knowing only the process parameters. An operating protocol to produce, to characterise and to estimate the final properties of light alloy castings (produced by gravity casting process) was so defined. It can be used also to treat more complex geometries and it can be easily extended to industry.

Contents

Introduction

The history of elementary magnesium started in 1755, when Joseph Black, a Scottish chemist, discovered that magnesia contained a new element, magnesium. Black was unable to isolate this element.
The British chemist and scientist Sir Humphry Davy was honoured as the discover, because he isolated the metal in 1808 by electrolysis.
Then many other scientists were able to isolate the metal developing different production processes. Besides smaller attempts in some European countries, magnesium found steady interest only in Germany, which in 1868 was the only producer in the world, using the metal mostly as powder for pyrotechnical purposes.
During World War I (and even more during World War II) magnesium related activities and developments had a large growth. Several company and organizations built production plants, and in 1944 world capacity was estimated in 432,000 tons from 41 plants distributed in 13 countries.
In the post war period, production of magnesium decreased drastically. Magnesium industry attempted to develop different magnesium applications, but failed in the most part also because many of the other applications developed during the war could not be quickly converted to civilian uses. Large users of magnesium were Volkswagen for Beetle production and Samsonite for luggage improvement. Very technical uses of magnesium took place for aircrafts and rockets applications.

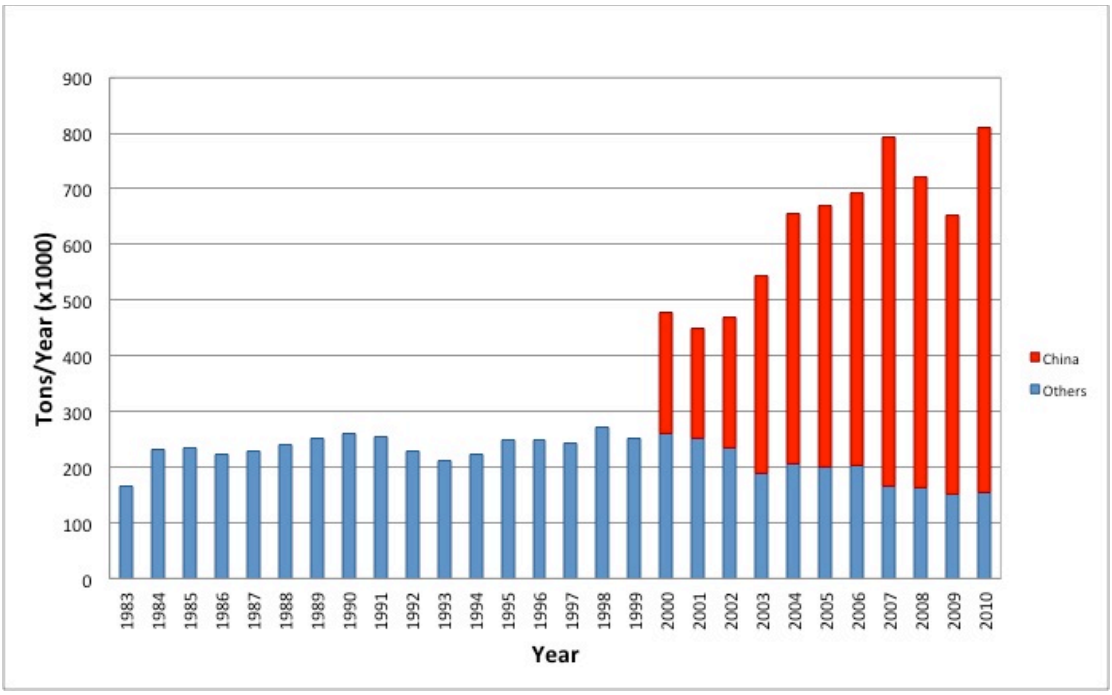

Figure 1 - Primary magnesium production trend in the last three decades [1]. Statistical methodology before 2000 excluded the Commonwealth of Independent States and the People's Republic of China.

In the recent years, die casting has been reported as the fastest growing segment of the magnesium industry (Figure 2). Magnesium die casting market is driven mainly by automotive applications [2, 3]. There is also certain growth in applications for the "3C" market (Communications, Computers and Cameras) and for handheld tools [4]. Introduction of the high-ductility energy absorbing alloys in the AM-series is a major driving force behind the expansion of the automotive use of the magnesium diecastings [5-9].

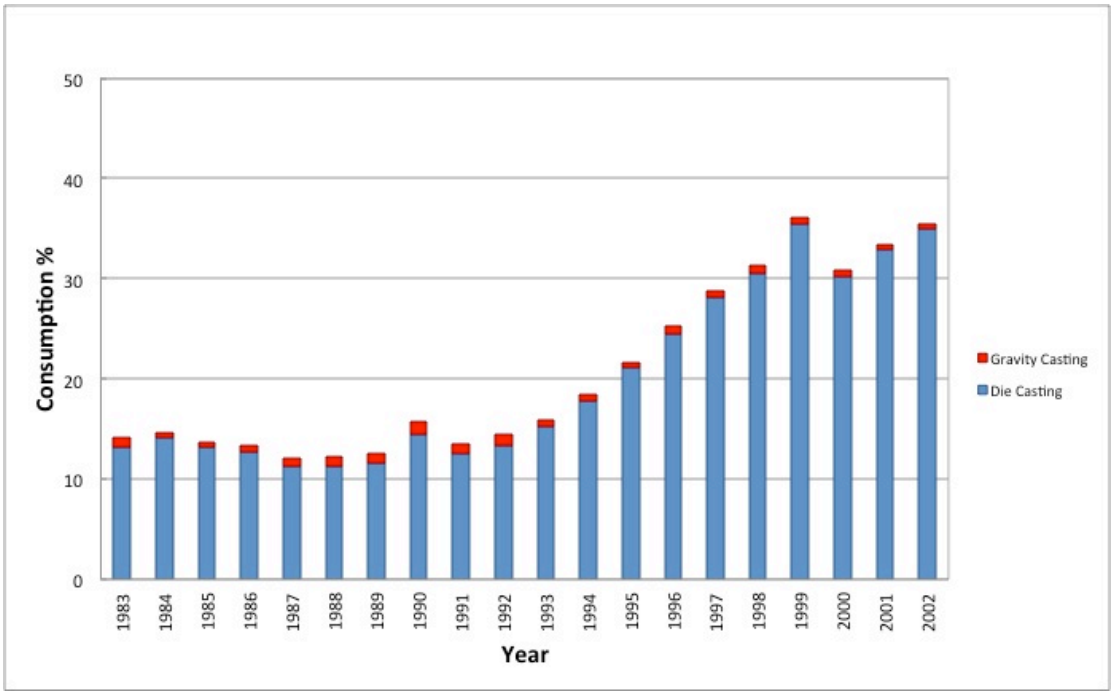

Figure 2 - Magnesium used by die casting and gravity die casting in the recent past [1].

Magnesium gravity casting has reported too an annual growth, not evident as for die casting but constant. The sand and permanent mould casting alloys are used for rather specialised applications. Racing wheels, engine blocks and certain parts for helicopters and aircraft constitute the majority of applications [10-12].
It is typically the low density of magnesium that leads to its initial consideration as a material of construction in consumer applications. Like most other metals, magnesium is almost never used in its pure form but it's alloyed to improve many of its properties [13]. The most common alloying elements are aluminium, zinc, manganese, silicon, zirconium, calcium, yttrium, silver, rare earth metals. The content of other elements like iron, copper and nickel must be strictly controlled to obtain quality magnesium castings. Aluminium is one of the most important alloying elements in magnesium [5]. Figure 3a shows the Mg-Al system focused on Mg side.

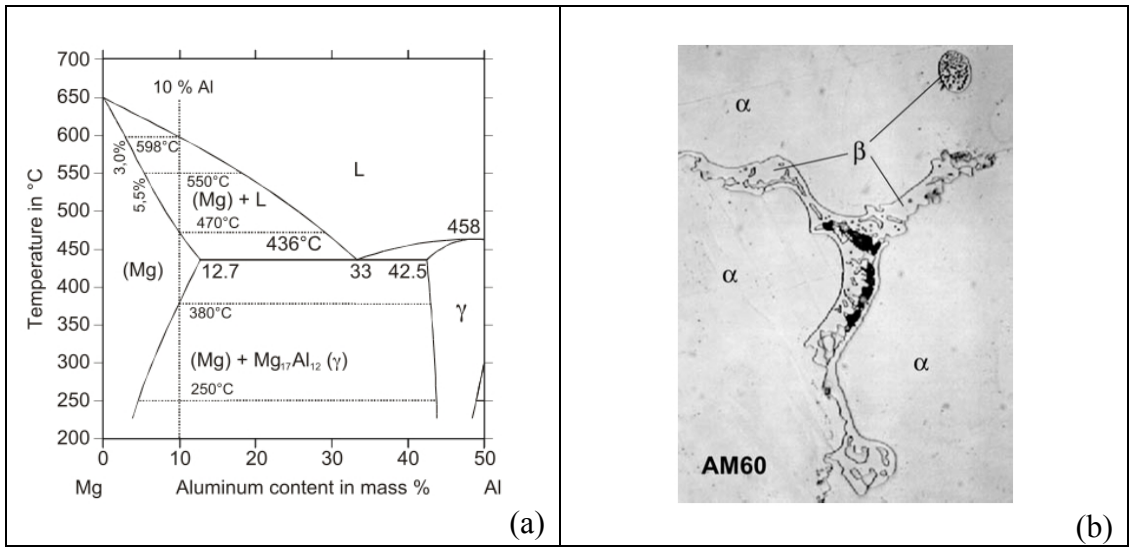

Figure 3 - (a) Magnesium-rich section of Mg-Al system and (b) α-Mg and β-$Mg_{17}Al_{12}$ in AM60 alloy [14].

Magnesium and aluminium are fully soluble in the liquid state, and the eutectic reaction takes place at 437°C, forming a mixture of α-Mg and β-$Mg_{17}Al_{12}$ (which is brittle), as illustrated in Figure 3b. The aluminium content in magnesium alloys also influences both grain size and ductility, as shown in Figure 4.

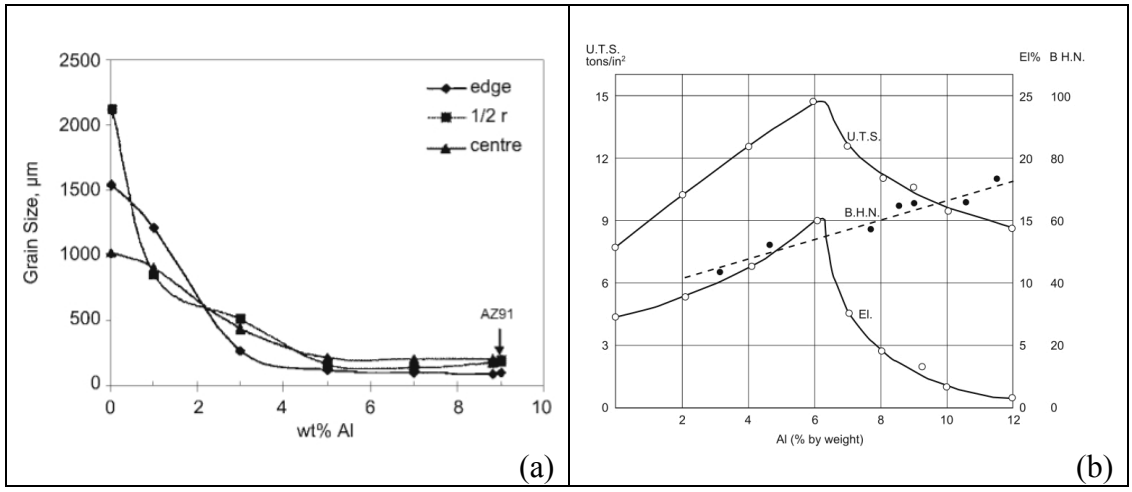

Figure 4 - Effect of aluminium content (a) on grain size [15] and (b) on ductility [16]. Alloys with high amounts of aluminium tends to become brittle.

As result, an AM60B magnesium alloy, which contains about 6 wt% Al, combines good grain refinement with a limited embrittling effect [17]. The AM60B alloy has outstanding ductility and energy absorbing properties combined with good strength and castability [18-20]. Typical uses are automotive seat frames, steering wheels, instrument panels, brackets, fans [21].

The AM60B alloy has historically been used with HPDC, but this process has some inherent drawbacks. Generally, the die filling speed is very high and therefore, the flow is very turbulent, with ingate velocities of 50 m/s and above. In conventional HPDC this produces castings with compressed gas inclusions, which cause porosity or blisters after heat treatment [22]. Porosity and inclusions affect the mechanical properties, which are so far below those acceptable for a given alloy [23].
To improve this situation, vacuum assisted HPDC and the more recent semisolid approach are under continuous development [24-32]. The excellence of HPDC lies in the possibility to cast large-size castings with thin walls, but not necessarily in highly loaded parts.
In addition there are some market niches that requires magnesium castings with high final quality. Aerospace and military applications, like helicopter and fighter planes parts, belong to this category. These parts need to be achieved through gravity casting process to minimise the defects content so ensuring best safety conditions.

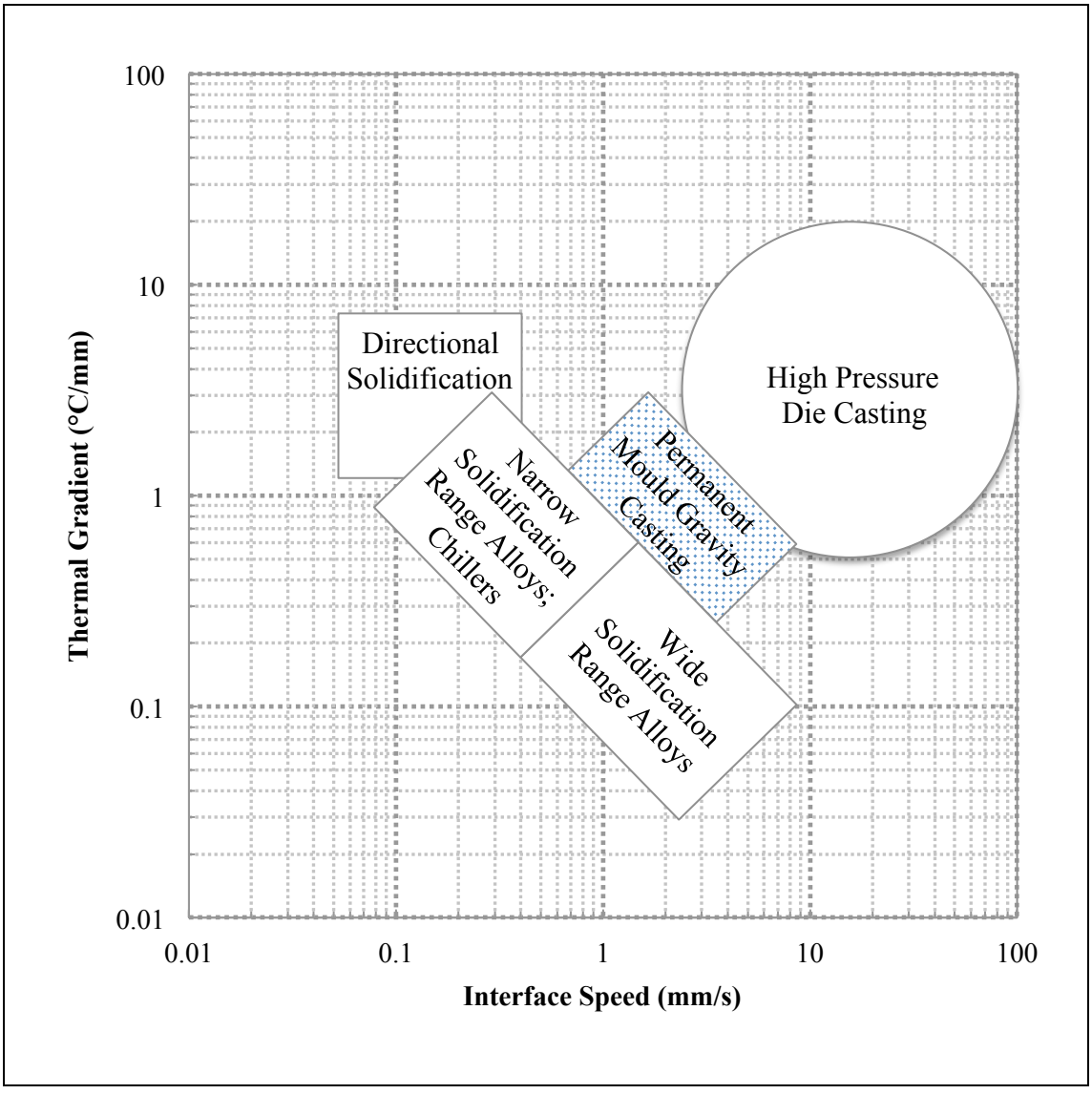

Figure 5 - Magnesium alloys casting processes contextualisation relatively to thermal gradient and interface speed.

Therefore it's very interesting to study the permanent mould gravity casting process of this alloy, that represents a niche in the magnesium casting processes panorama, with very different solidification conditions with respect to high pressure die casting (as visible in the graph in Figure 5), but not for this less important.
As confirmed also by the pie chart in Figure 6, die casting represents the area of greatest employment for this element (excluding the usage of magnesium as an element for producing aluminium alloys). Consequently in the literature is already available a large number of works regarding high pressure die casting process.

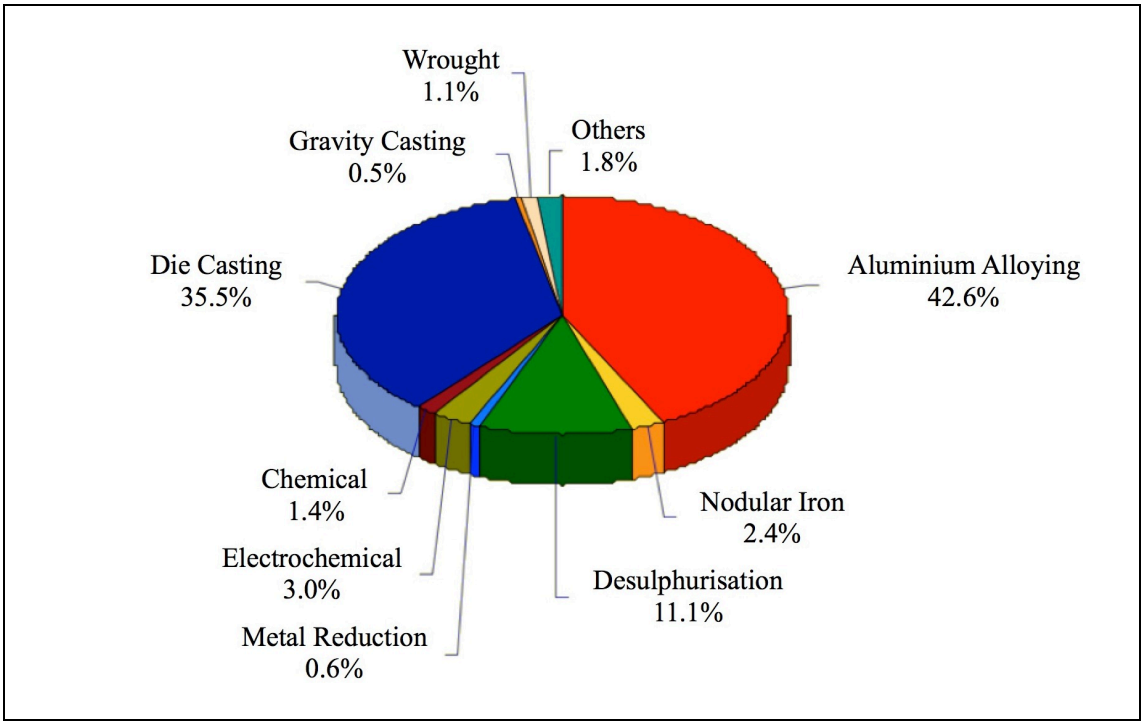

Figure 6 - Magnesium consumption in last years.

The scenario is very different regarding the gravity casting of magnesium alloys, that represents a minority with only the 0.5% of the overall consumption of magnesium.
It's possible to make a further comparison with the other processes' cooling conditions by looking at the scheme reported in Figure 7.

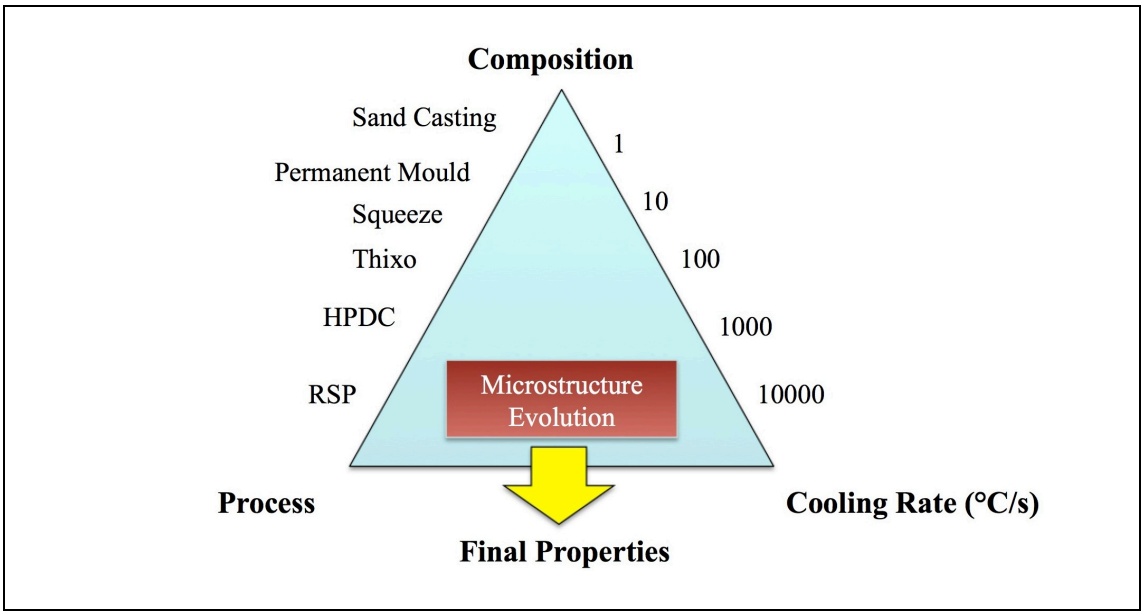

Figure 7 - Solidification in magnesium casting processes [33, 34].

This diagram shows the different cooling conditions belonging to the various casting processes. Permanent mould gravity casting process has typical cooling rates in the range of 1÷10 °C/s. It's precisely in this context, with this combination of thermal gradient and alloy (AM60B), that this study is focused.
In these conditions, as previously mentioned, are mainly produced components used for military and aerospace applications. Another reason, in addition to the magnesium lower density, is the cheaper fabrication with this castings process and the possibility to produce single items or small lots. Representative castings for these applications, that generally have weight between 0.5 kg and 2 kg, and thickness between 5 mm and 20 mm, can be viewed in Figure 8.

Figure 8 - Typical castings for aerospace applications.

It's thus interesting to analyse this type of process, to supply new relations between the cooling conditions and the final castings' properties, that could fill the literature's lack.

Objectives and Outline

The overall objective of this work is the research of improvements in magnesium alloys components performance, by focusing on the identification of the process criticalities and the optimisable variables, trying to establish reliable correlations between process parameters and microstructural characteristics.
Local microstructure is generally acknowledged to affect the potential mechanical properties of gravity die cast Mg alloys intended for structural applications. Varying the cooling conditions of solidifying metal, it is possible to change the solidification history of casting, thus obtaining different microstructures.
In order to study this relationship, a step casting geometry can be used, where the different thickness of the steps guarantees the different microstructural scale (Figure 9).

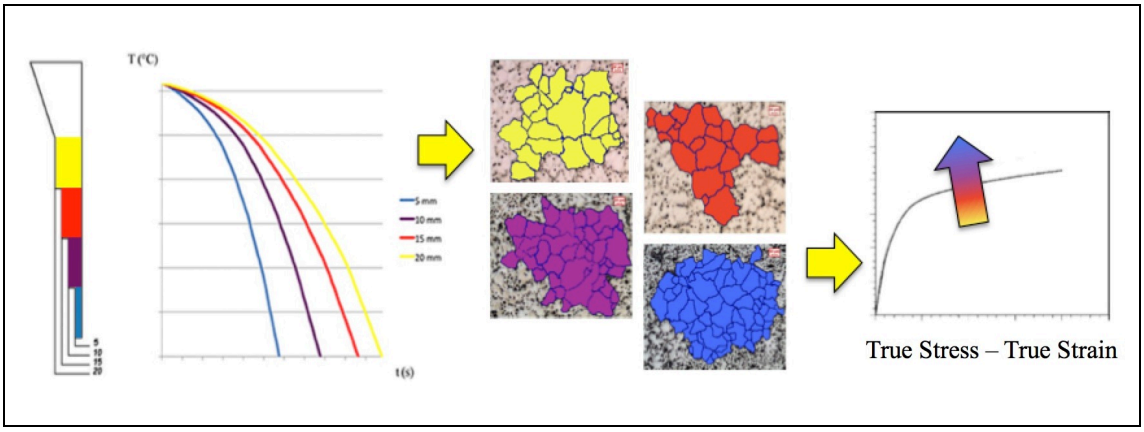

Figure 9 - Step die geometry

It's important, at this planning stage, to try to represent the real conditions in the best possible way. So the volume and the thickness of the die has been decided in function of the typical weight and geometry of the castings for aerospace industry (Figure 8).
Moreover, to ensure that the casting process leads to obtain sound reference castings, a further stage must be accomplished: the design of a specific mould for the gravity castings process of magnesium alloys.
Once produced reliable step castings, their characterisation will provide consistent data to be used for relate the process parameters to the castings' final properties.

Mould Design for Gravity Casting

Conventional gravity casting is still the most widely used method when relatively small numbers of castings must be produced or when there are specific needs. While perfectly adequate for many castings, this method has a number of drawbacks.

Gravity Die Casting

In gravity die casting the molten metal is poured directly from the crucible through air into a pouring bush and hence through a running and gating system into the cast shape (Figure 10a).

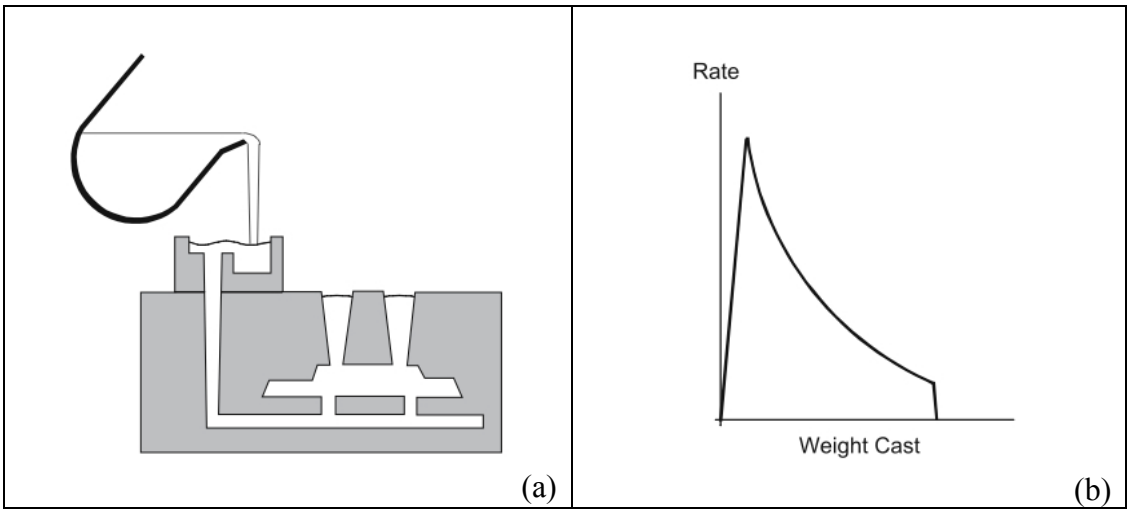

Figure 10 - (a) Pouring stage in gravity die casting: (b) fill rate defined by mould geometry.

The molten metal stream goes through several abrupt changes of direction, each of which can give rise to turbulence and possible formation of oxide inclusions or gas entrainment. Furthermore, the rate at which the casting fills is a function of the height difference between the pouring bush and the metal level in the mould (Figure 10b). Consequently, fill rate reduces towards the end of the cast. Where thin-sectioned castings are being poured, the reducing fill rate increases the difficulty of filling the thinnest sections.
This increases the complexity of mould and running system design to ensure good quality metal is fed adequately to all parts of the casting.

The Previous Reference Model

As mentioned before, varying the cooling conditions of solidifying metal it is possible to change the solidification history of casting, thus obtaining different microstructures. In order to study this relationship, reference moulds with step casting die geometry are usually employed (Figure 11a), where the different thickness of the steps guarantees the different microstructural scale (Figure 11b).

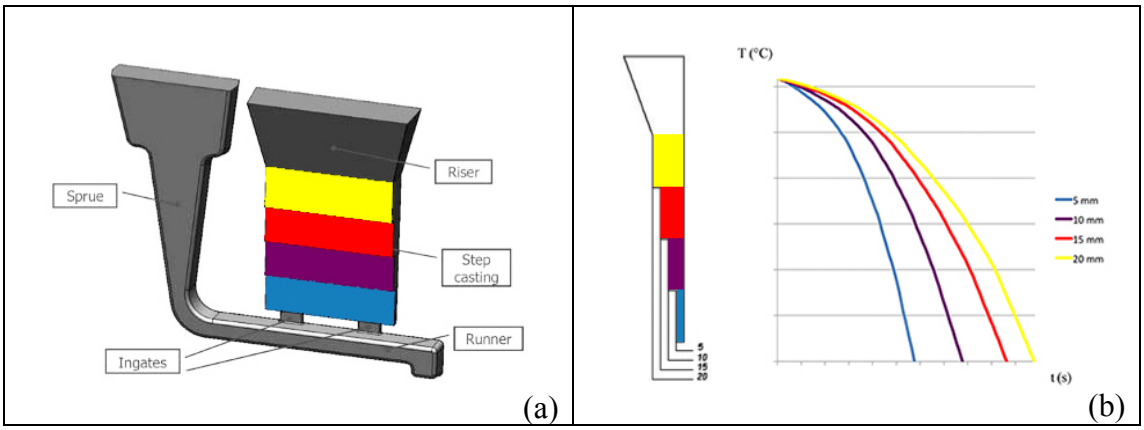

Figure 11 - (a) Typical reference casting and (b) related cooling conditions.

Recent studies [35, 36] have shown the correspondence between experimental results and numerical simulation predictions, allowing to consider these reference moulds reliable if used with aluminium alloys. For a number of reasons, the same can not be said for magnesium alloys [37].
In fact using the existing reference mould, designed for aluminium alloys, to produce AM60B magnesium step castings by gravity process, could lead to obtain results very different from what expected. Results of non-destructive testing (NDT) carried out on preliminary AM60B castings, produced using an existing step die cavity mould, are shown in Figure 12. The castings were analysed by means of a Bosello SRE 80 industrial machine equipped with a macrofocus X-ray set up at 70-100 kV and 0.20-0.80 A.

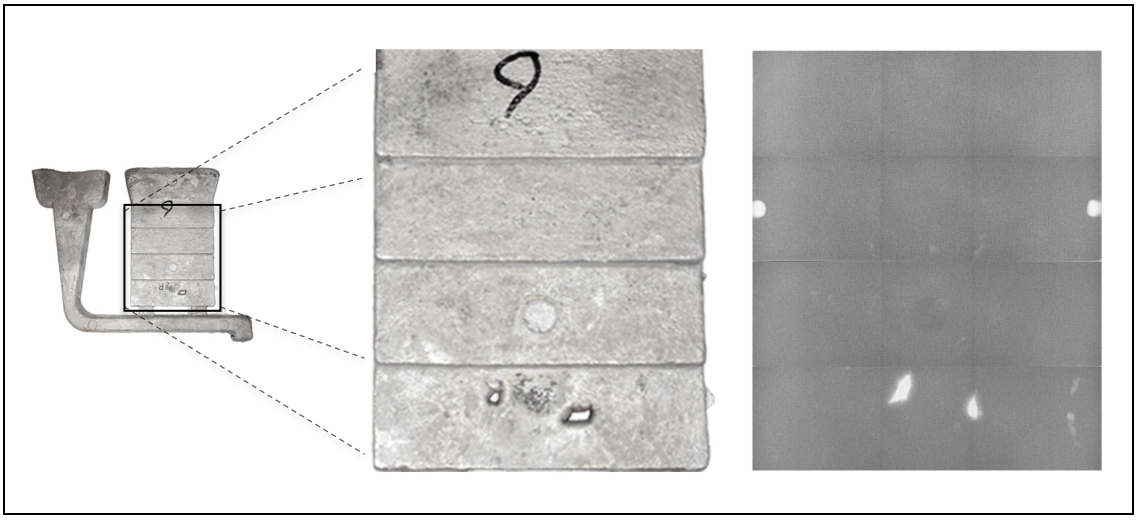

Figure 12 - Macro-focus X-ray image of an AM60B step casting obtained by the existing die, showing the presence of macro porosity in the thinnest step [38].

The qualitative results coming from the X-ray investigations reveal the presence of macro porosity, mainly located in the thinnest section (bottom step). Since mechanical

characteristics are strongly affected by the presence of defects it seems mandatory to minimise the defect content to obtain sound Mg alloy castings.
To design a new reference mould, specifically to be used with magnesium alloys, with the aim to optimise the whole casting process so getting reliable AM60B alloy castings, the first step is to understand the source and the cause of these casting defects.

Numerical Simulation

To do this, and to propose possible solutions, the numerical simulation approach was used to reproduce the casting process with the existing reference mould. Both the material and the die temperatures, and the filling parameters were analysed using Magma5 software v.5.1 (2011) from MAGMASOFT®. Basic governing equations of used simulation software are continuity equation, Navier-Stoke's equation, energy equation and volume of fluid (VoF) method for the free surface movement during the die filling [39]. The CAD model of the existing permanent mould was drawn and imported in the casting simulation software where a controlled volume mesh of 55,200,000 cells for the whole system (die and casting) and a mesh of 2,500,000 elements for the die cavity were automatically generated. The initial simulation parameters were setup to reproduce the casting process with the existing permanent mould, to individuate and understand the source and the causes of casting defects in order to propose possible solutions. Therefore, an AM60B alloy and a gravity manual pouring process were chosen from Magma5 internal database, as well as the other physical constants and properties of the die and the alloy, and their evolution with temperature, like the heat transfer coefficients (HTC) between alloy and mould and mould's walls. The molten alloy was set at 730°C and the mould preheating temperature at 350°C, as acquired from the casting process, to increase the reliability of numerical simulation. Virtual thermocouples were inserted in specific zones of the die, in order to control the temperatures profiles and to compare these values with the real ones, and were also inserted in die cavity to study the solidification evolution of the casting.
The shape of the castings obtained with the existing mould is shown in Figure 13, where the runner and the gating systems, the feeder and the pouring basin, are highlighted with different hues.

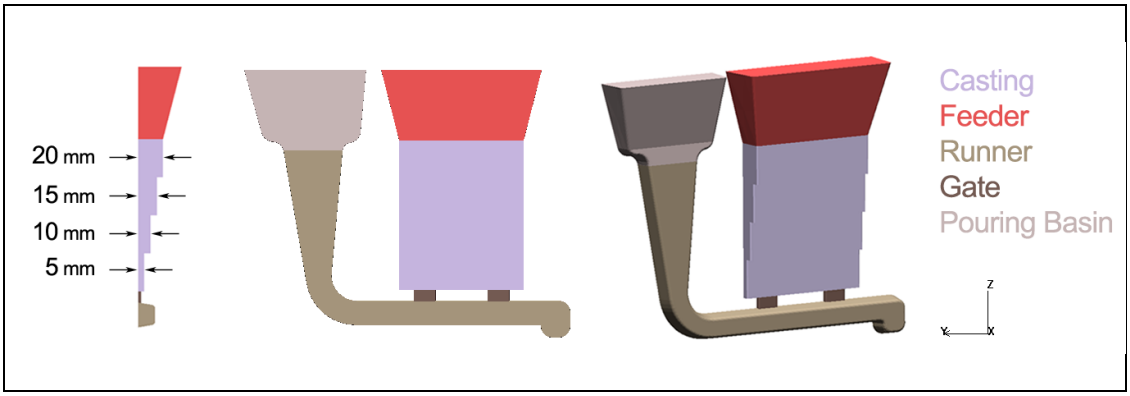

Figure 13 - The geometry of the existing casting [37].

Primarily, several filling issues were detected: the ingates' positions were not correctly designed and the path followed by the molten metal showed the presence of excessively turbulences in the thinnest step (Figure 14a), therefore producing "film-to-film" contact [40].

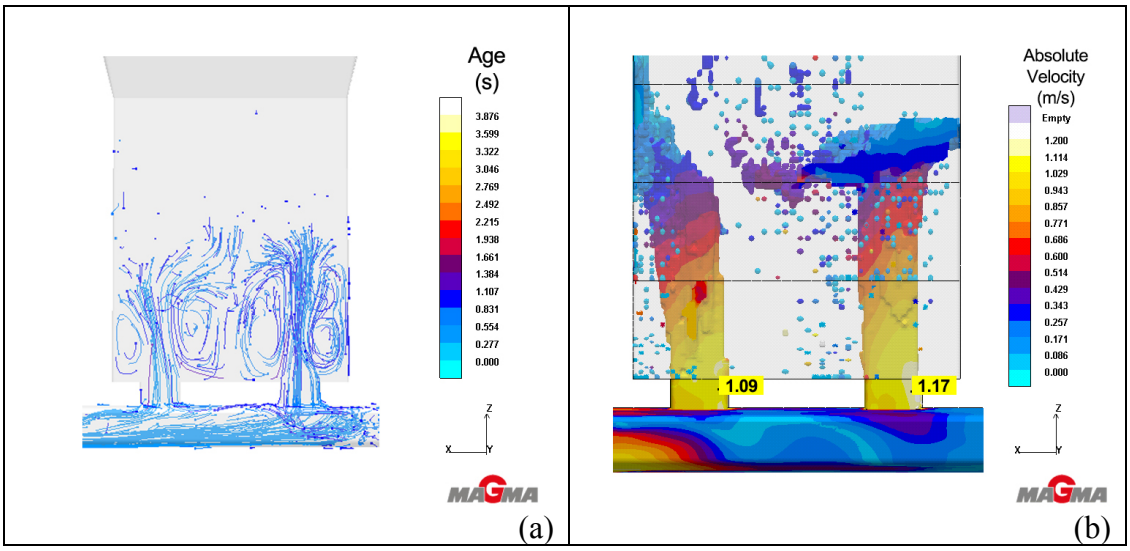

Figure 14 - (a) Metal flow at the ingates and (b) ingate velocities in the first mould [37].

Figure 14b shows the ingate speeds, that were higher than 1 m/s. Moreover, the non-returning trap at the end of the runner didn't work properly and the metal didn't remain trapped but returned back (Figure 15a).

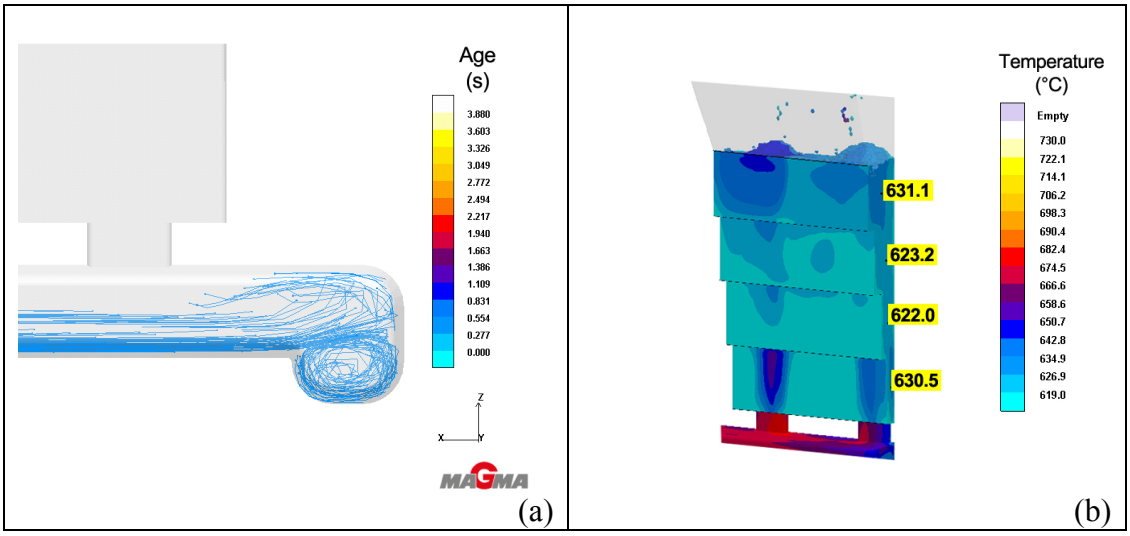

Figure 15 - (a) Metal flow in the non-return trap and (b) filling temperatures in the existing mould [37].

In the first design the molten metal temperatures were generally too low and the lowest were in the 10 mm and 15 mm steps (Figure 15b). Considering the whole

solidification process, the temperature gradient was not mainly directed from the thinnest to the thicker step and the solid fraction analysis confirmed this property (Figure 16a).

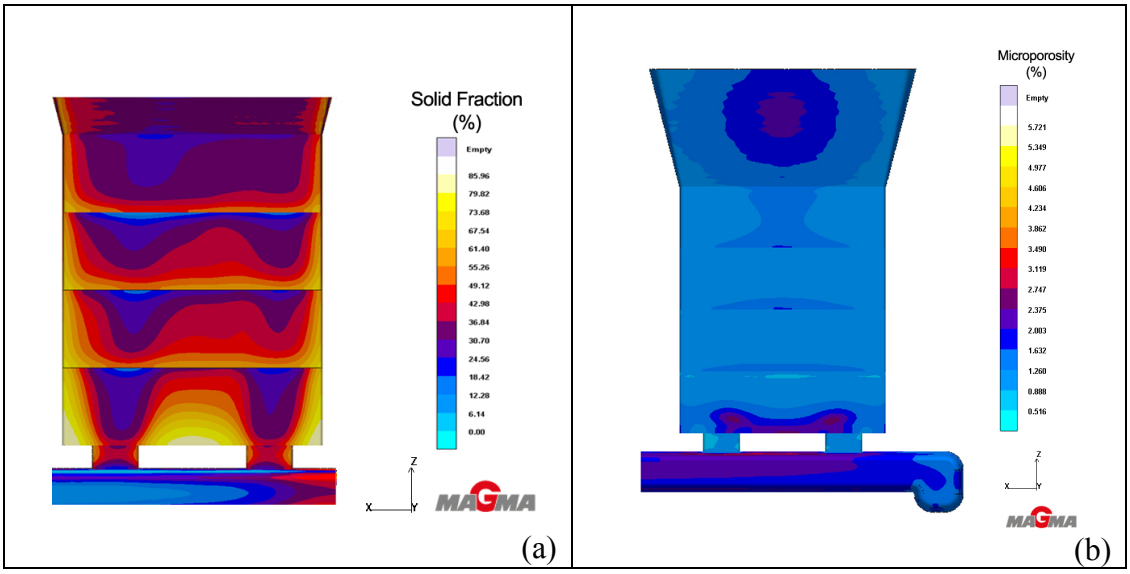

Figure 16 - (a) Measured solid fraction and (b) microporosity prediction for first mould [37].

Looking at local phenomena, the microporosity prediction (Figure 16b) let suppose to find high percentage of porosity in the thinnest step. That result is aligned with what observed firstly during the casting operations and then during NDT stage, so confirming the consistency of the numerical simulation.

Designing a Mould

Nevertheless to improve the overall casting process it isn't enough considering these encountered issues. Many aspects of the filling process and of the die cavity geometry must be considered designing a mould.

First essentials in making good quality magnesium casting are to ensure the casting is filled with the minimum of turbulence and that the gating system is designed to avoid or trap any entrained oxide or inclusions that may occur during pouring.

Synthetically, the features that should be contemplated during the design stage are outlined in Figure 17.

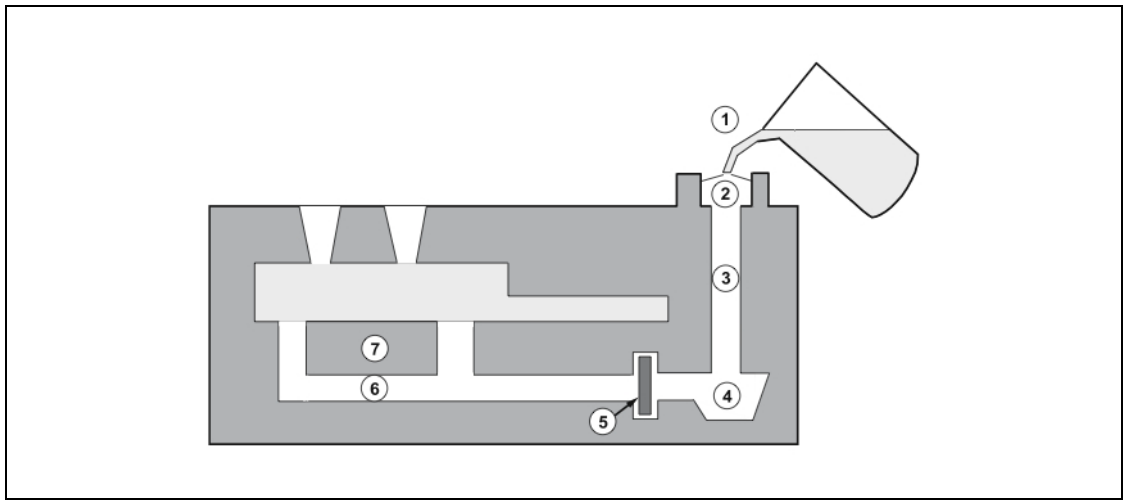

Figure 17 - Key factors for mould design [41].

As illustrated in Figure 17, the effective measures to be used are:
1) Pouring streams should be as short as possible and well protected to avoid development of thick oxide skins.
2) Pouring bushes should always be used to minimise the turbulent flow into the downsprue when the metal is poured.
3) Downsprues should be tapered with cross-sectional area at the bottom being less than the top, to ensures the sprue remains full throughout filling and avoids aspirating air. Rectangular sprues are preferable to round ones as they prevent vortex formation.
4) A well should be provided beneath the sprue to trap any drossy oxide from the start of pouring.
5) Filters can be incorporated in the running system. Most effective are knitted mild steel mesh pads or ceramic foam filters. Ceramic filters should be high Al_2O_3 or ZrO_2 and fully sintered to avoid reaction. In both cases, filters should be fitted in an enlarged section of the runner to avoid any choking effect. Even in well designed moulds, filters should be used because the melt may contain some unsettled oxides; moreover filters help to obtain a laminar flow through the gate.
6) Metal should be fed into the lowest section of the casting and allowed to rise up through the casting; cascading flow should be avoided.
7) Casting filling should be unpressurised, i.e., total cross sectional areas within the running system should decrease progressively from the casting entry to the downsprue. An ideal ratio is 1-2-3 for downsprue-runners-gates. All runners and gates should be smooth and generously radiused where possible.
After having ensured the delivering of clean metal to the casting, an adequate feeding of the die must be achieved, to promote optimum directional solidification so minimising micro-shrinkage [42].
Riser design is important for magnesium castings. The purpose of the riser is to supply liquid metal to feed the casting. They must therefore be the last portion of the casting to solidify. Ideally, the hottest metal should be supplied to the risers. However, this is not always possible in bottom-filled castings.

The Optimised Mould

The new permanent mould was designed considering all these aspects, with the help of the numerical simulation to study the filling and the solidification behaviour of the alloy by changing the die cavity geometry, in order to minimise the presence of defects. In Figure 18 is illustrated the geometry of the step casting obtainable with the new die, where the thickness sequence of the casting's steps was maintained as the existing die, and the runner system was completely redesigned.

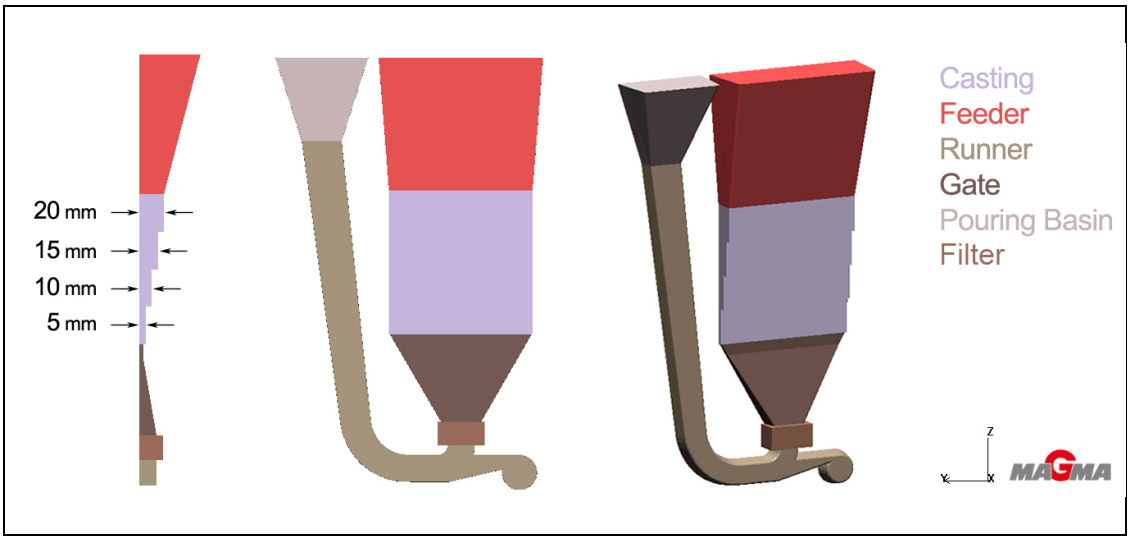

Figure 18 - Final geometry of the optimised step casting [37].

The optimised configuration provided several improvements if compared to the previous one. The running system section was measured according to Campbell's "10 rules of castings" for making sound and reliable castings [43, 44]. Only one gate was designed, to prevent eventually film-to-film contact during the filling stage [40]. Further, the non-returning trap was redesigned to avoid the metal return. A location to eventually set a foamed filter upstream the gate was designed in order to make the flow less turbulent as possible [45], and to make the metal speed at the gate to be in order of 0.4-0.6 m/s (Figure 19b). These are the most appropriate flow velocities to obtain a laminar flow, as indicated by Campbell [46].

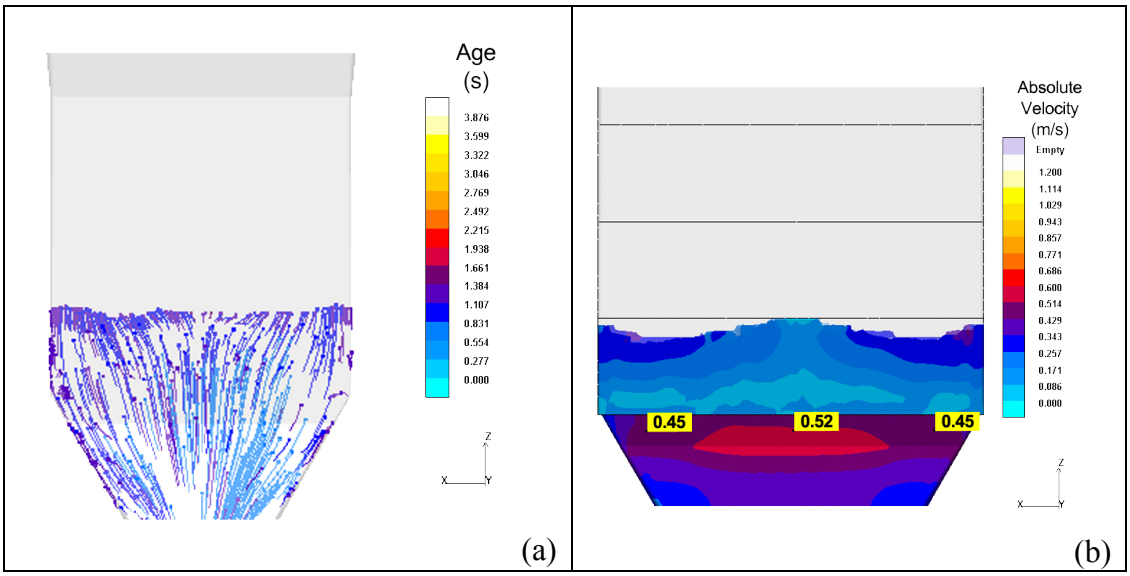

Figure 19 - Details of (a) metal flow at the ingate and (b) ingate velocities in the optimised die [37].

The new geometry, differently from the existing one, produces a desired temperature gradient [47], as shown in Figure 20b. The excessive speed of the metal at the ingates of the first die, and of course their configuration, produced the formation of turbulence inside the casting; the reviewed shape of the ingate and the addition of the filter made the flow to be as laminar as possible (Figure 19a). The trap present in the first mould didn't achieve the goal and the metal flow partially returned back [37]; differently the design of the new trap made the metal flow to fill it properly (Figure 20a), as confirmed by Campbell [41].

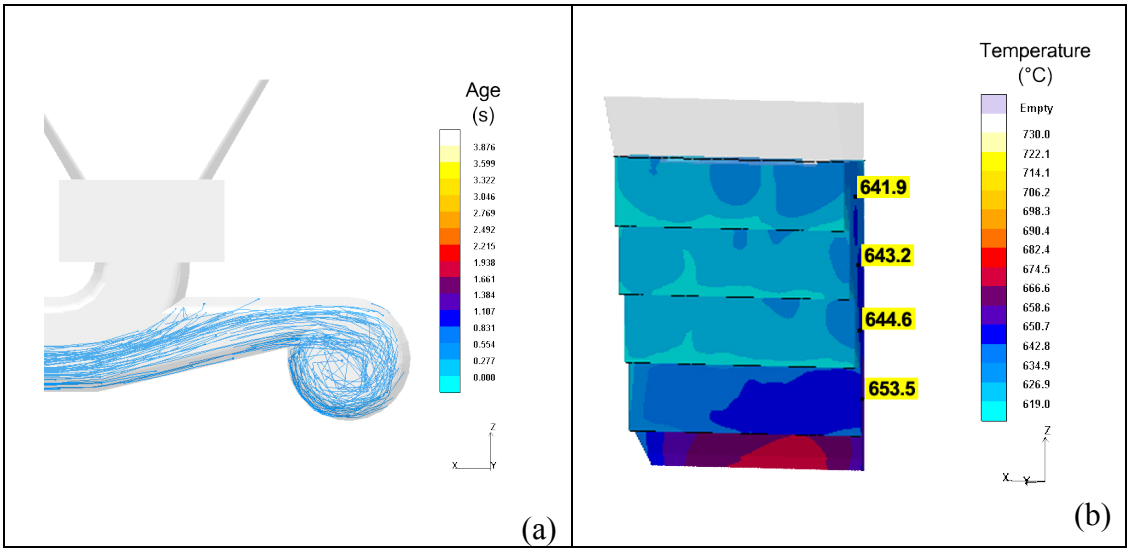

Figure 20 - (a) Metal flow in the non-return trap and (b) filling temperatures in the redesigned die [37].

The temperature gradient directed from the thinnest to the thicker step was obtained with the final configuration of the die. The analysis of the solid fraction gave further confirmation of this (Figure 21a). In order to individuate the presence and distribution of microshrinkage, microporosity prediction was analysed. Results are shown in Figure 21b.

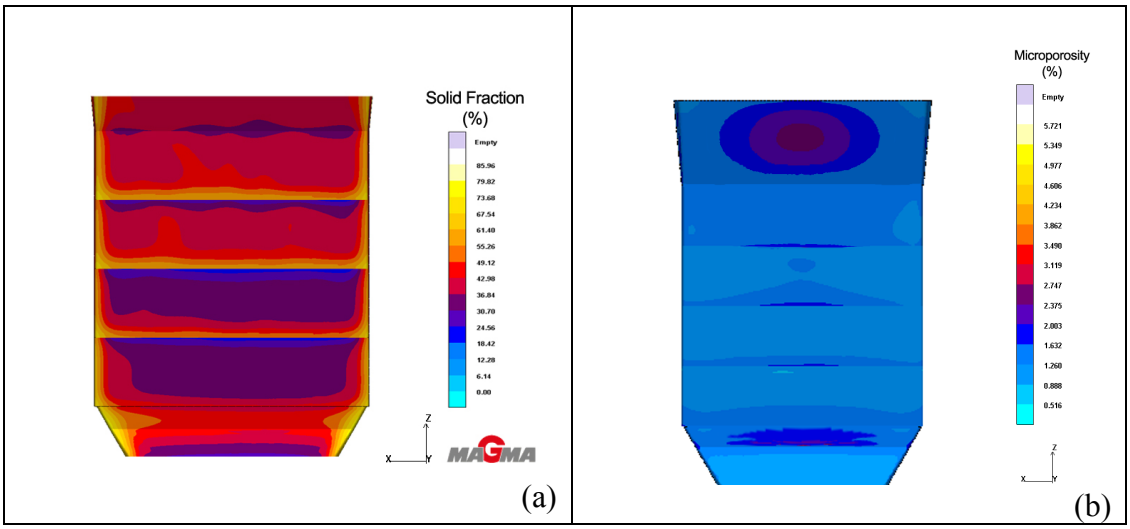

Figure 21 - Details of (a) calculated solid fraction and (b) microporosity prediction in the middle section of the casting obtained with the optimised die [37].

Differently from what evidenced by the same analysis on the existing permanent mould (Figure 16b), Figure 21b shows that the critical regions are located outside the casting, i.e. at the ingate and the feeder.
To prove the quality of the design work, the same non-destructive tests were performed on castings made by the new mould, and the results are visible in Figure 22.

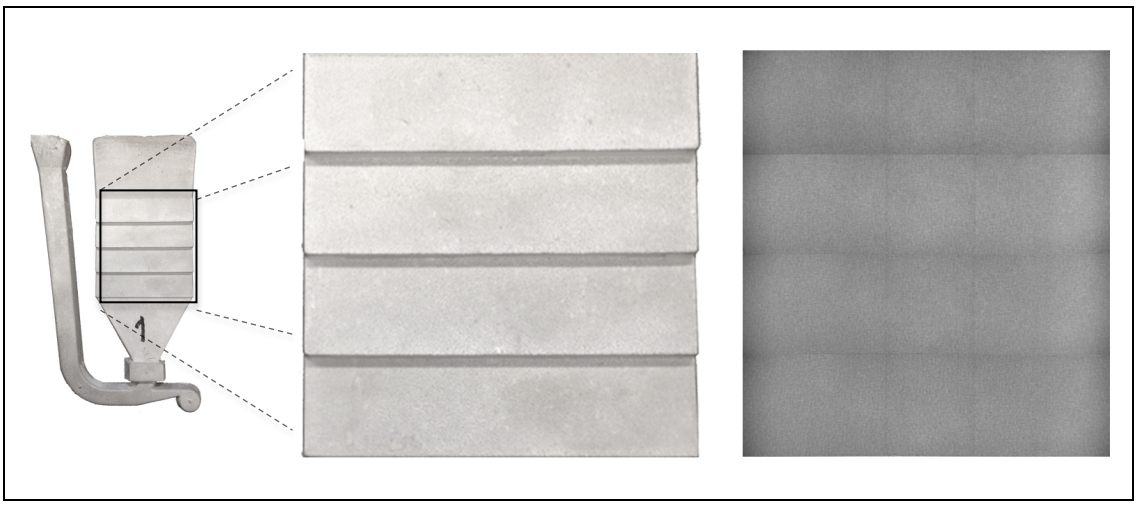

Figure 22 - Macro-focus X-ray image of a casting produced by using the optimised mould [38]. No macro defects have been detected.

In these castings there are no signs of appreciable inhomogeneity. The disappearance of macro porosity denotes with no doubt an improvement for final mechanical properties [48], and let suppose that the this mould can represent a new reference for study solidification phenomena on complex shape geometries.

The Casting Process

Using the optimised mould, two series of reference step geometry castings were produced, to study the relations between cooling conditions and both microstructural and mechanical properties.

Materials and Methods

The AM60B alloy used in this study (provided by Meridian Technologies) was in the form of ingots with a weight of 7 kg each.
The chemical composition of the "as-received" alloy was compared, after its use in the preliminary experiments, with the "as-cast" one to make sure that there was no significant variance in the composition due to the casting process to be used.
The Table 1 compares the chemical compositions of the AM60B magnesium alloy "as-received" with "as-cast" condition, verifying that both are according to ASTM B94 specifications.

Table 1 - Chemical composition of AM60B alloy used in the present research (wt.%). Comparison between "as-received" and "as-cast" conditions, and with ASTM data.

AM60B	Al	Zn	Mn	Si	Fe	Cu	Ni	Others	Mg
As-received	5.76	0.039	0.273	0.032	0.002	0.003	<0.001	<0.003	bal.
As-cast	5.76	0.0039	0.272	0.031	0.002	0.003	<0.001	<0.003	bal.
ASTM	5.5÷6.5	<0.22	>0.25	<0.10	<0.005	<0.01	<0.002	<0.003	bal.

The material, originally in the form of ingots, was cut into pieces and melt in an electric furnace, provided with a graphite crucible coated with boron nitride, to reduce the iron diffusion from the crucible to the alloy. The furnace was setup at 730°C and loaded with 4.5 Kg of alloy. The melt was protected from the environment atmosphere by a gas mixture composed of 0.5% SF_6 and 99.5% CO_2 (mol.%) to prevent magnesium reactions with the oxygen [49]. Periodically, the molten metal was manually skimmed and stirred with a coated paddle. The redesigned permanent mould (Figure 23a) was made by an AISI H11 tool steel and the die temperature was measured by K-type thermocouples inserted 5 mm under the surface of the die at three different locations (Figure 23b). This allowed a better control of the die temperature, in order to have a homogeneous temperature distribution throughout the die, in the range between 400 and 420°C, for all the experimental period.

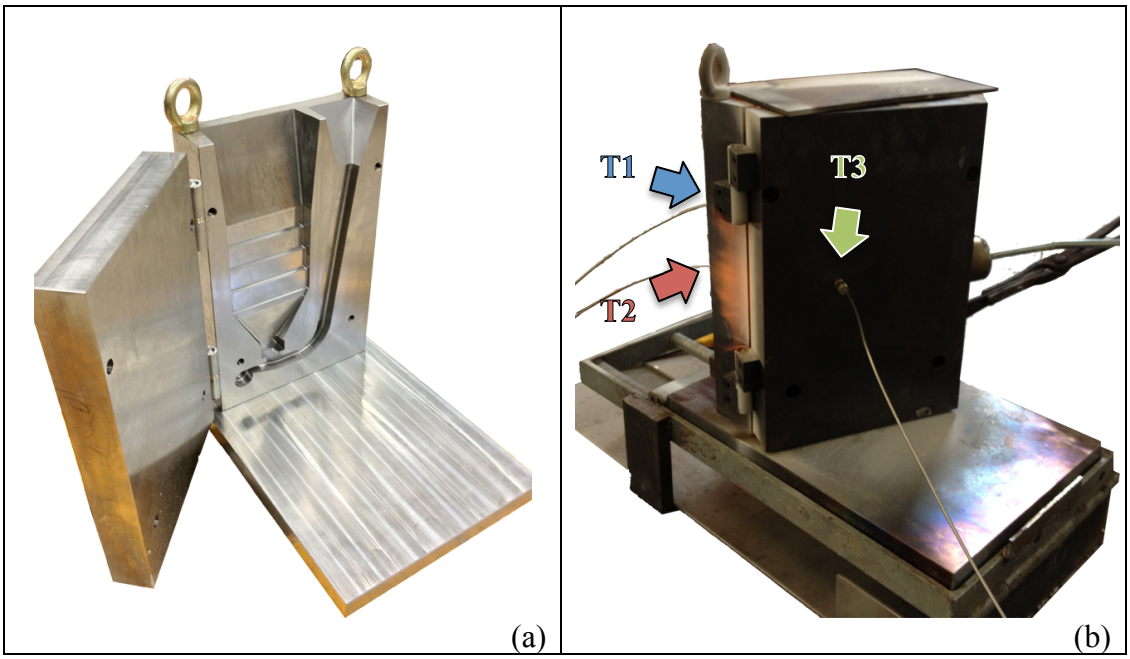

Figure 23 - (a) The optimised permanent mould and (b) the pre-heating stage of the die [38].

The casting process was cyclic and when the mould reached the desired temperature a ceramic foam filter was positioned upstream the gate, to trap oxide films and to make the flow less turbulent as possible [45], and the die was then closed. A preheated ladle was used to pour the molten metal into the pouring basin making a bottom filling of the die. The pouring time was about 4-5 seconds and the cycle time was about 8 minutes. The movable side of the die was then opened and the casting ejected with the help of extractors. The cycle restarted again eventually preceded by the die preheating to ensure the proper die temperature.

The Resulting Castings

Two casting campaigns have been executed. In the first one a 10 ppi ceramic foam filter has been used to minimise molten metal turbulence and to prevent non-metallic materials reaching the mould cavity. One of the castings obtained during the first production is shown in Figure 24.

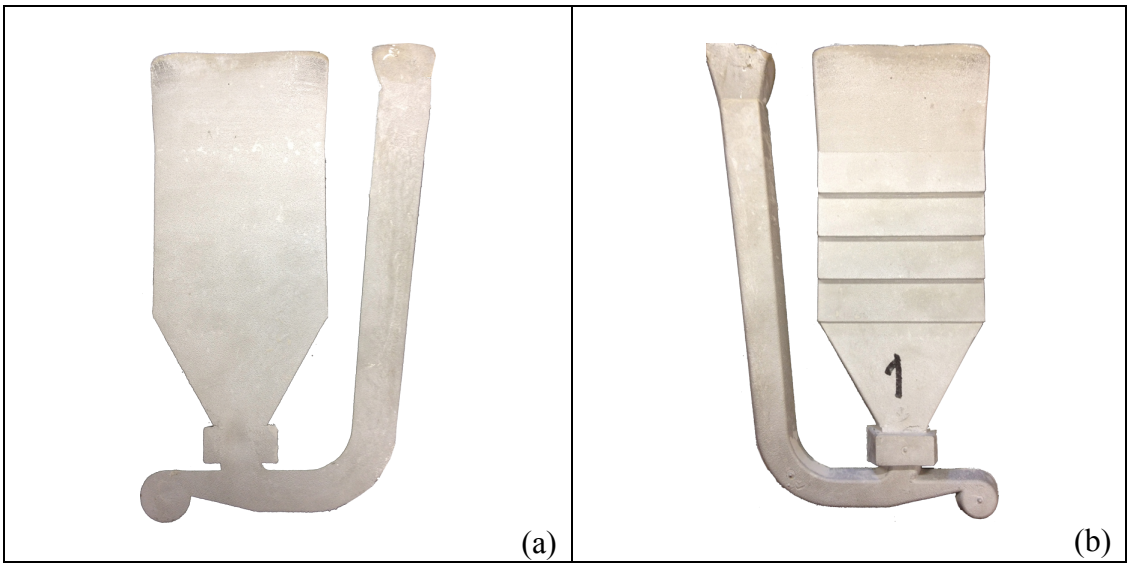

Figure 24 - Example of a step casting produced with the optimised die: (a) back and (b) front views [38].

Non-destructive testing have been performed on those castings, to evaluate their quality. The X-ray machine used in this work had a macrofocus that allows rougher analysis of the casting and a microfocus that allows instead to centre the analysis on a particular narrow zone of the observed casting.
This kind of analysis allows defects' detection through the variation of the density in the material. The denser areas appear darker than the ones with defects, so a gas porosity or a shrinkage are presented as clearer zones within a darker matrix.
This type of analysis can only provide a qualitative index of castings soundness: the small size defects are not visible, and defects like oxides are difficult to detect because of their density that is very similar to the density of the alloy. Inclusions some times are visible but only if with different density from the matrix or if enough big. The Bosello SRE80 machine has a resolution of the order of a tenth of a millimetre. Additionally, it has to be considered that a two dimensional image can contain overlaying defects.
In this survey, the parameters that were set in the machine are reported in Table 2, while the results of the X-ray investigation on the reference steps castings produced during the first casting campaign are reported in Figure 25.

Table 2 - X-Ray machine settings used during the investigation.

Step thickness (mm)	Voltage (KV)	Current (A)
20	53	0.80
15	49	0.80
10	45	0.80
5	40	0.80

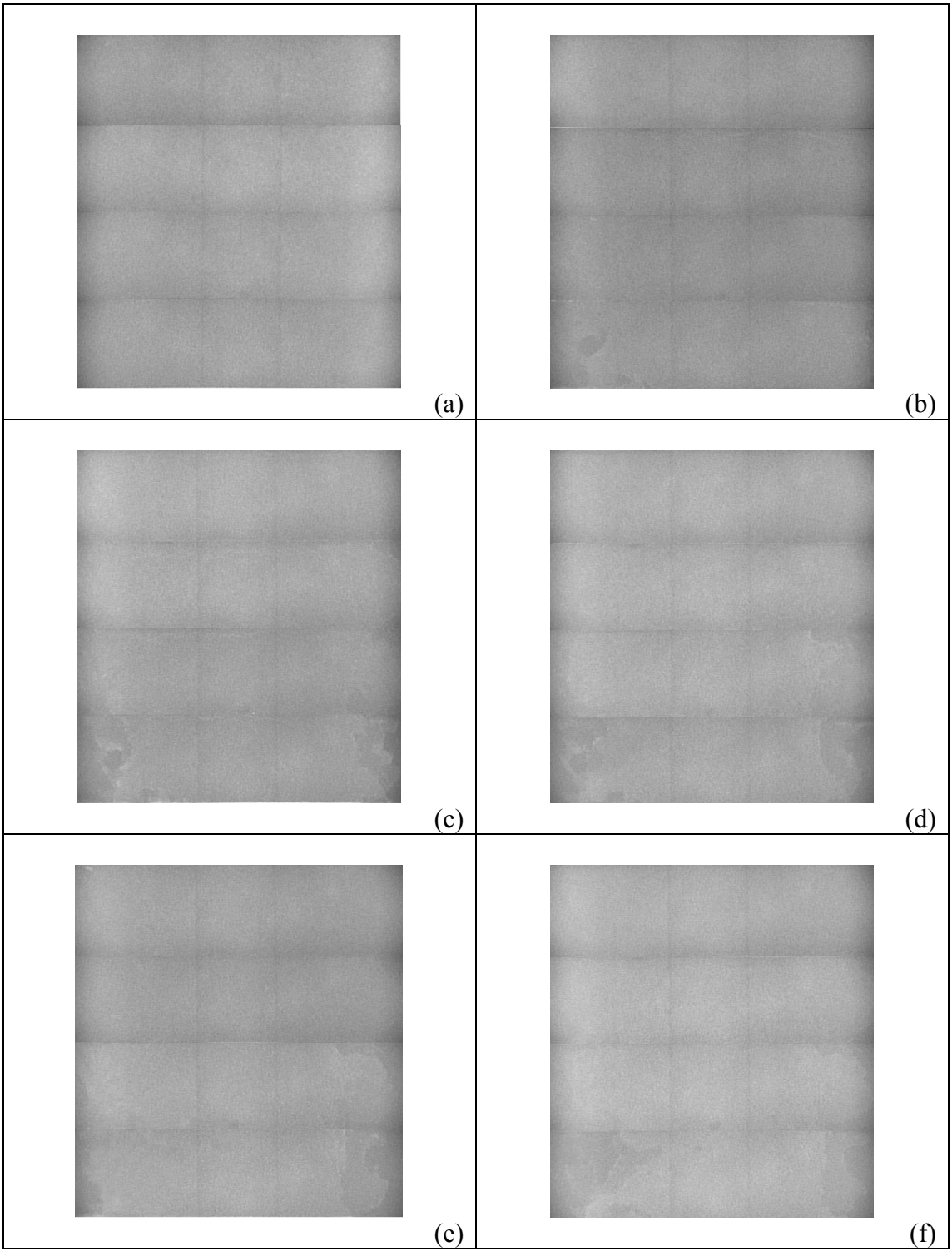

Figure 25 - X-ray investigation on the castings produced using the 10 ppi ceramic foam filter, executed using a Bosello SRE80 industrial equipment.

In Figure 25 are shown the X-ray images related to the 6 reference castings, selected from the whole production with the 10 ppi filters, form which the tensile tests specimens were retrieved. Only the castings with no evidence of porosity were considered to process the tensile tests, to obtain more reliable results. Other 6 castings were then dedicated to the microstructural characterisations.
A second casting campaign using 20 ppi ceramic foam filters has been completed to evaluate if better mechanical properties could be achieved and to see if any changes occurred in microstructure. If it's natural to expect that a greater number of impurities can be retained into a more powerful filtering system, it's also true that fluid-dynamic variations in mould filling must be carefully considered.
In Figure 26 are reported the results of the X-Ray investigation on 8 sound step castings produced during the second campaign. As previously illustrated, some kind of defects are not detectable with X-ray; anyhow no evidence of filling issues due to the 20ppi filters denser mesh was found.

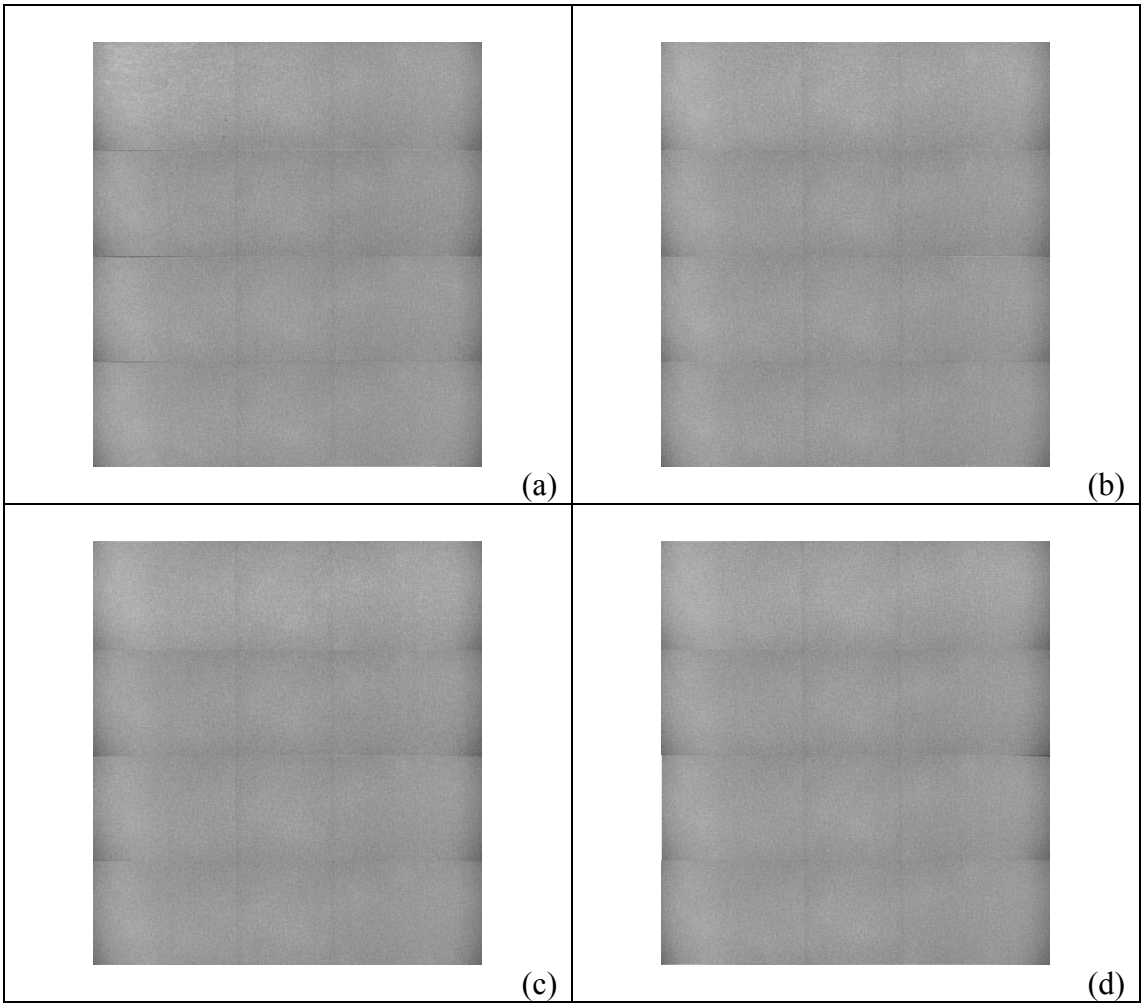

Figure 26 - X-ray investigation images (obtained using a Bosello SRE80 machine) of the castings produced with the 20 ppi filters and chosen for characterisations.

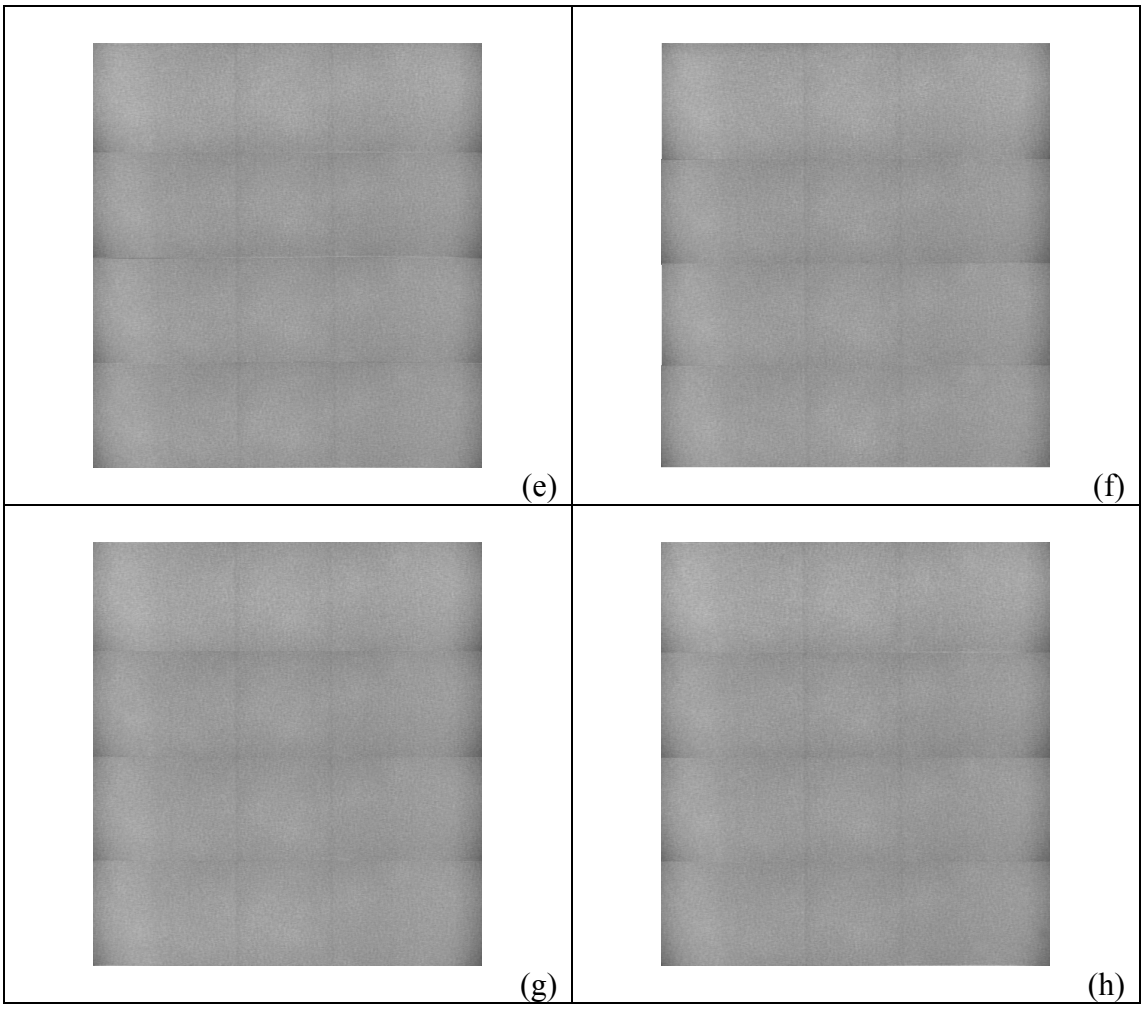

Figure 25 - X-ray investigation images (obtained using a Bosello SRE80 machine) of the castings produced with the 20 ppi filters and chosen for characterisations.

Also for these casting conditions, the microstructure evolution of 6 further castings was considered.

Mechanical Characterisation

Tensile tests make possible to characterise the material. Certain mechanical properties were analysed, in particular the yield stress, the ultimate tensile stress and the percentage elongation.

Specimens Arrangement

To perform the tests, the material needed to be prepared by the right way, to ensure the results reliability and comparability. So the castings previously reserved for these tests (a total of 14 steps castings, considering both the casting campaigns) were firstly purged of unnecessary parts like riser, gate and running system (Figure 27a).

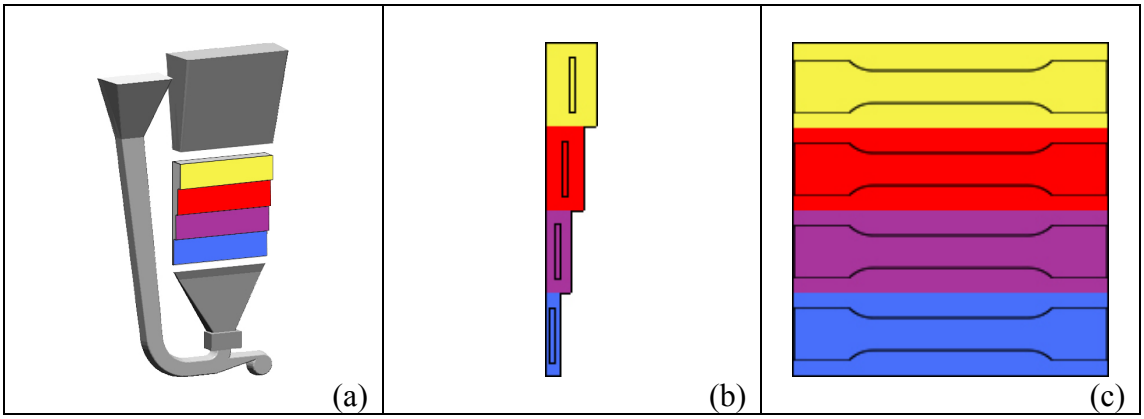

Figure 27 - Resulting casting pattern which highlights (a) the steps and the discarded parts, and (b,c) the position from which the tensile specimens were derived.

Then they were subjected to mechanical processing, to obtain the specimens from the core of each step, as shown in Figure 27b,c. This stage allowed to acquire 56 tensile samples already ready to be processed.
Tensile specimens' geometry was chosen following ASTM rules [50]; shape and dimensions are illustrated in Figure 28. Flat form factor was judged more suitable because of steps' thickness.

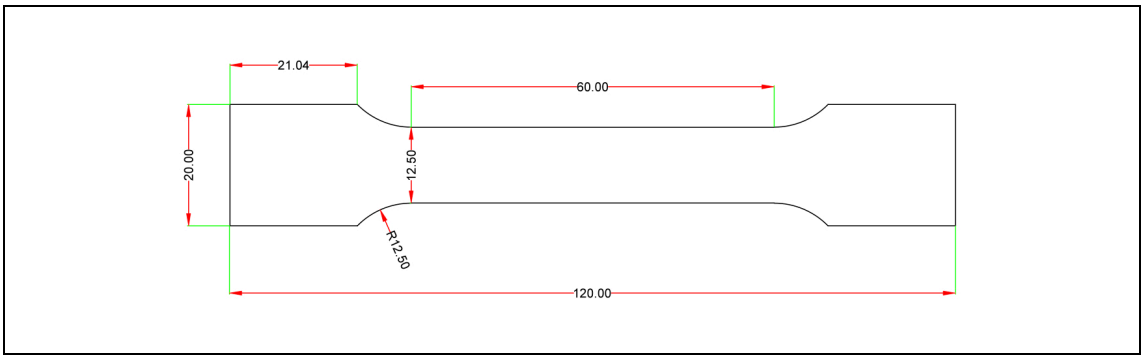

Figure 28 - Geometry and dimensions (mm) of flat specimens for tensile testing [50]. Thickness 3 mm.

Tests Execution Procedure

The static tensile tests were executed approximately at the same conditions, with a MTS 810 servo hydraulic machine (Figure 29a) fitted with a 25 mm strain gauge deformations detector (Figure 29b), at a speed of 1 mm/min and with a temperature between 16°C and 18°C.

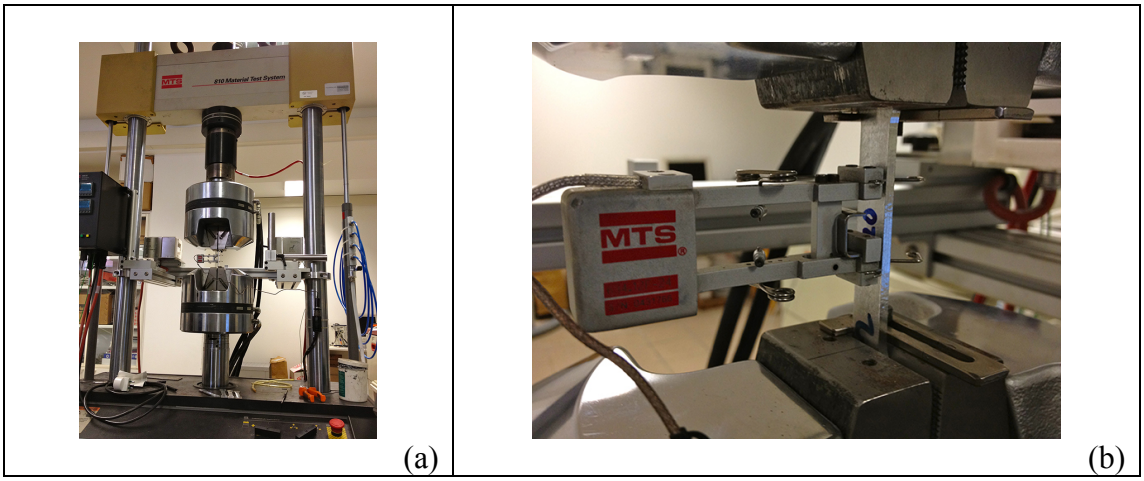

Figure 29 - (a) The MTS 810 tensile tests machine used and (b) the strain gauge deformation detector.

The tensile specimens were clamped into the machine's grips and the test started micrometrically turning away the machine's holds. The machine's integrated system for acquiring data, made sampling at intervals of a few tenths of a second, providing force-elongation data couples. Each test was completed as soon the specimen was broken. An instant before the rupture, the machine recorded the maximum value of the force over the entire duration of the test. That value compared to the initial section is a point of interest and indicates in any way the toughness of the alloy [51].

Considered Parameters

The experimental data obtained were subsequently processed to provide organised values of the elastic limit ($YS_{0.2\%}$), the ultimate tensile strength (UTS) and elongation (e%). The stress-strain curves were plotted, for each specimen, in this way: the instant specific load was calculated dividing the force [N] for the resistant section [mm^2], the deformation instead derives from the relationship between the total elongation of the gauge length [mm] and its initial length [mm]. For this purpose, a prior measurement of the specimens has been required; in particular for each tensile specimen the length, the thickness and the width of the gauge length were measured.
Regarding the data provided by the tests, it's appropriate to specify the following: the ultimate tensile strength was identified by the maximum point of the curve, and it represents the highest load that the specimen could have tolerated before starting to break down; the yield stress was obtained qualitatively by graphical approach, considering a 0.2% offset from the straight line which represents the elastic behavior zone; the percentage elongation came directly by rationing the measured deformation to the original length.

Microstructural Characterisation

Microstructural Evolution during Solidification

As reported in the literature [52] the distribution, the chemical composition and the volume fraction of the constituent phases, depend on the production process, especially on the solidification speed.

Studying magnesium alloys' behaviour it's important considering the *coring* effect [53], a micro segregation that takes place during the solidification of most foundry commercial alloys. In this case, the characteristic microstructure of the studied alloy was achieved by a gravity casting process, and then with relatively low cooling rates.

The solidification sequence of AM60B alloy begins with the nucleation of primary magnesium (α-Mg) at a temperature of about 619°C. As the alloy is cooled, when the temperature reaches about the 433°C the formation of eutectic Mg-$Mg_{17}Al_{12}$ takes place. So the resulting structure consists of primary α-Mg dendrites with α-Mg and β-$Mg_{17}Al_{12}$ into the interdendritic regions.

According to the Mg-Al phase diagram, the β-$Mg_{17}Al_{12}$ formation can be expected when the aluminium content is at least the 13% (Figure 30a).

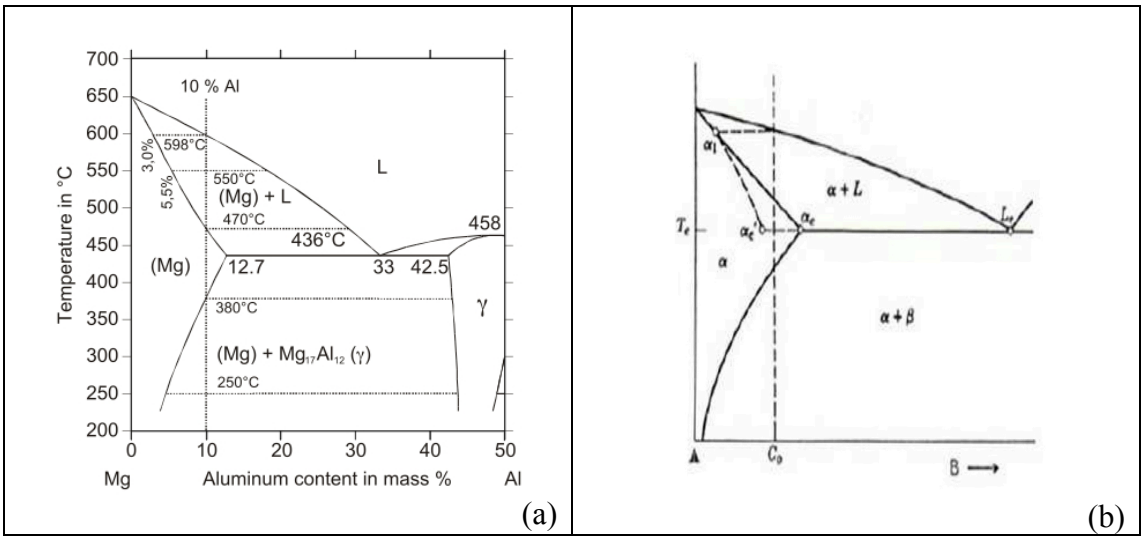

Figure 30 - (a) Magnesium-rich section of Mg-Al system and (b) portion of a generic binary phase diagram showing a shift of the lower concentration limit for eutectic formation due to non-equilibrium cooling conditions [54].

The liquid alloy of composition C_0 (Figure 30b) that solidifies in pseudo-static conditions will not give place to any eutectic transformation; however, when non-equilibrium cooling conditions occur, there is formation of eutectic also for concentrations lower than α_e. The minimum threshold concentration which leads to eutectic formation can move from α_e (equilibrium cooling conditions) to α_e' for abrupt cooling (Figure 30b).

Investigation Method

With the aim of correlating the resulting microstructure with cooling conditions and mechanical properties, microstructural investigations were carried out on some

reference castings. From the step castings reserved for the metallographic analysis were obtained the samples, at the middle section, i.e. the area in which most breaking occurred during the tensile tests on similar samples dedicated to such tests.
The samples, prepared according to conventional metallographic techniques, were observed with an optical microscope (Leica DMLA) and analysed using an image processing software (Leica LAS).
The microstructure of the analysed alloy were studied, in correspondence of different thicknesses, through a large number of captured images. The high number of detections ensures a high quality of realised statistics. To calculate the equivalent grain size and the eutectic fraction, the samples were chemically etched with different solutions, one consisting of 5 ml of acetic acid in 100 ml of demineralised water (Figure 31a) to highlight the gain borders, and a solution of 1.5 ml of phosphoric acid with 2 ml of nitric acid in 100 ml of ethanol (Figure 31b) for emphasizing the eutectic and the intermetallic compound.
For the reasons mentioned above, in the alloy used during this study, which contains about 6% of aluminium, a precipitation of eutectic occurs. The magnesium dendrites growth takes place according to usual solidification principles of primary α-Mg phase: in the dendrites core there is a poor Al content and with the solidification progress the liquid is enriched in aluminium, till reaching the eutectic composition that solidifies at the end of the cooling process. So the Al content in α-Mg is lower in the zones far from β-$Mg_{17}Al_{12}$.

Observed Microstructure

The solidified alloy is so characterised by the presence of equiaxic grains of α-Mg primary phase (Figure 31a), within dendrites, with a rich solid solution of aluminium in the interdendritic regions.

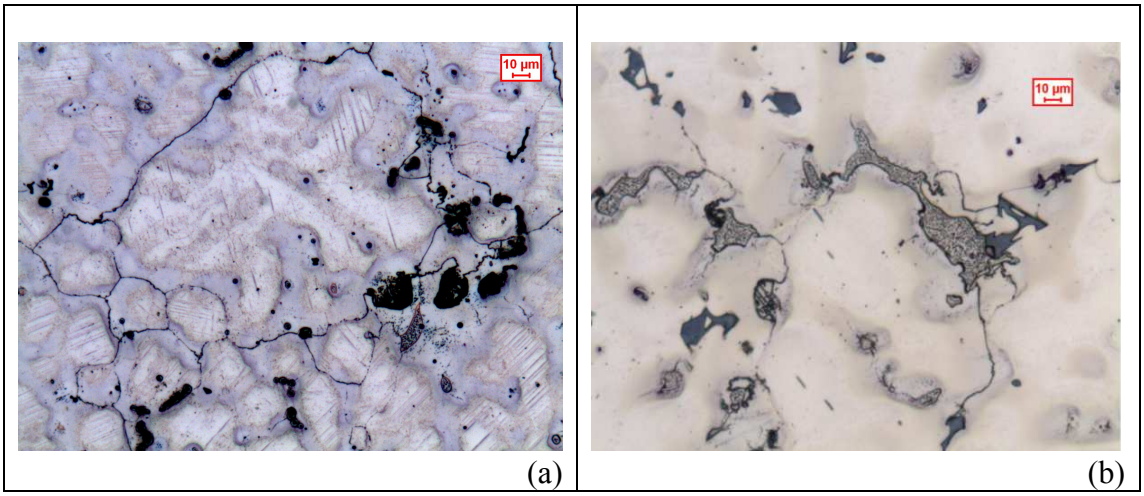

Figure 31 - Microstructure (200X Leica pictures) of gravity cast AM60B alloy: images showing (a) grain boundaries and (b) morphology of eutectic and intermetallic compound.

In the grain boundary and in the interdendritic regions occurs the precipitation of $Mg_{17}Al_{12}$ induced by the variation of solubility of aluminium.
The eutectic Mg-$Mg_{17}Al_{12}$ clearly derives from a non-equilibrium solidification conditions, which produce micro-segregation phenomena, with a drastic reduction of α-Mg amount. This typical eutectic morphology can be described as a network of

interconnected $Mg_{17}Al_{12}$, which contains "islands" of α-Mg. This partially divorced structure can be found, as well as Al-Mn intermetallic compounds, at the grain boundaries and in the interdendritic regions (Figure 31b).
The end of the eutectic solidification doesn't necessarily mean the conclusion of phase transformations in this alloys. With gravity castings process typical cooling rates, other precipitations occur in the oversaturated zones of α-Mg. This precipitation can have two forms, either continuous or discontinuous.
The most common form in this study is the discontinuous one (Figure 32).

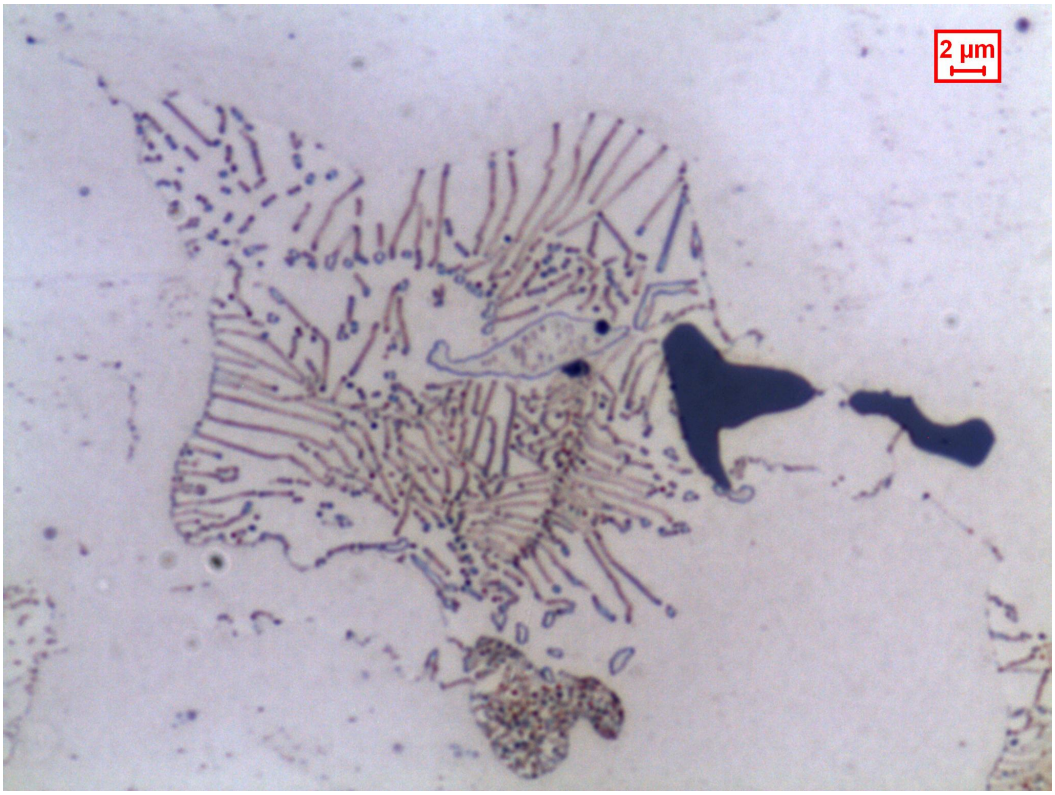

Figure 32 - 1000X optical microscope image representing a typical lamellar precipitate in AM60B alloy.

The growth of these precipitates, that have lamellar morphology and $Mg_{17}Al_{12}$ composition, takes place inside the α-Mg grains, similarly to the growth of the pearlite's lamellae inside of the austenite grain during the cooling of the steel. This discontinuous precipitation seems to grow from the eutectic $Mg_{17}Al_{12}$ towards the inside of the α-Mg grain.
These discontinuous precipitates nucleate separately in the oversaturated α-Mg and, mainly, they are located in the interdendritic regions, closest to the eutectic Mg-$Mg_{17}Al_{12}$, since these regions have a higher aluminium content than into the core of the dendrites, where the concentrations of aluminium are significantly lower.

Analysed Parameters

The executed microstructural analysis was a quantitative investigation, based on direct visual observation. The eutectic structure, the lamellar precipitates, the intermetallic compounds and the equivalent grain size were considered in this stage.
To ensure more detailed and reliable results, is was made use of the aid of automatic calculation techniques. An appropriate routine, embedded in the QWin software, allowed to analyse 50 neighboring zones in the core of each prepared sample. These investigation was performed at a fixed optical magnification for all the specimens, and permitted to quantify the percentage area of the considered particles and their characteristics, such as the area, the perimeter, the roundness, the aspect ratio and the equivalent diameter.

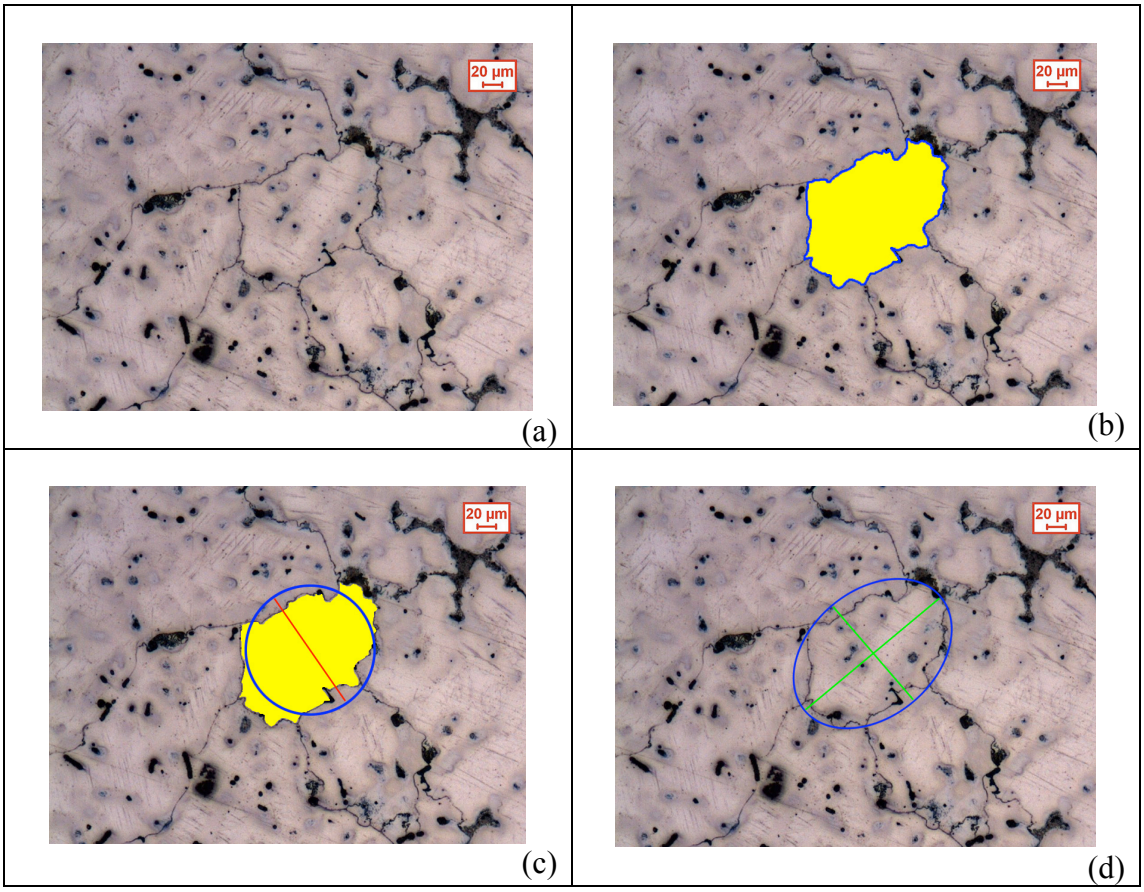

Figure 33 - Graphical representation of the analysed parameters.

Excluding the percentage content, whose meaning is easy to understand, an indicative graphical representation of how the other parameters are calculated is shown in Figure 33. Considering one of the grains highlighted in the micrograph in Figure 33a, the related area and perimeter can be measured as shown graphically in Figure 33b, allowing to define the equivalent circle diameter as observable in Figure 33c. By relating the grain area with the ideal circle one is then possible to define the grain roundness. The grain aspect ratio is defined as the ratio between the grain length and the grain width, as indicated in Figure 33d.

Experimental Results

The numerical simulation is a powerful tool to study the filling behaviour of a die and to predict the defects' formation. But there are many other useful data, which come from the simulation, which can help to understand the dynamics regarding the whole casting process. In order to establish relationships between the process parameters and the accordingly developed microstructures, initially it is convenient to consider the times and the rates of metal solidification, with reference to the different die thickness.

Cooling Rates

In the results provided by numerical simulation the values of the solidification times and of the cooling rates are present, but it has to be considered that not all the input parameters that are provided as input to the simulation are accurate. It can be definitely assumed as exact the geometry of the mould, the chemical composition of the alloy and of the mould's material, the filling time and other parameters related to the execution of the casting process. One of the most difficult phenomenon to consider is the way in which the alloy and the mould exchange the heat between them. The simulation software contemplates the models that describe the thermal exchanges for the most common alloys and processes, such as high pressure die casting. This unfortunately is not the case for processes such as the permanent mould gravity casting. In these circumstances the heat transfer coefficient must be estimated using the information provided by competent sources [55], then combining the experimental data with the empirical ones.

Mould Thermal Field Data

During the mould assembling operations, three permanent thermocouples were installed into the mould, to monitor the thermal gradients both during the preheating stage of the mould and during the casting operations. Thus, these thermal field data can be used to reconstruct the manner in which the alloy and the mould exchange the heat between them during the entire process. Figure 34 represents the history of the temperatures in the mould in correspondence of the permanent thermocouples, positioned as shown in Figure 23b.

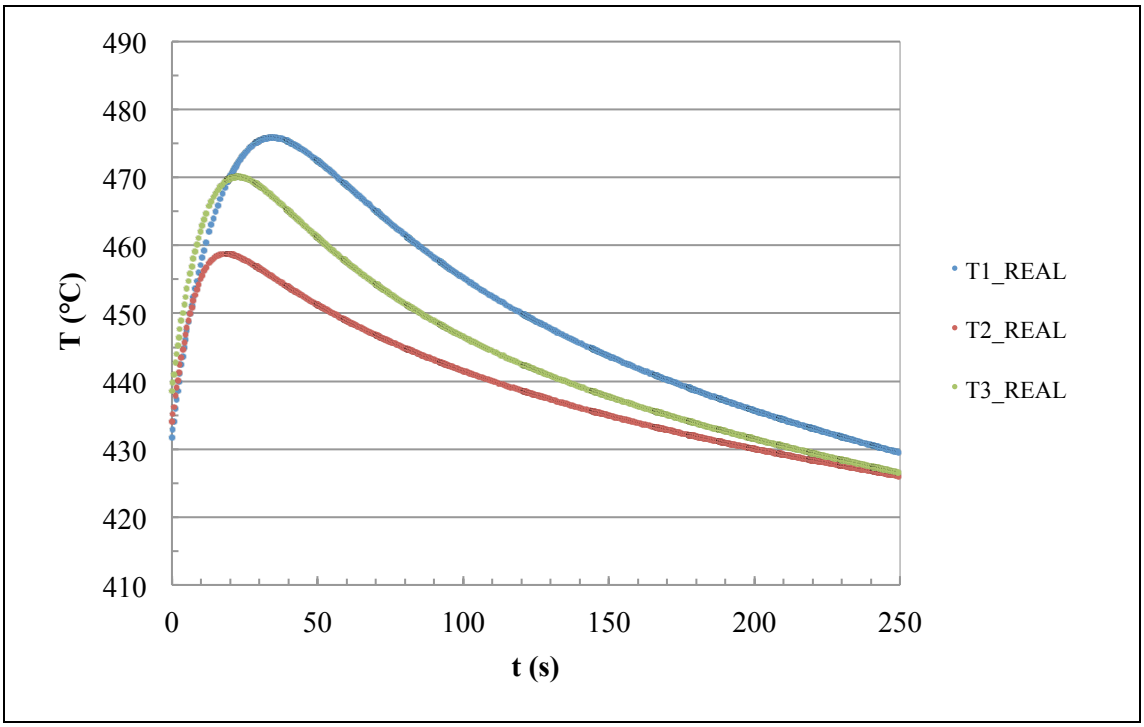

Figure 34 - Temperatures revealed by the permanent thermocouples in the mould during the filling of the die and during the solidification of the casting.

A manual optimisation is consequently needed to find a match between real thermocouples values and simulation ones, acting on the heat transfer coefficient until a correspondence is found.

Heat Transfer Coefficient Optimisation

As anticipated, the casting simulation software included the HTCs related to the most widespread processes in the industry. As a starting point, a HTC "close" to the combination of alloy, mould and process, can be chosen if the optimal one is not present in the database. So a heat transfer coefficient for an AM60B magnesium alloy and for an AISI H11 mould was initially taken from the available ones, but it referred to the most common HPDC instead of the permanent mould (gravity) casting process, so it was modified to be more compliant to the gravity casting process [55].
The time dependant heat transfer coefficient for the HPDC process is represented in Figure 35.

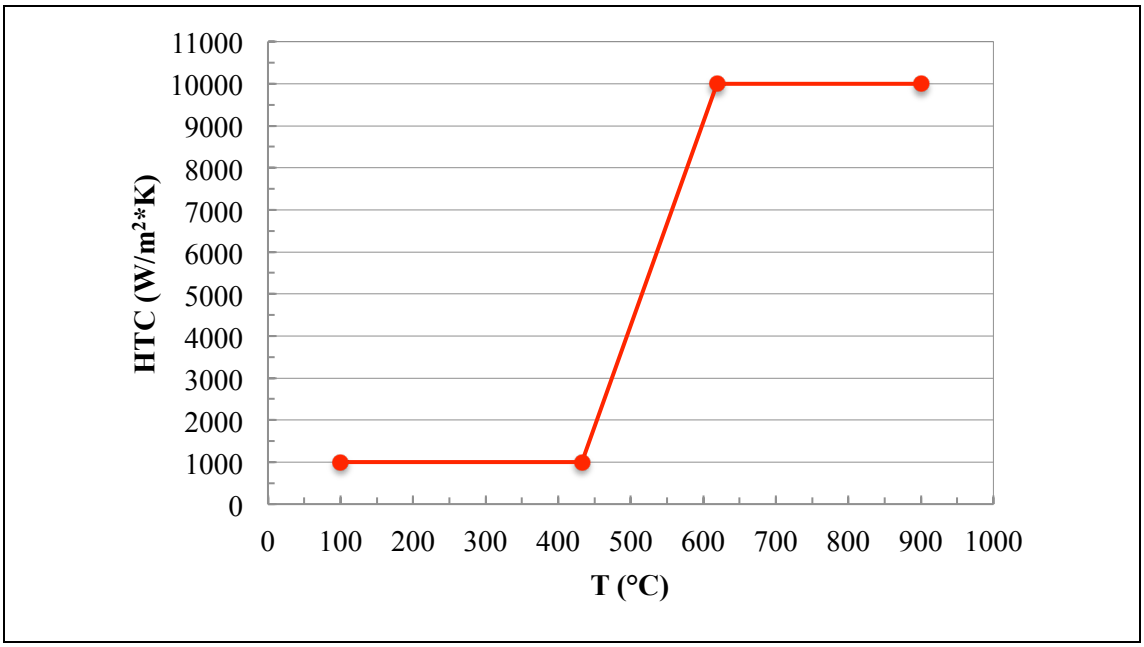

Figure 35 - Temperature dependant heat transfer coefficient between AM60B alloy and H11 mould. Data provided by Magma casting simulation software, valid for HPDC process.

It is obvious that this HTC can't be the most adequate to describe the heat transfer between alloy and mould during a gravity casting process. The time in which the molten metal fills the die and the pressures are very different between HPDC and gravity casting. However, it can be useful to observe and graphically analyse the relationships between permanent thermocouples history data and the HTC used to simulate the process. In Figure 36 it is shown a comparison between the real acquired data by the permanent thermocouples and the thermal field data provided by the simulation software using the HTC represented in Figure 35.

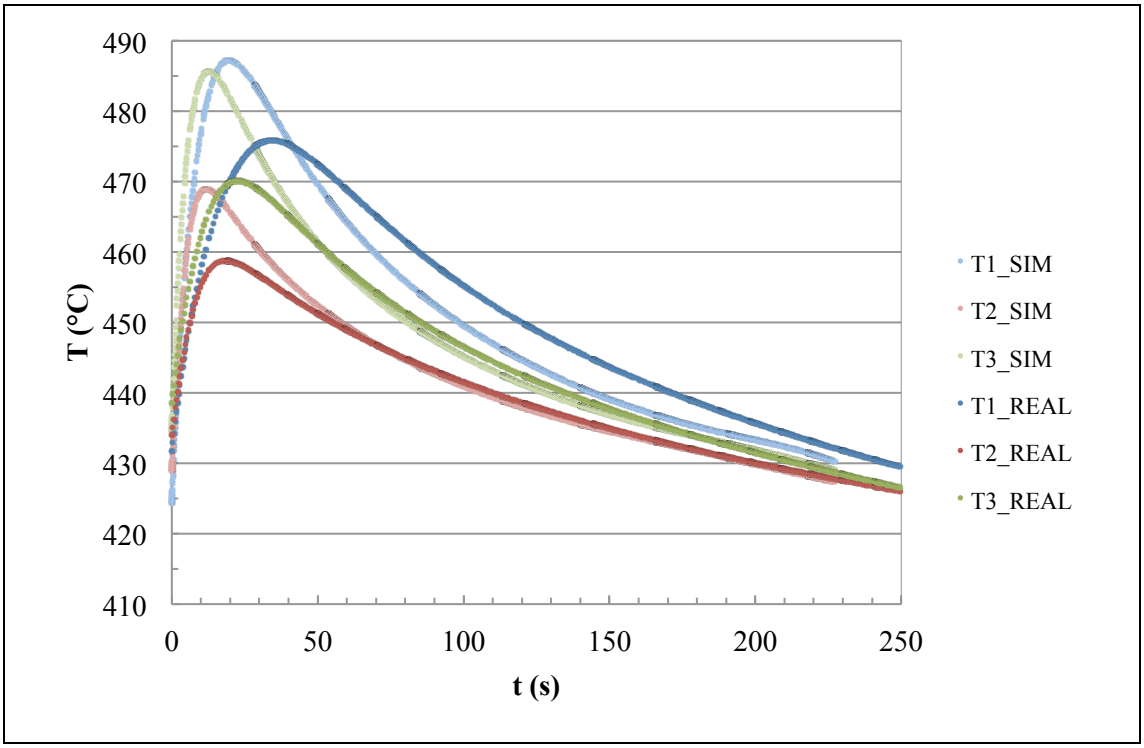

Figure 36 - Comparison between measured mould thermal field data and mould temperatures calculated using the standard die casting HTC.

This gives a further confirmation of the very different conditions for these processes. For these reasons, in the preliminary numerical simulations of the casting process, necessary to design the optimised mould, a modified HTC according to ASM recommendations was used [55], as shown in Figure 37.

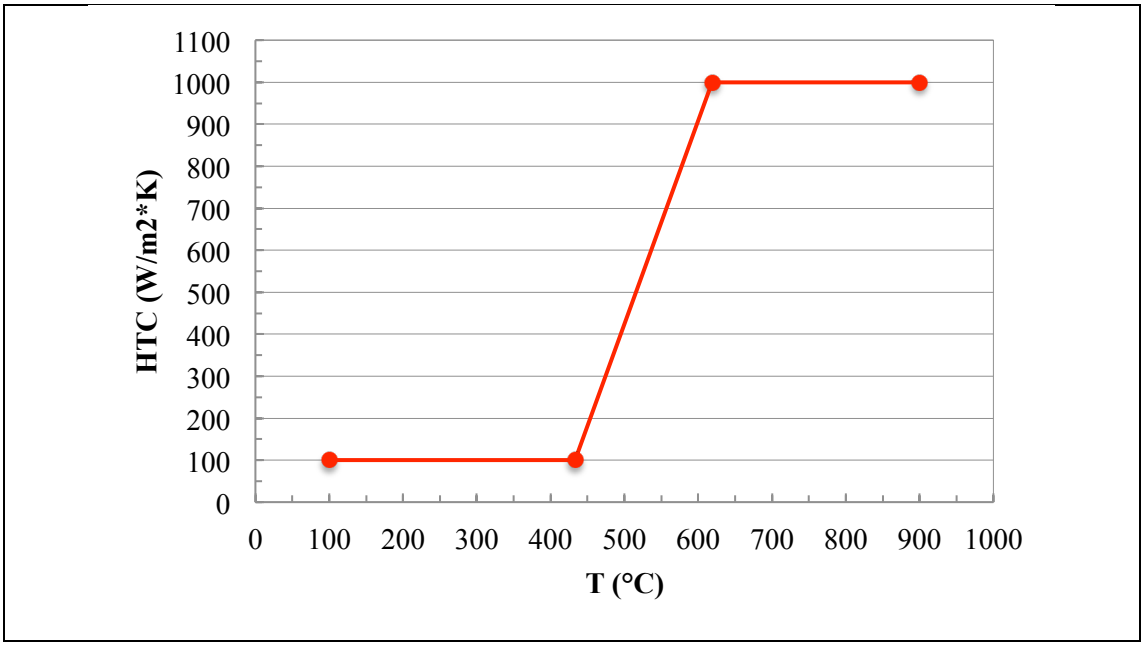

Figure 37 - AM60B permanent mould (gravity) casting heat transfer coefficient as suggested by ASM [55].

Comparing the virtual thermocouples data with the real ones (Figure 38), it can be noticed that even this configuration doesn't describe adequately the thermal behaviour of the system.

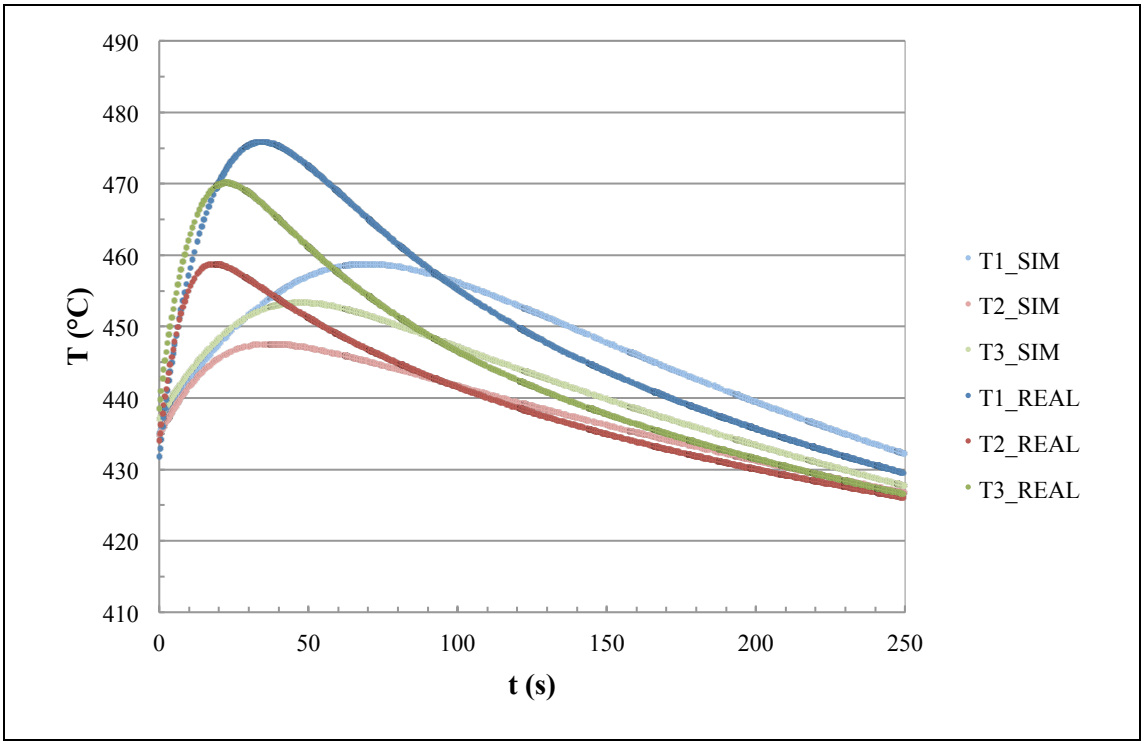

Figure 38 - Comparison between measured mould thermal field data and mould temperatures calculated using the standard permanent mould (gravity) casting HTC.

Consequently, a manual optimisation of the HTC must be performed to find a balance between real thermocouples values and virtual ones. First of all, a clarification must be done: the mechanisms describing the heat exchange in the real world can not be simplified by a HTC that considers only the solidus and the liquidus temperatures. Combining the real data with those provided by the simulation it was possible to find a good correspondence by considering a more complex HTC than suggested by the simulation software. The optimised HTC is represented in Figure 39.

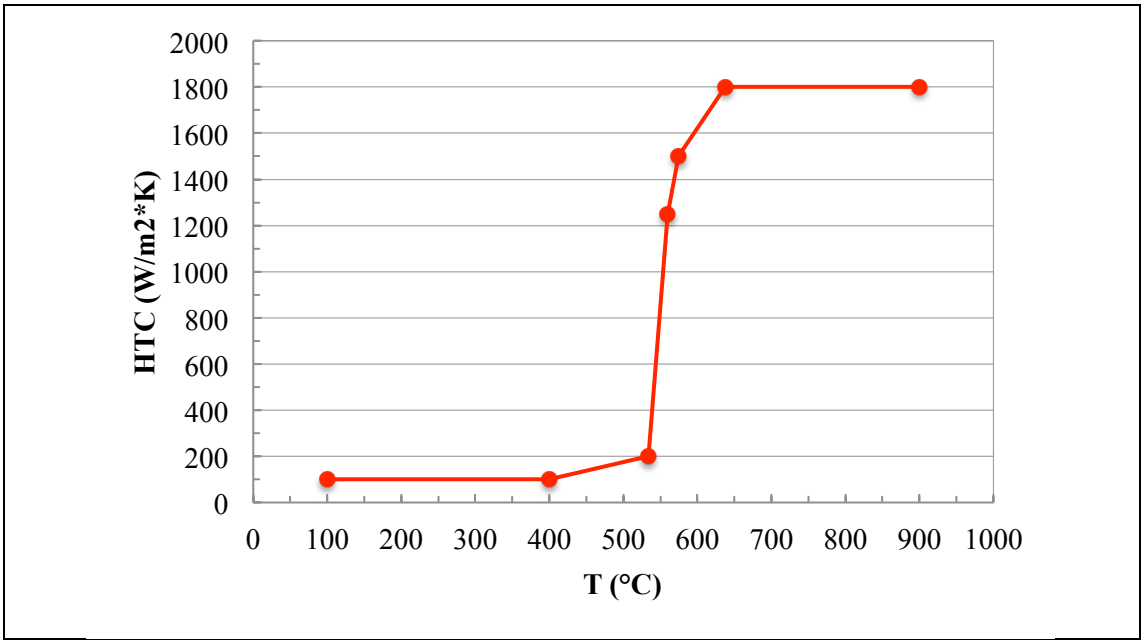

Figure 39 - The optimised temperature dependant heat transfer coefficient, between AM60B alloy and AISI H11 mould, for permanent mould gravity casting process.

This heat transfer model adequately describes the dynamics that occur with this combination of alloy, mould and process, and the good correspondence between thermal field data calculated adopting this model and the real ones (Figure 40) supports the approach adopted for the HTC evaluation.

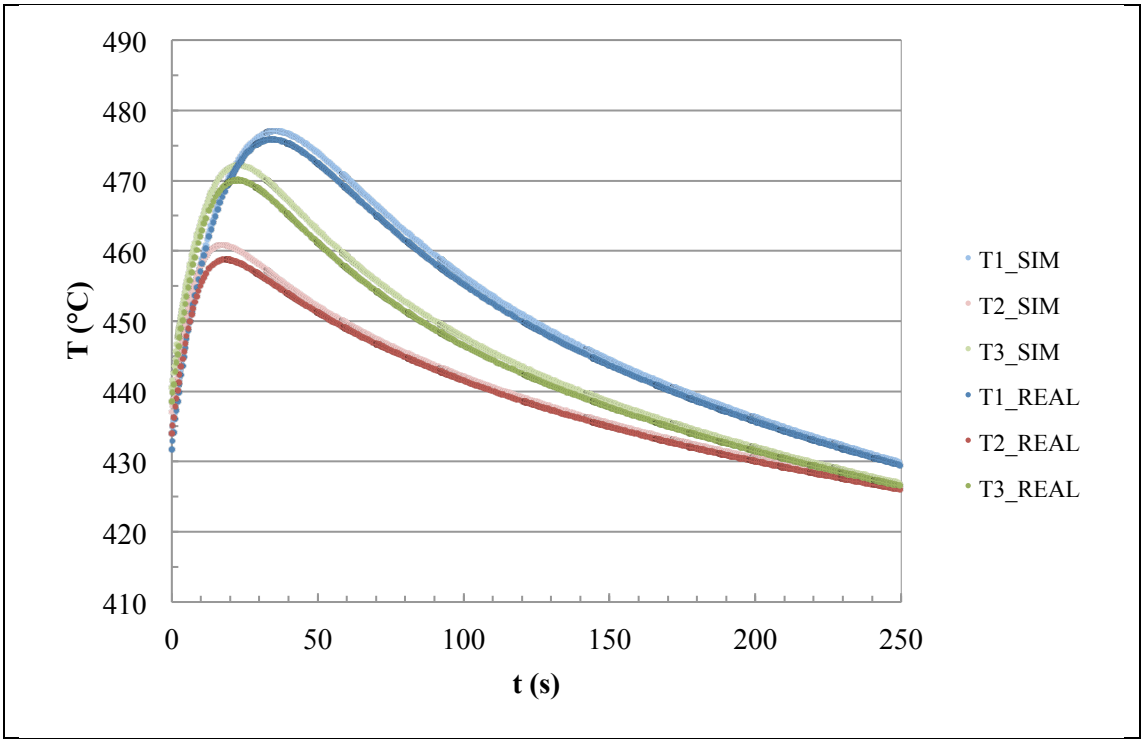

Figure 40 - Correspondence between calculated mould thermal field data (by using the optimised HTC) and the experimental ones.

Solidification Times and Cooling Rates

Now, having all the elements that describe the process, it's possible to obtain an accurate evaluation of the times needed by the molten metal to solidify, in the centre of each different thickness step. By setting up the numerical simulation with the optimised HTC, the virtual thermocouples placed in the middle section of the casting give the solidification and cooling histories reported in Figure 41.

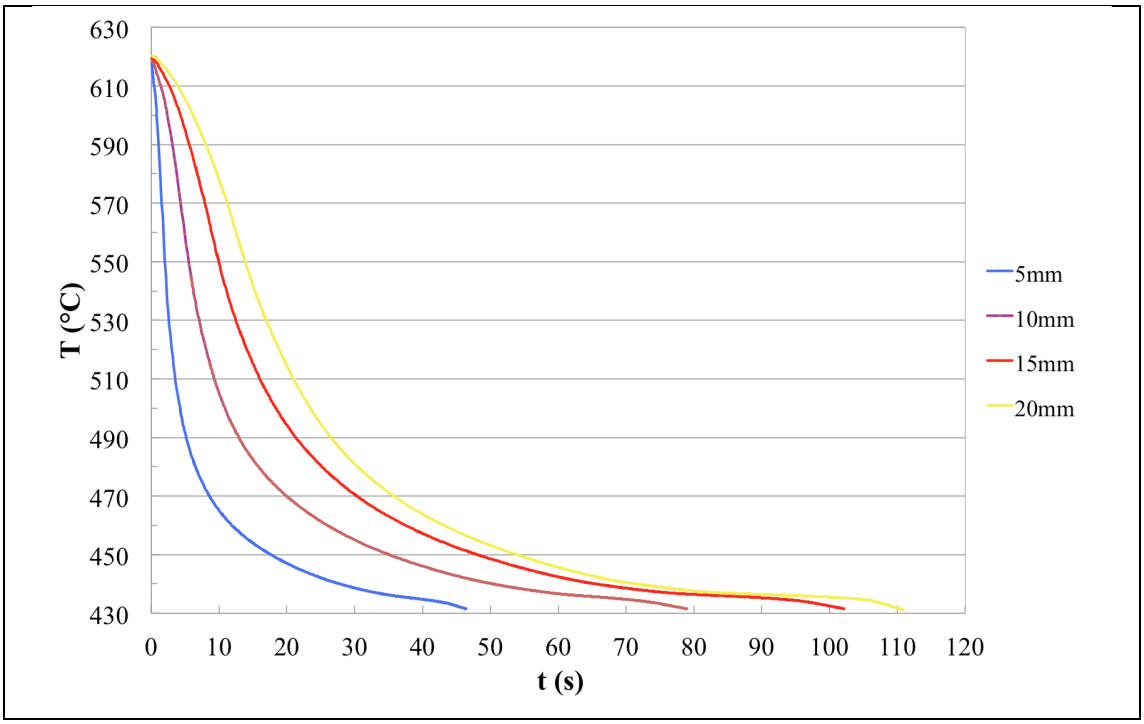

Figure 41 - Solidification and cooling history calculated in the centre of each step using the optimised heat transfer coefficient.

By analysing the numeric output of the simulation, it's possible to estimate the values of the solidification times and to calculate the average cooling rate, as shown in Table 3.

Table 3 - Calculated solidification times and cooling rates in the core of each different thickness step.

Step thickness (mm)	Solidification Time (s)	Cooling Rate (°C/s)
20	108	1.73
15	97	1.91
10	72	2.59
5	42	4.48

Such data are now available for analysing the microstructure evolution as a function of the cooling conditions.

Microstructural Characteristics

The microstructure evolution as a function of the cooling conditions will be analysed in this section.

Eutectic Analysis

The aim of the investigation on eutectic was firstly to estimate its content in the specimens obtained from the core of each castings' step, and then to analyse its dimension and its shape. In the Table 4 are reported the eutectic percentage revealed in the castings obtained using the 10 ppi filters, and in Table 5 the results coming from the same analysis on the castings produced adopting 20 ppi ceramic foam filters.

Table 4 - Eutectic content detected in the castings produced using 10 ppi ceramic foam filters.

Step thickness (mm)	Average eutectic content (%)	Standard deviation
20	0.72	0.64
15	0.67	0.58
10	0.96	0.47
5	0.85	0.60

It isn't noticeable a clear trend for the eutectic content detected in the first samples, only a slight increase with the thinning of the steps, and generally the content seems to be very similar in the two thicker steps, between 0.67% and 0.72%. The same phenomenon is observed considering the eutectic calculation performed on the thicker steps of the second campaign castings (Table 5), where the eutectic fraction is between 0.69% and 0.70%.

Table 5 - Eutectic content detected in the castings produced using 20 ppi ceramic foam filters.

Step thickness (mm)	Average eutectic content (%)	Standard deviation
20	0.70	0.59
15	0.69	0.59
10	0.48	0.37
5	0.56	0.47

But in this case, the eutectic fraction decreases with the thinning of the steps. These different trends can find an explanation in the solidification phenomena that take place increasing the cooling rate.

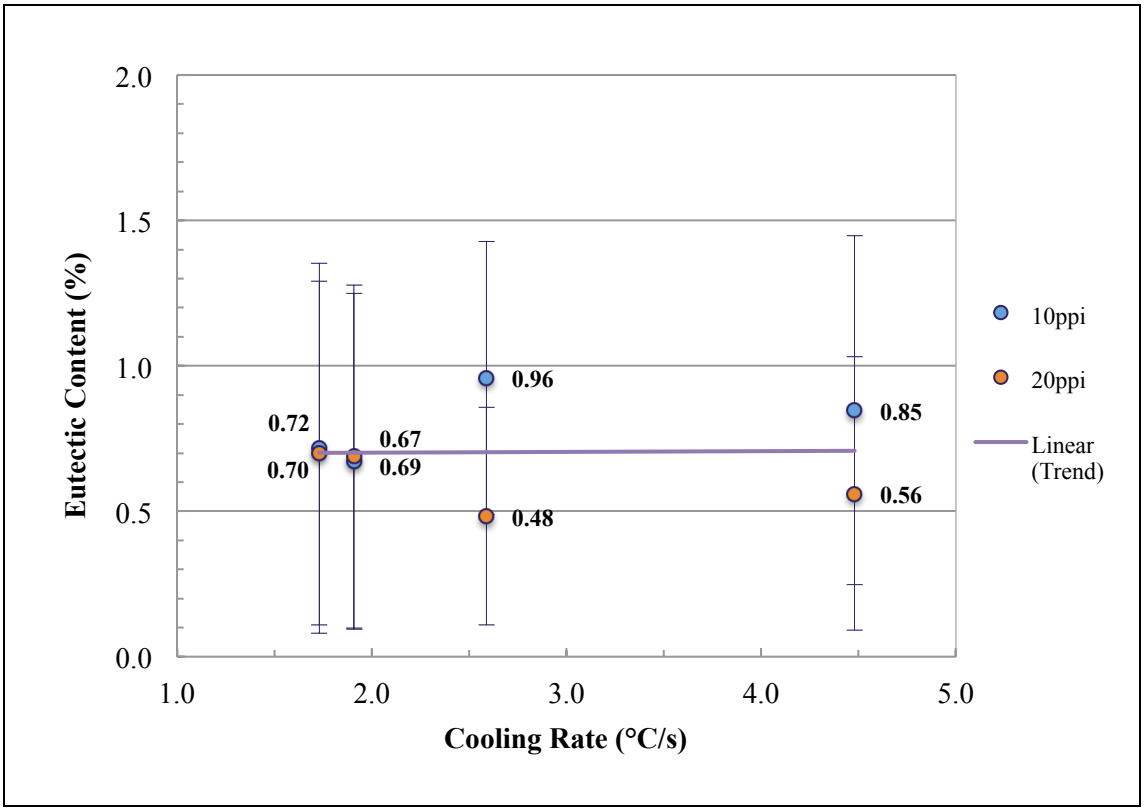

Figure 42 - Summary of the eutectic fraction values coming from the microstructural investigation on all samples (both 10 and 20 ppi filters tests). The eutectic content is related to the cooling rate.

Analysing all the acquired data, the overall trend shows that the eutectic fraction seems to keep constant varying the cooling conditions (Figure 42). Considering the standard deviation values, both series (10ppi, 20ppi) have the same trend: maximum deviation in the step having greater thickness (0.59, 0.64), followed by a decrease until the 10 mm step (0.37, 0.47), and a final increase for the thinnest step (0.47, 0.60). This may be a consequence of the mould filling dynamics, and of the rapid solidification in correspondence of thin walls, which produces less uniform microstructures.
In Table 6 and Table 7 the eutectic particles equivalent diameter data are reported, as resulting from the analysis on both the casting campaigns.

Table 6 - Eutectic particles equivalent diameter measured in the castings produced using 10 ppi filters.

Step thickness (mm)	Average equivalent diameter (μm)	Standard deviation
20	8.63	2.68
15	6.87	2.58
10	8.02	2.41
5	6.84	2.38

The average value of the eutectic diameter, detected in the core of each step, decreases in a discontinuous way in the first series, from 8.63 μm in the 20 mm step to 6.84 μm in the 5 mm step (Table 6), and decreases gradually in the second series, from 7.55 μm to 5.91 μm (Table 7). Also the standard deviation has the same trend, decreasing with the thickness.

Table 7 - Eutectic particles equivalent diameter measured in the castings produced using 20 ppi filters.

Step thickness (mm)	Average equivalent diameter (μm)	Standard deviation
20	7.55	2.86
15	7.43	2.53
10	6.81	2.77
5	5.91	2.12

Considering the overall obtained data, the eutectic equivalent diameter decreases increasing the cooling rate, as visible in Figure 43 that represents the correlation between the average equivalent diameter of the eutectic particles and the cooling conditions.

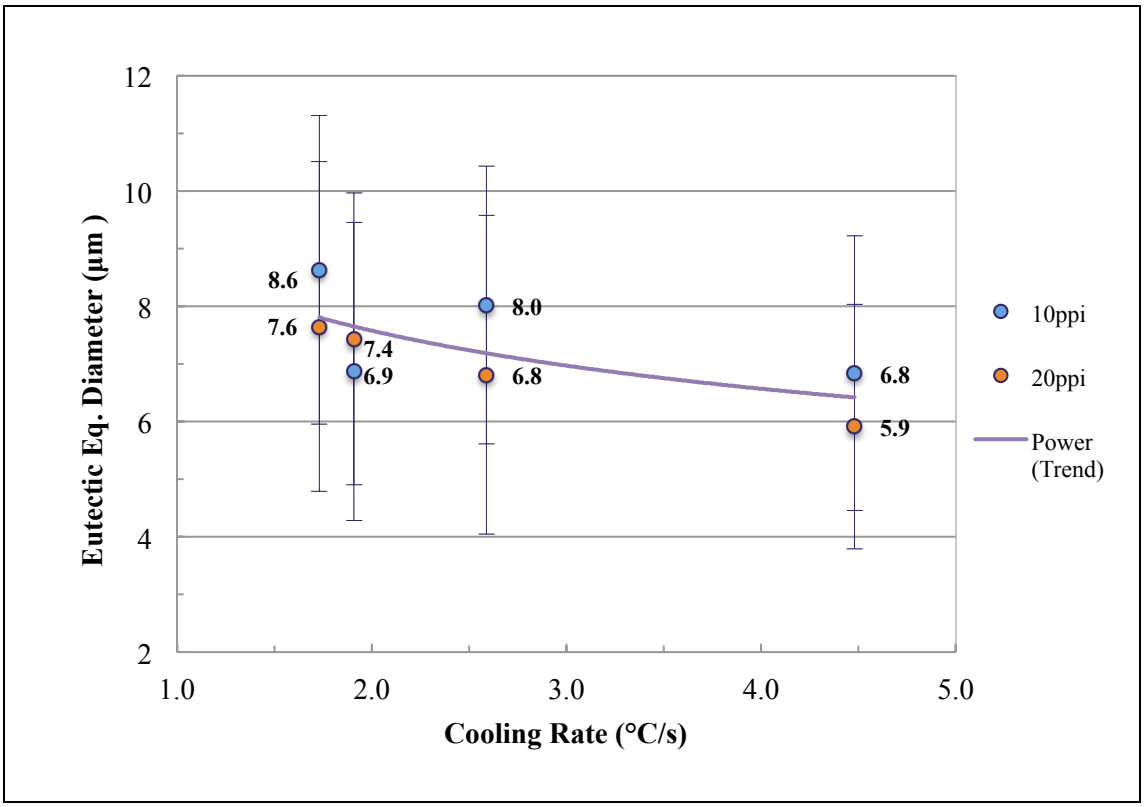

Figure 43 - Summary of the eutectic equivalent diameter analysis: both 10 and 20 ppi trials are considered. The equivalent diameter is related to the cooling rate.

By studying the eutectic's shape, it can be seen that from the eutectic roundness analysis significant data trend can not be individuated.

Table 8 - Eutectic particles roundness resulting from the investigation on the 10 ppi tests castings.

Step thickness (mm)	Average eutectic roundness	Standard deviation
20	1.67	0.62
15	1.42	0.44
10	2.08	0.78
5	1.54	0.73

The first series (Table 8) has a greater range, from 1.42 to 2.08, while the second one (Table 9) gives more close values, from 1.70 to 1.83; it this case, it can be assumed an influence by the filter's denser mesh.

Table 9 - Eutectic particles roundness resulting from the investigation on the 20 ppi tests castings.

Step thickness (mm)	Average eutectic roundness	Standard deviation
20	1.76	0.86
15	1.70	0.70
10	1.83	0.95
5	1.72	0.73

Relating all the collected roundness data to the cooling rate (Figure 44), it's even more clear how the cooling conditions in this case don't affect such geometric parameter, relatively to the eutectic.

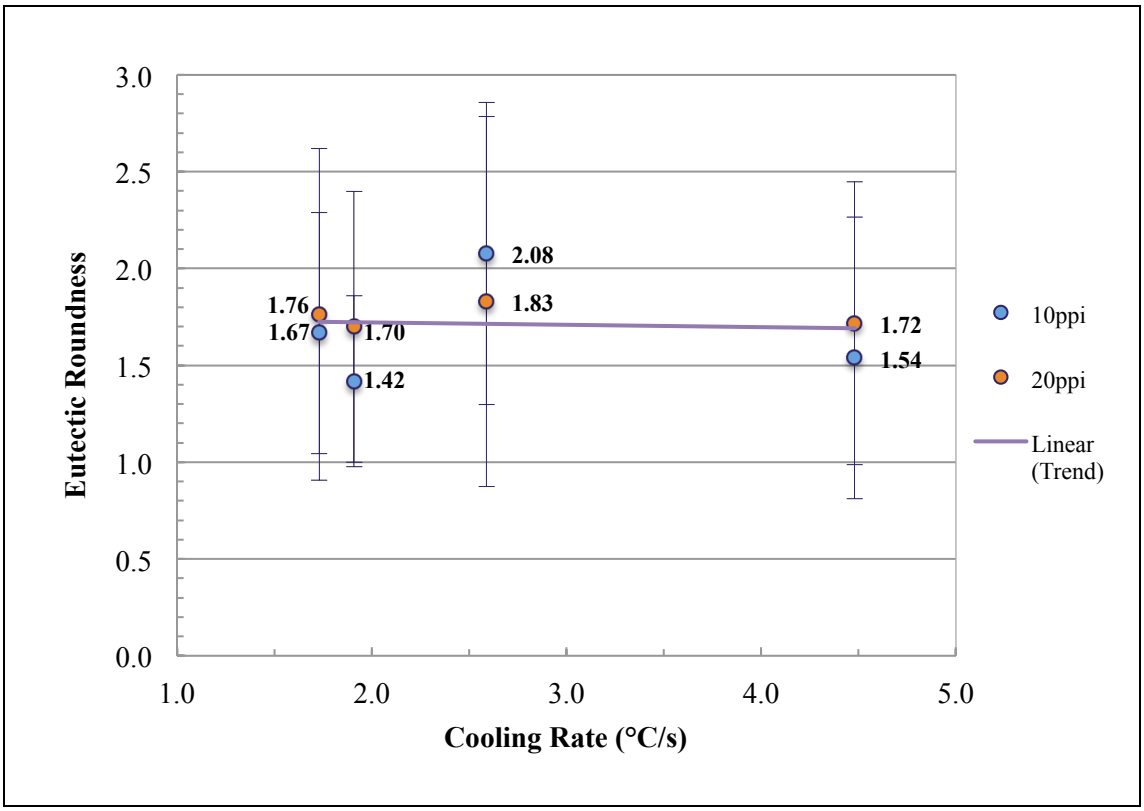

Figure 44 - Summary of the eutectic roundness analysis on both 10 and 20 ppi trials. The roundness is related to the cooling rate.

The linear trend shown in Figure 44 get a even stronger connotation if only the orange dots are considered, in other terms contemplating the 20 ppi series, for the reasons explained above. Considering the aspect ratio of the eutectic particles, it's visible a slight decreasing trend with the increasing of the cooling rate, more linear considering only the values of the second series (Table 11).

Table 10 - Eutectic particles aspect ratio regarding the castings produced using 10 ppi filters.

Step thickness (mm)	Average eutectic aspect ratio	Standard deviation
20	1.73	0.46
15	1.73	0.56
10	1.81	0.56
5	1.67	0.53

For both the series the standard deviation rises with the cooling rate, and also in this case the trend is more pronounced for the second series. Globally it's hard to assign a main role to the cooling conditions in these trends.

Table 11 - Eutectic particles aspect ratio regarding the castings produced using 20 ppi filters.

Step thickness (mm)	Average eutectic aspect ratio	Standard deviation
20	1.75	0.53
15	1.72	0.48
10	1.70	0.56
5	1.68	0.58

Looking at the summary chart (Figure 45) this point is more clear: there isn't a significant relation between the cooling rate and the final aspect ratio of the eutectic.

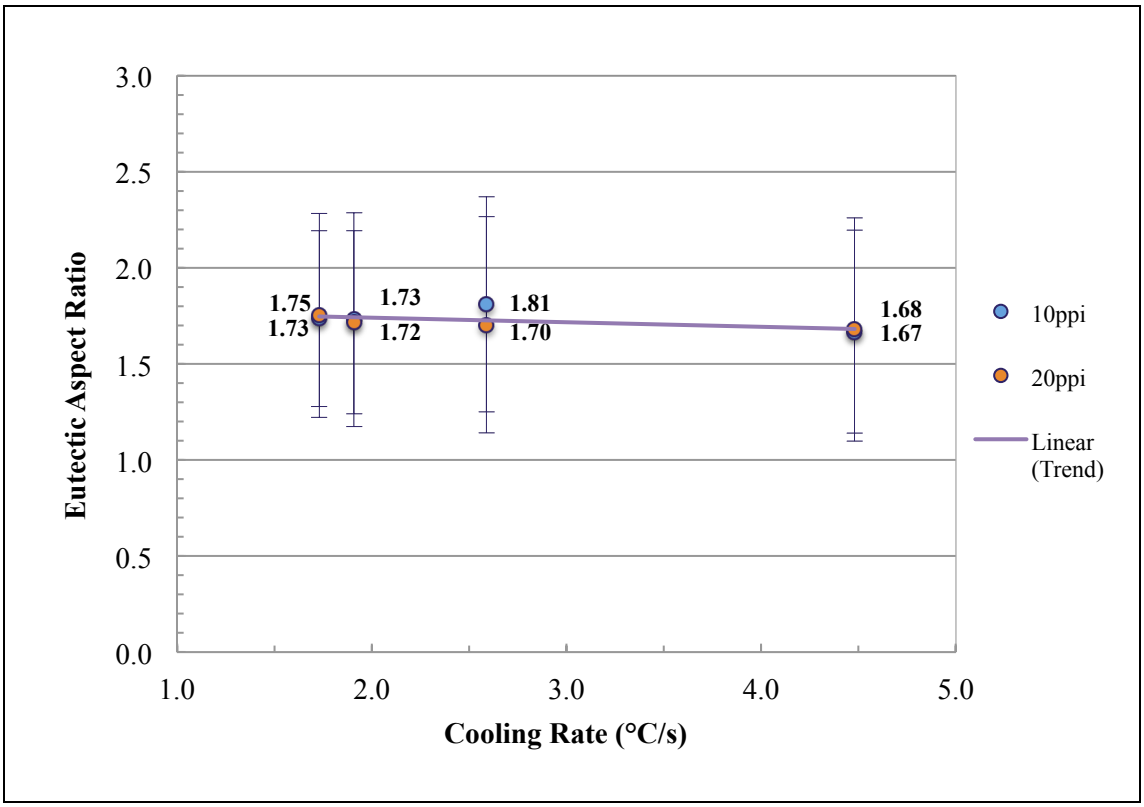

Figure 45 - Summary of the results coming from the aspect ratio evaluation on all samples.

Lamellar Precipitate

It's very interesting to study now the lamellar structures and their size. Below are shown the data referred to the percentage occupied by these structures for the castings produced with the 10 ppi filter (Table 12) and for those obtained by using the 20 ppi filter (Table 13).

Table 12 - Lamellar precipitate content detected in the castings produced using 10 ppi ceramic foam filters.

Step thickness (mm)	Average precipitate content (%)	Standard deviation
20	0.55	0.32
15	0.64	0.53
10	0.73	0.58
5	1.24	0.65

It can be immediately noticed that the first series castings have a percentage of lamellar structures that increases from a value of 0.55% up to 1.24%, passing from the

thicker step to the thinnest one, i.e. increasing the cooling rate. The standard deviation values present the same trend.

Table 13 - Lamellar precipitate content detected in the castings produced using 20 ppi ceramic foam filters.

Step thickness (mm)	Average precipitate content (%)	Standard deviation
20	0.21	0.20
15	0.50	0.45
10	0.69	0.56
5	0.98	0.61

Looking at the second series castings, the percentage of lamellar precipitates grows from 0.21% to 0.98%, starting from the thicker step and arriving to the thinnest one. The standard deviation values present the same trend also in this series, increasing with the cooling rate.

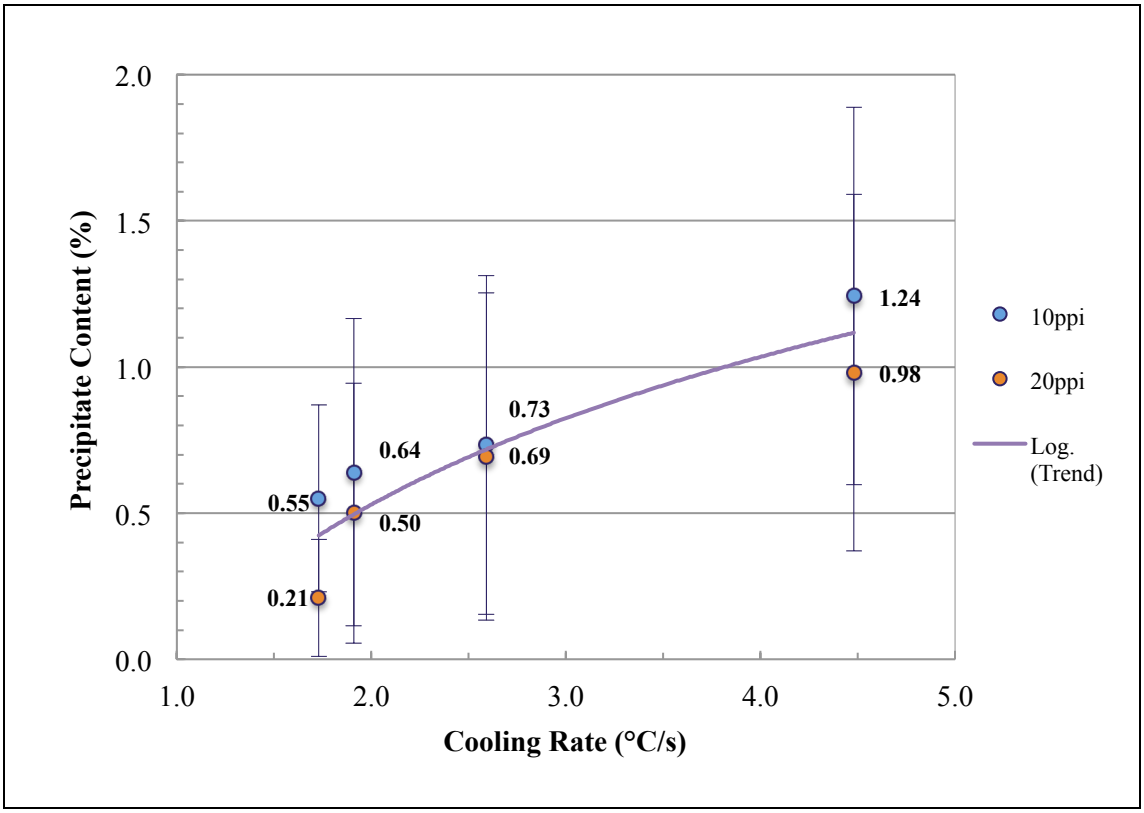

Figure 46 - Summary of the precipitate percentage values coming from the microstructural investigation on all samples (both 10 and 20 ppi filters tests). The precipitate content is related to the cooling rate.

The situation is even clearer viewing the graph in Figure 46. If the analysis of the eutectic fraction didn't revealed a clear dependence from the cooling conditions, now the situation is different and it's shown how the cooling rate has a main influence on the segregation phenomena, leading to the lamellar structures formation.
Regarding the average diameter of this precipitate, the trend is quite clear in this case too. The equivalent diameter decreases from 14.52 μm to 9.92 μm for the first series (Table 14) and it also decreases for the second series, starting from 10.84 μm up to 8.43 μm (Table 15).

Table 14 - Precipitate particles equivalent diameter measured in the castings produced using 10 ppi filters.

Step thickness (mm)	Average equivalent diameter (μm)	Standard deviation
20	14.52	3.42
15	13.34	3.11
10	12.01	3.09
5	9.92	2.85

The standard deviation values have an average decreasing trend, more pronounced for the 10 ppi castings.

Table 15 - Precipitate particles equivalent diameter measured in the castings produced using 20 ppi filters.

Step thickness (mm)	Average equivalent diameter (μm)	Standard deviation
20	10.84	2.24
15	9.78	2.42
10	8.63	2.35
5	8.43	2.18

The overall data are graphically reported in Figure 47, to confirm the considerations written above.

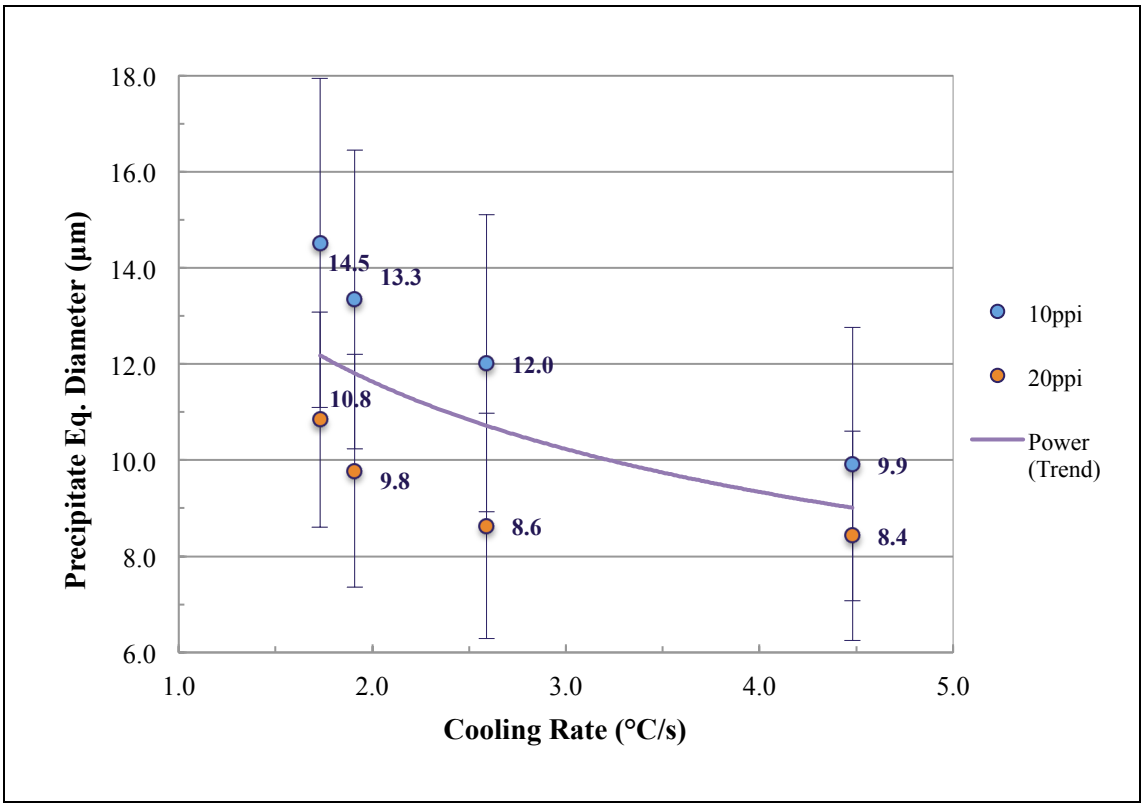

Figure 47 - Summary of the precipitate equivalent diameter analysis: both 10 and 20 ppi trials are considered. The equivalent diameter is related to the cooling rate.

Cooling conditions affect the precipitation of the lamellar compound (Figure 46), which has less time to grow by increasing the cooling rate (Figure 47).
The shape analysis of the segregations shows their irregularity, as the high roundness value revealed both the first series (Table 16) as well for the second one (Table 17).

Table 16 - Precipitate particles roundness resulting from the investigation on the 10 ppi tests castings.

Step thickness (mm)	Average precipitate roundness	Standard deviation
20	2.13	0.76
15	2.11	0.32
10	1.98	0.54
5	1.97	0.70

Values upper than 2 denote very articulated geometries, very far from looking like a circle (which corresponds to the value 1).

Table 17 - Precipitate particles roundness resulting from the investigation on the 20 ppi tests castings.

Step thickness (mm)	Average precipitate roundness	Standard deviation
20	1.96	0.60
15	2.10	0.60
10	1.98	0.69
5	2.04	0.65

Looking at the graphical representation (Figure 48) it can be seen that the lamellar precipitate's morphology is irregular independently from the cooling conditions, keeping the average value around 2.

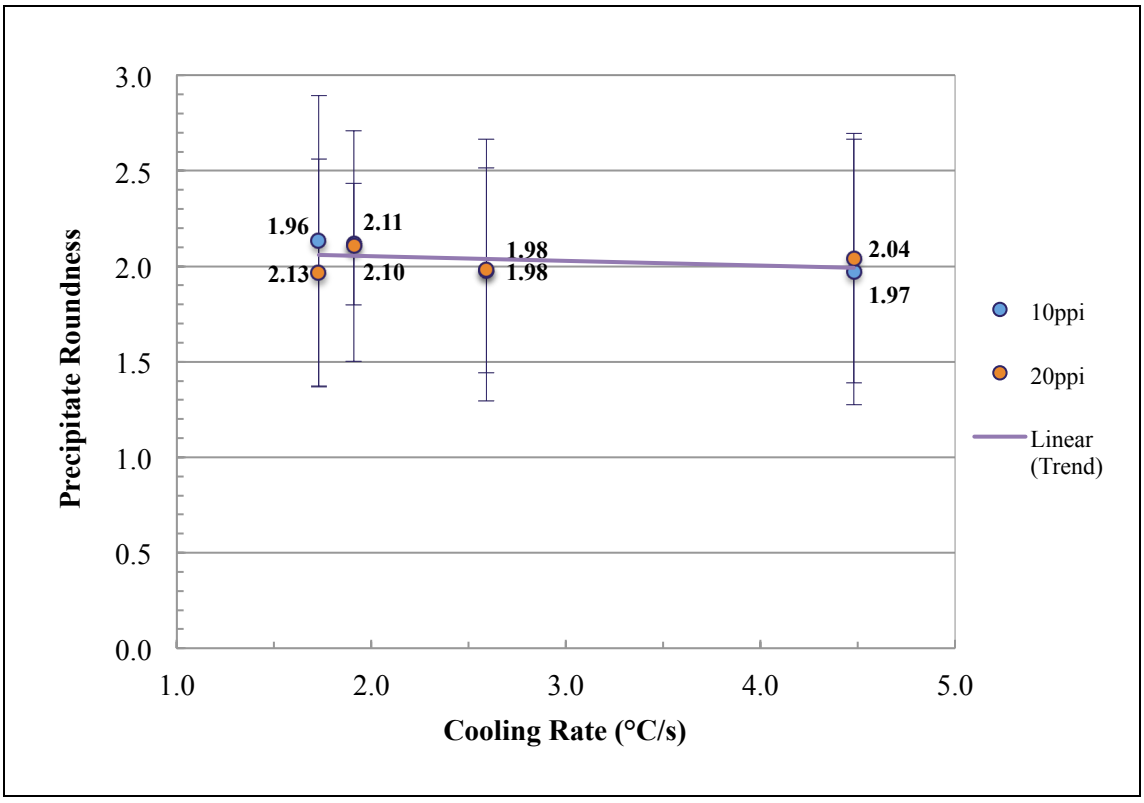

Figure 48 - Summary of the precipitate roundness analysis on both 10 and 20 ppi trials. The roundness is related to the cooling rate.

Considering the precipitate aspect ratio, the values retrieved by the shape analysis (reported in Table 18 and Table 19) confirm what was observed with the optical microscope, i.e. these precipitates preferentially assume an elongated shape.

Table 18 - Precipitate particles aspect ratio regarding the castings produced using 10 ppi filters.

Step thickness (mm)	Average precipitate aspect ratio	Standard deviation
20	1.98	0.44
15	1.77	0.33
10	1.90	0.60
5	1.91	0.55

Table 19 - Precipitate particles aspect ratio regarding the castings produced using 20 ppi filters.

Step thickness (mm)	Average precipitate aspect ratio	Standard deviation
20	2.15	0.77
15	2.04	0.72
10	2.02	0.65
5	1.98	0.66

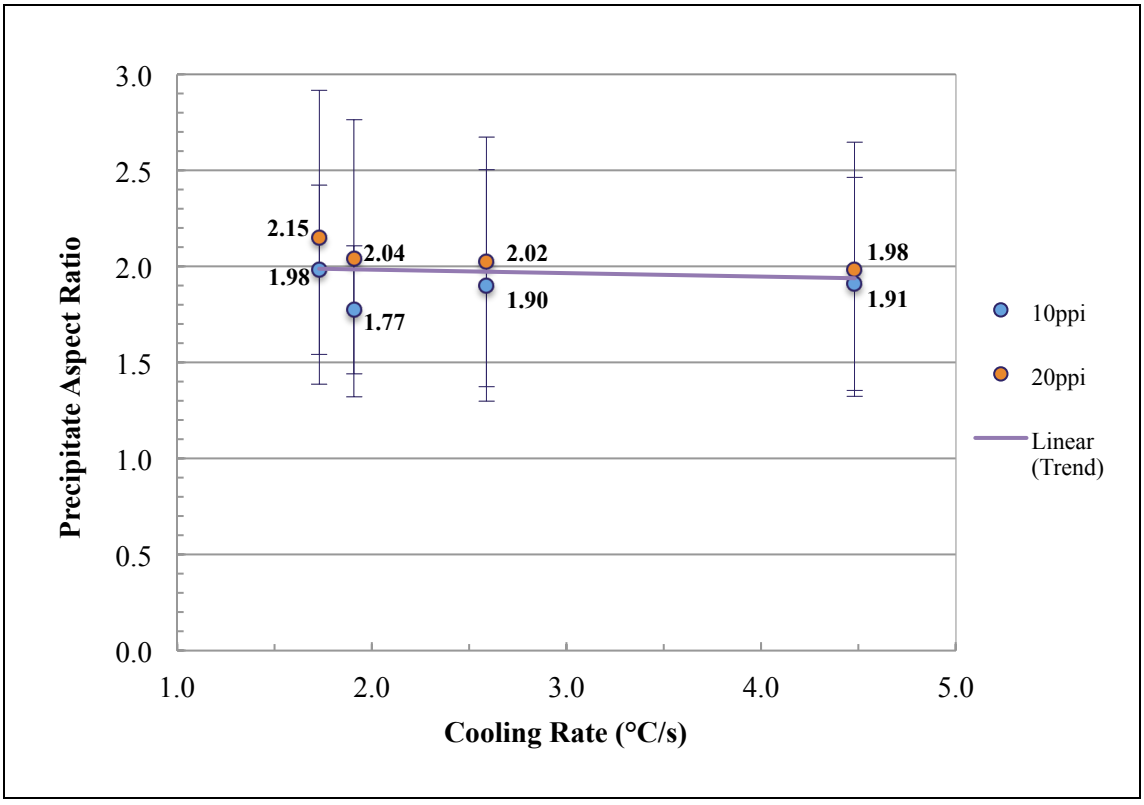

Figure 49 - Summary of the results coming from the aspect ratio evaluation on all samples.

As well as for the roundness, also the aspect ratio values don't show a dependence of this parameter by the cooling conditions, as visible in Figure 49.

Intermetallic Compound

Regarding the Al-Mn intermetallic compound, and in particular the percentage fraction, Table 21 and Table 22 report the average values coming from the metallographic analysis. The intermetallic fraction is generally small if compared with other structures like eutectic or the lamellar precipitate. Both series present measured values that are in the around of 0.1%, with a more or less marked decreasing trend.

Table 20 - Intermetallic content detected in the castings produced using 10 ppi ceramic foam filters.

Step thickness (mm)	Average intermetallic content (%)	Standard deviation
20	0.15	0.12
15	0.17	0.13
10	0.17	0.10
5	0.11	0.08

The standard deviations even seem small but if associated with the content values becomes clear that the intermetallic compounds are not uniformly distributed, as observed during the optical investigation.

Table 21 - Intermetallic content detected in the castings produced using 20 ppi ceramic foam filters.

Step thickness (mm)	Average intermetallic content (%)	Standard deviation
20	0.10	0.08
15	0.09	0.06
10	0.09	0.08
5	0.08	0.06

The Figure 50 provides a graphical illustration of the relationship between the intermetallic compound's content and the cooling rate.

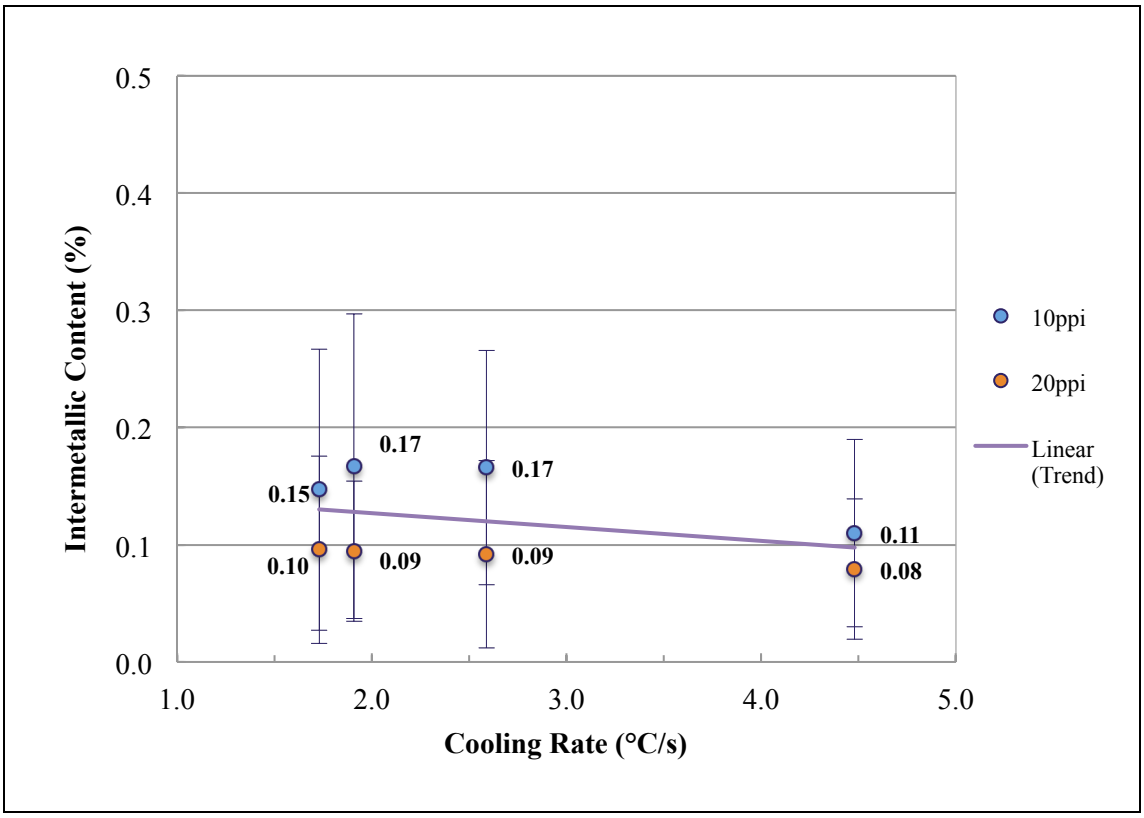

Figure 50 - Summary of the intermetallic fraction values coming from the microstructural investigation on all samples (both 10 and 20 ppi filters tests). The intermetallic content is related to the cooling rate.

But it's even more pronounced the influence of the cooling conditions on the intermetallic average diameter: for the castings produced using the 10 ppi filters the calculated diameter is 7.99 µm, referring to the thicker step, and decreases with the thickness up to 4.87 µm (Table 22).

Table 22 - Intermetallic particles equivalent diameter measured in the castings produced using 10 ppi filters.

Step thickness (mm)	Average equivalent diameter (µm)	Standard deviation
20	7.99	1.79
15	6.04	2.29
10	5.88	2.17
5	4.87	0.68

In a similar way, analysing the castings obtained by making the use of 20 ppi filters, the equivalent diameter values have a decreasing trend from 6.52 µm to 4.94 µm (Table 23).

Table 23 - Intermetallic particles equivalent diameter measured in the castings produced using 20 ppi filters.

Step thickness (mm)	Average equivalent diameter (µm)	Standard deviation
20	6.52	2.86
15	5.86	2.46
10	5.55	2.13
5	4.94	1.48

Also the standard deviations are on average decreasing while increasing the cooling rate, and this means that shorter solidification times produce more similar intermetallic compounds (about the size). Figure 51 presents a summary view of this analysis.

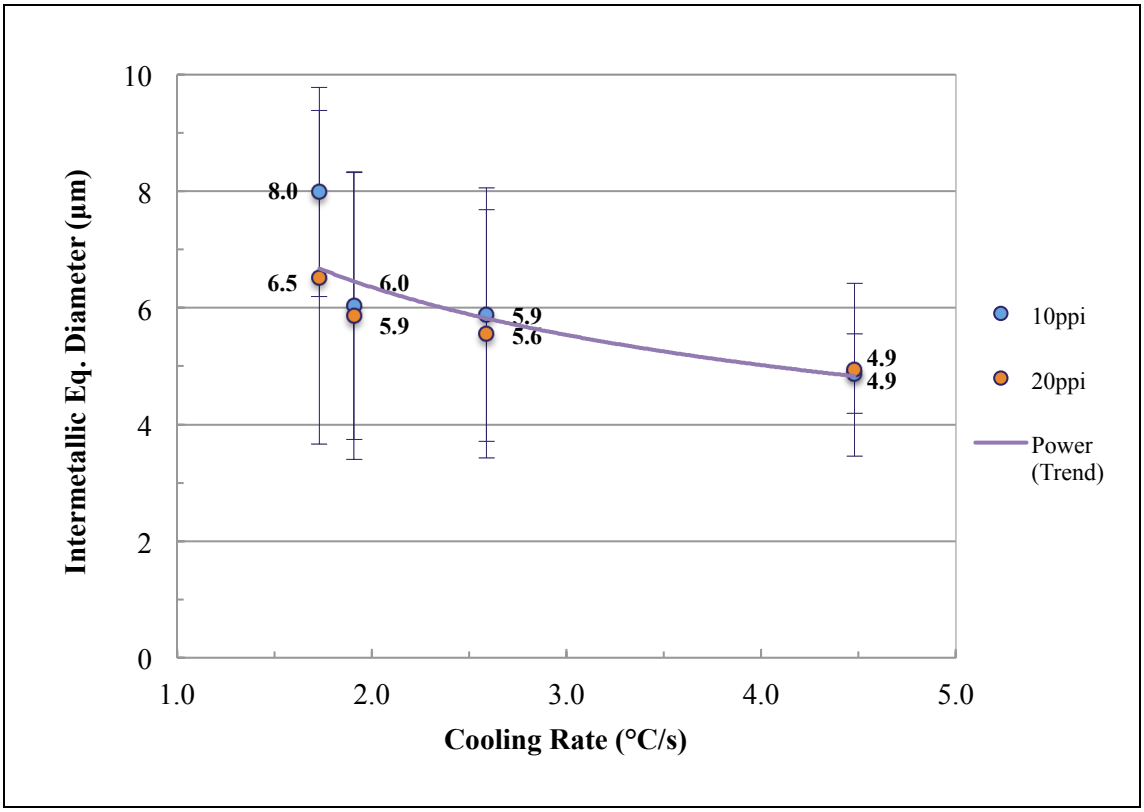

Figure 51 - Summary of the intermetallic compound equivalent diameter analysis: both 10 and 20 ppi trials are considered. The equivalent diameter is related to the cooling rate.

Approaching the intermetallic compound's shape, the roundness parameter values (Table 24 and Table 25) haven't a trend useful to establish relations with the cooling conditions, but it can be noticed that these values often exceed 3. Evaluating also the standard deviations, the overall data corroborate what observed during the experimental investigations: this is an irregular and inhomogeneous compound.

Table 24 - Intermetallic particles roundness resulting from the investigation on the 10 ppi tests castings.

Step thickness (mm)	Average intermetallic roundness	Standard deviation
20	3.40	0.58
15	2.78	0.79
10	3.40	0.58
5	2.82	0.72

Table 25 - Intermetallic particles roundness resulting from the investigation on the 20 ppi tests castings.

Step thickness (mm)	Average intermetallic roundness	Standard deviation
20	2.32	0.55
15	2.55	0.40
10	2.73	0.45
5	2.58	0.47

Looking at the chart in Figure 52, it's therefore difficult to assign a trend to the collected data.

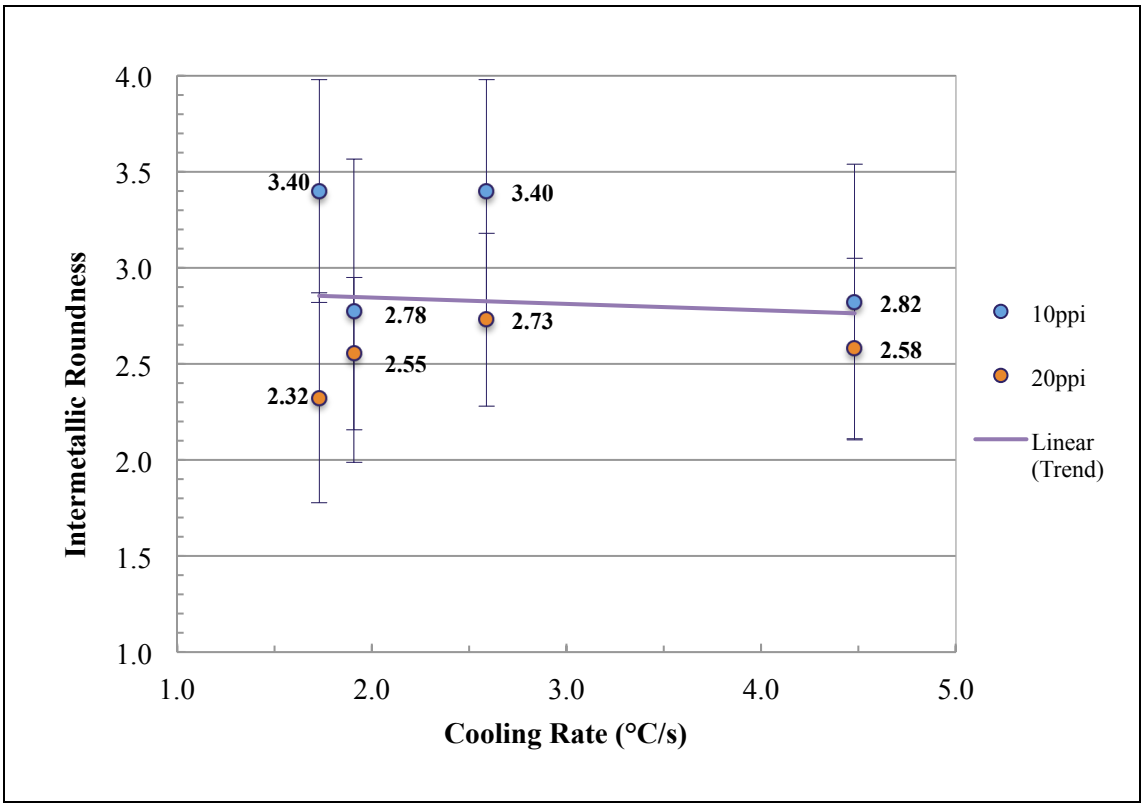

Figure 52 - Summary of the intermetallic compound roundness analysis on both 10 and 20 ppi trials. The roundness is related to the cooling rate.

The results coming from the analysis of the aspect ratio are more delineated. Considering both the casting campaigns, the calculated parameter's value is almost always greater than 2 (Table 26 and Table 27).

Table 26 - Intermetallic particles aspect ratio regarding the castings produced using 10 ppi filters.

Step thickness (mm)	Average intermetallic aspect ratio	Standard deviation
20	2.06	0.79
15	2.06	0.65
10	2.30	0.97
5	2.06	0.80

Analysing only the second series data, it's evident a growing with the cooling rate (Table 27).

Table 27 - Intermetallic particles aspect ratio regarding the castings produced using 20 ppi filters.

Step thickness (mm)	Average intermetallic aspect ratio	Standard deviation
20	1.92	0.51
15	2.18	0.86
10	2.21	0.84
5	2.36	1.01

The accumulative trend, considering both the series, is increasing too with the cooling rate, as visible in Figure 53, and it denotes the formation of intermetallic increasingly irregular moving towards more drastic cooling conditions.

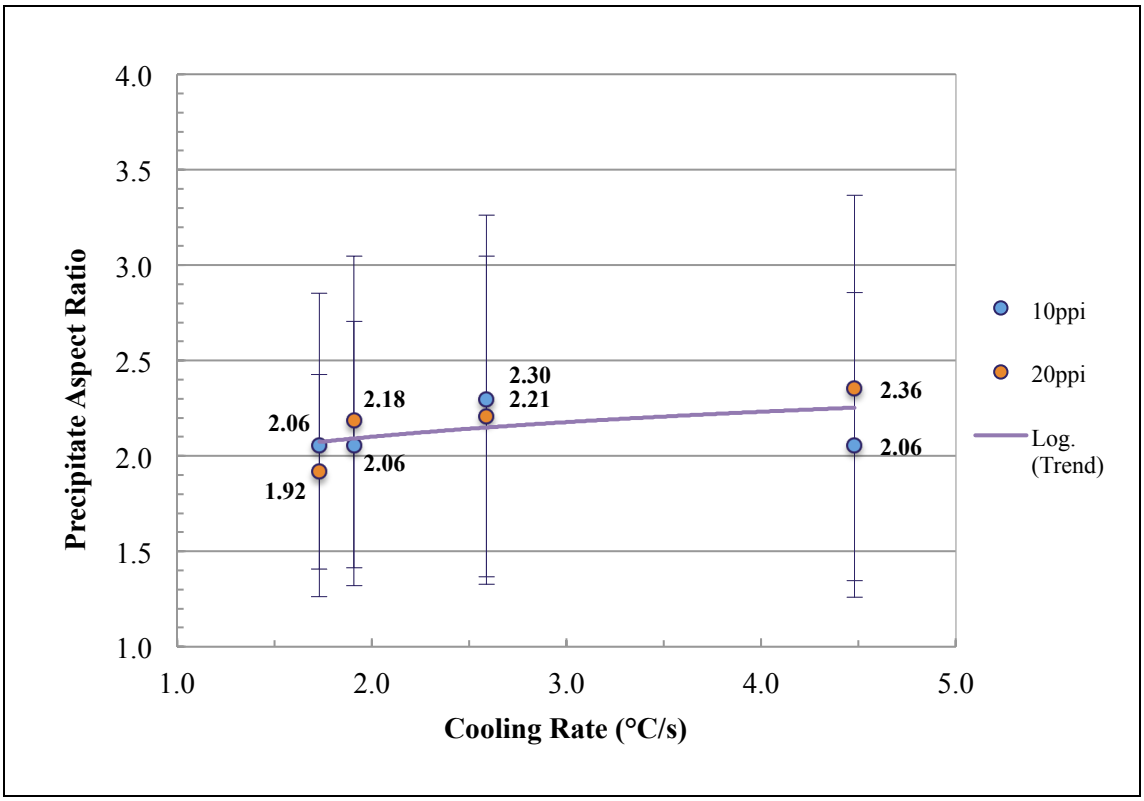

Figure 53 - Summary of the results coming from the aspect ratio evaluation on all samples.

Grain Analysis

The experimental activity's results exposure continues with the grain analysis executed on the 12 step castings previously reserved for such investigations. The first 6 castings analysed were those produced during the initial casting campaign. The average grain diameter calculated on each step are reported in Table 28.

Table 28 - Equivalent grain size measured in the castings produced using 10 ppi filters.

Step thickness (mm)	Average grain diameter (μm)	Standard deviation
20	100.00	28.35
15	89.30	24.35
10	75.71	19.62
5	65.90	17.75

The obtained values, for the 10 ppi filters trials, are between 65.90 μm and 100.00 μm, and the related standard deviations grow too with the step thickness, from 17.75 to 28.35; also the average grain diameter measured on the second trials has the same trend (Table 29), increasing from 59.50 μm to 91.65 μm with the thickness (decreasing the cooling rate), and in this case too the standard deviation is lower in the thinnest step (16.03) and higher in the thicker one (22.61).

Table 29 - Equivalent grain size measured in the castings produced using 20 ppi filters.

Step thickness (mm)	Average grain diameter (μm)	Standard deviation
20	91.62	22.61
15	76.22	19.23
10	66.43	18.33
5	59.50	16.03

These data allow to draw the chart reported in Figure 54, that represents the equivalent grain size as a function of the cooling rate.

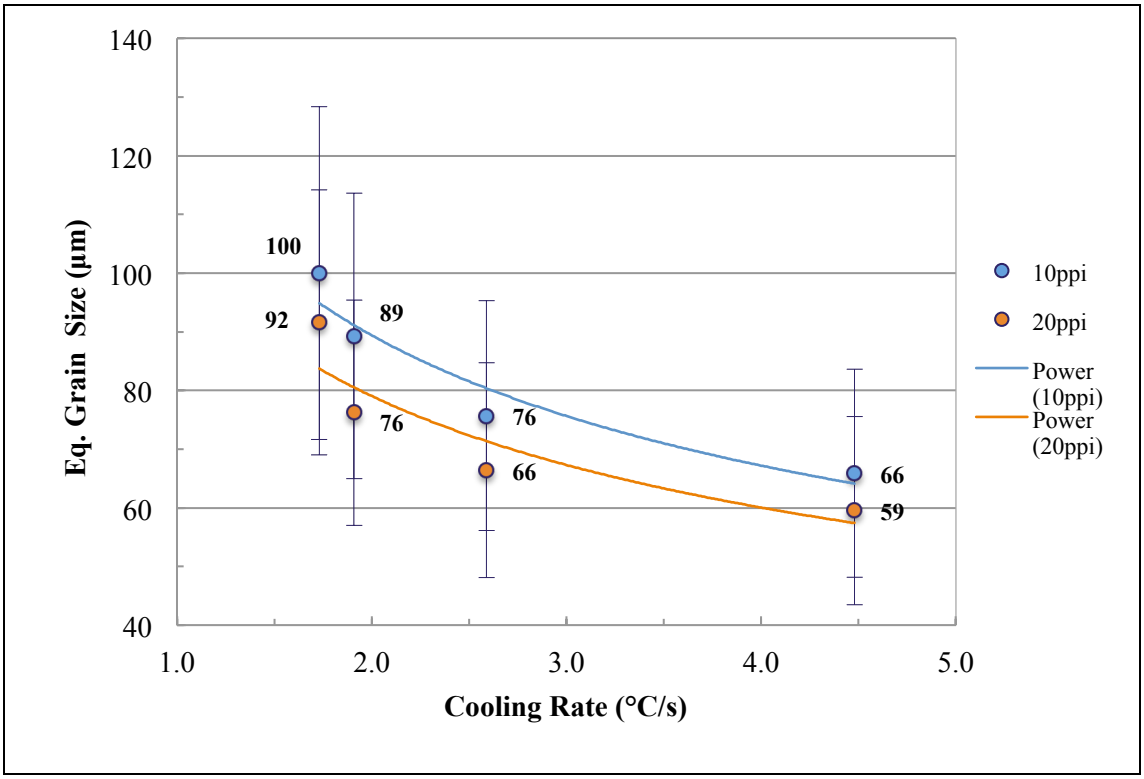

Figure 54 - Equivalent grain size determination results: diameter values are related to cooling conditions.

For these cooling rates, relatively low if compared with the HPDC ones, the DAS can be taken as the equivalent grain size; since the DAS can be related to the cooling rate by a power law, as suggested by Flemings [56], it's possible to draw a trend of this type in the chart above, as highlighted in blue (10 ppi series) and in orange (20 ppi series). The equations describing these curves can be defined, as it will be illustrated later, and allow to predict the equivalent grain size by knowing only the cooling conditions.
Considering now the grain's shape, the related analysis didn't provide data having a well defined trend, as already seen in the case of the intermetallic compound. Table 30 reports the grain's roundness as revealed on the first series, and Table 31 the second series related values.

Table 30 - Grain roundness resulting from the investigation on the 10 ppi tests castings.

Step thickness (mm)	Average grain roundness	Standard deviation
20	1.89	0.49
15	1.65	0.34
10	1.76	0.38
5	1.76	0.40

Table 31 - Grain roundness resulting from the investigation on the 20 ppi tests castings.

Step thickness (mm)	Average grain roundness	Standard deviation
20	1.56	0.32
15	1.54	0.37
10	1.63	0.36
5	1.66	0.36

These data's graphical representation (Figure 55) lets suppose that these cooling rates don't significantly affect the grain's morphology.

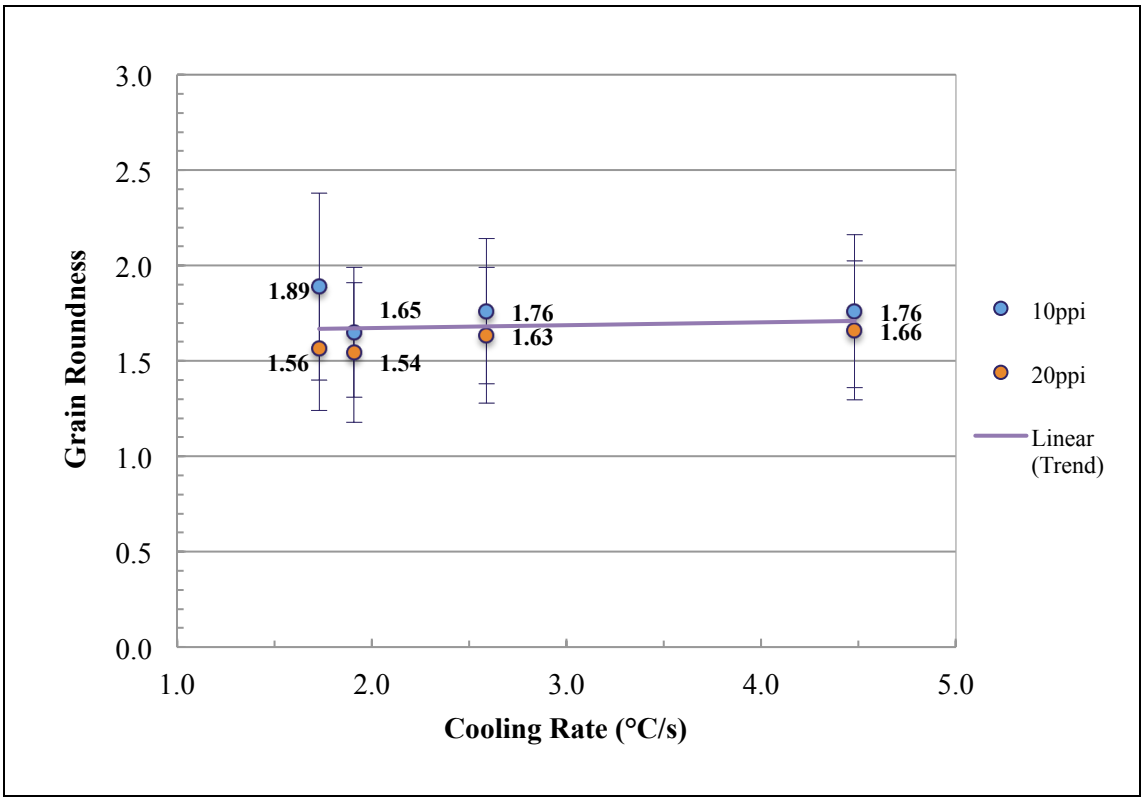

Figure 55 - Summary of grain roundness analysis on both 10 and 20 ppi trials. The roundness is related to the cooling rate.

This assumption is supported by the aspect ratio investigation's results. The first series analysis gave values in the range 1.56÷1.71 (Table 32), the second campaign's castings provided grain's aspect ratio values between 1.53 and 1.59 (Table 33).

Table 32 - Grain aspect ratio regarding the castings produced using 10 ppi filters.

Step thickness (mm)	Average grain aspect ratio	Standard deviation
20	1.71	0.39
15	1.56	0.38
10	1.61	0.30
5	1.58	0.32

Table 33 - Grain aspect ratio regarding the castings produced using 20 ppi filters.

Step thickness (mm)	Average grain aspect ratio	Standard deviation
20	1.53	0.34
15	1.55	0.35
10	1.59	0.38
5	1.53	0.34

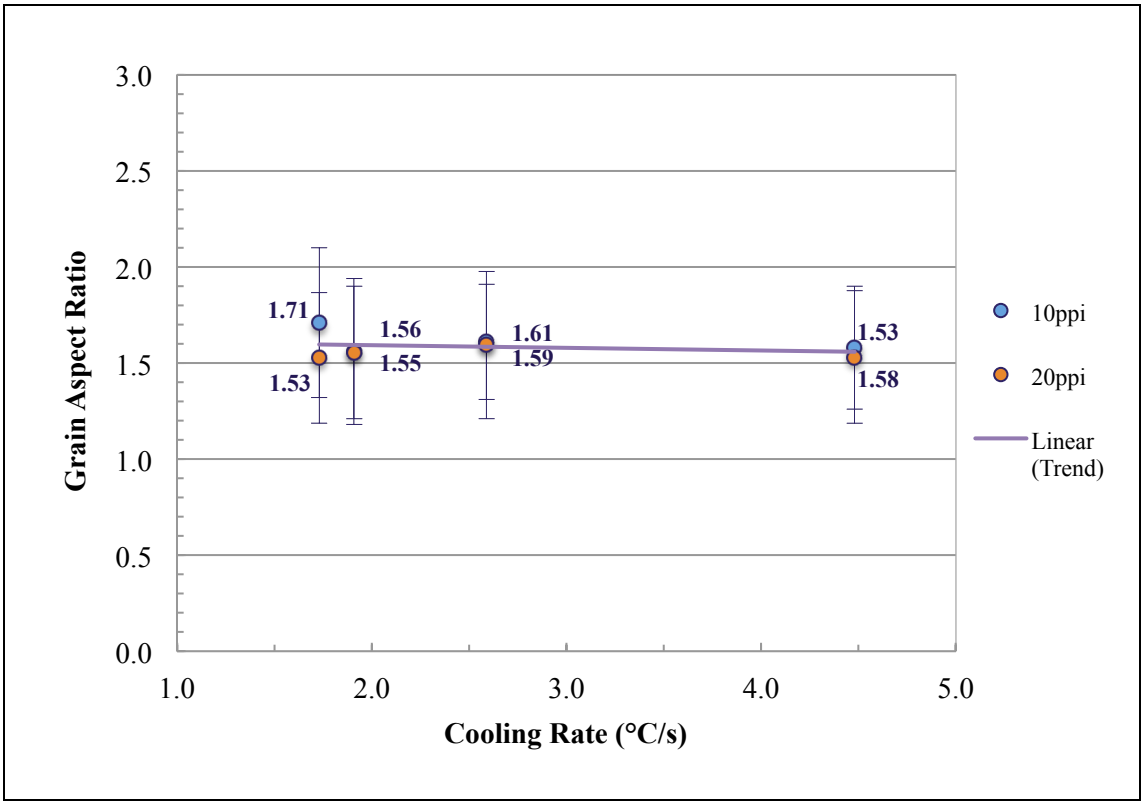

Figure 56 - Summary of the results coming from the grain aspect ratio evaluation on all samples.

The overall acquired data, contemplating 12 castings, show even better the low influence of the cooling rates on this parameter (Figure 56).

Mechanical Properties

The mechanical properties analysis aims to estimate the average values of the ultimate tensile strength for the different thickness steps, and then to compare these values to find a relationship with the cooling conditions; the same analysis has been performed also considering the yield tensile strength and the percentage elongation. Furthermore, to verify the reliability of the obtained results, in addition to the average values it has been reported also the average standard deviations. Firstly, the ultimate tensile strength analysis results are exposed.

Ultimate Tensile Strength

The UTS values related to the castings produced by using the 10 ppi filters are reported in Table 34.

Table 34 - Ultimate tensile strength resulting from the investigation on the 10 ppi tests castings.

Step thickness (mm)	Average ultimate tensile strength (MPa)	Standard deviation
20	170	8.73
15	172	9.76
10	176	19.38
5	-	-

The UTS values, for this first casting campaign, are between 170 MPa and 176 MPa. The tests executed on the tensile specimens obtained from the thinnest steps (5 mm) didn't provide useful data because of premature breaking, probably due to excessive oxide skins presence into the thinnest steps, the nearest to the filter and so more subjected to contamination originated by impurities not properly entrapped into the filter. Higher standard deviation value for the UTS, related to the tests on the 10 mm steps, supports this hypothesis. Graphical representation of the overall results, regarding the first series, are reported in Figure 57.

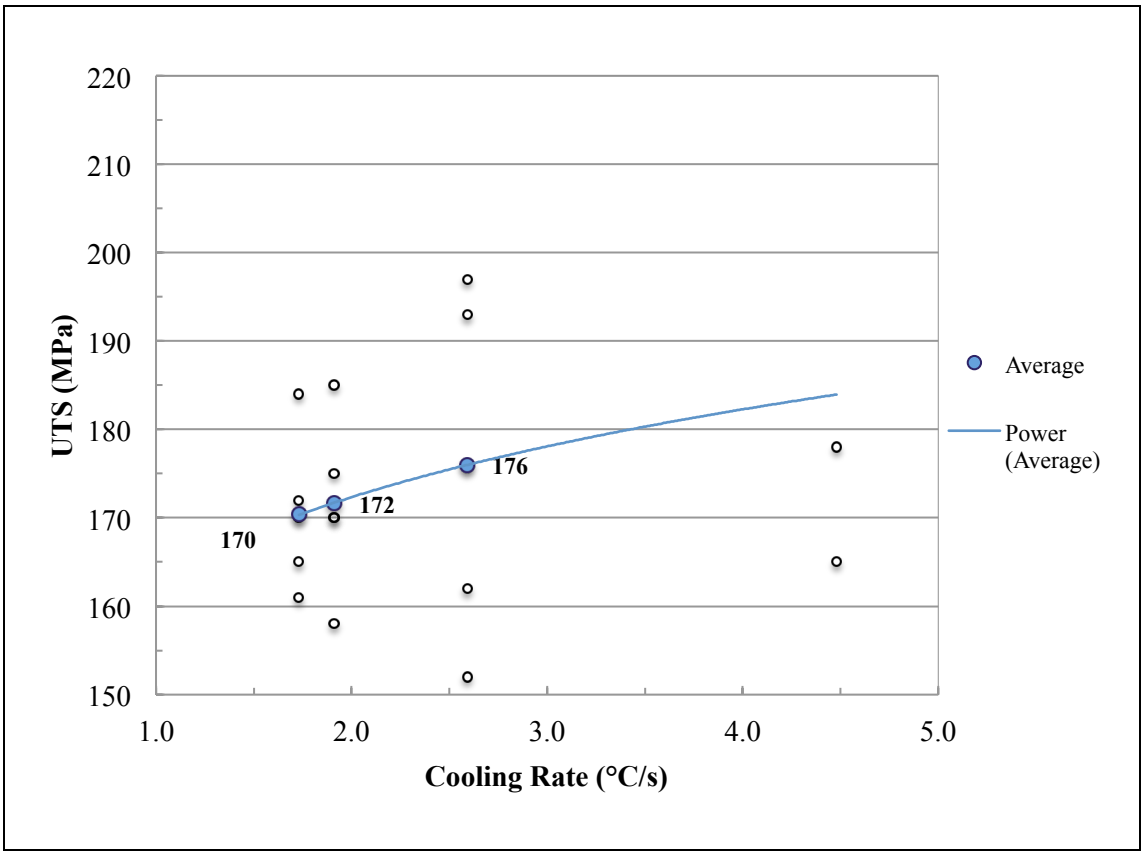

Figure 57 - Ultimate tensile strength values for the castings produced using the 10 ppi filters.

It has been chosen to represent the UTS resulting values with individual dots, instead of adopting only the average values and the standard deviations, to better describe the dispersion of the data in correspondence of the lower steps, i.e. the closest to the filter. The blue dots denote the average values and the blue curve the related trend.
The analysis executed on the castings obtained during the second campaign, using the denser mesh filters, led to the UTS results listed in Table 35.

Table 35 - Ultimate tensile strength resulting from the investigation on the 20 ppi tests castings.

Step thickness (mm)	Average ultimate tensile strength (MPa)	Standard deviation
20	187	8.84
15	192	8.27
10	200	6.10
5	202	5.92

The first noticeable aspect is that the UTS values obtained by the tests on the second campaign castings are higher (between 187 MPa and 202 MPa) than those seen

previously (Table 34), and this is a first confirmation that a finer mesh filter significantly contributes to produce sound castings. Another observation can be done on the standard deviations: in this second case the deviation values decrease with the increasing of the UTS values, and this means that the UTS results related to the thinnest steps are closer, and therefore more reliable than the ones related to the first series. It is clearly visible in the chart in Figure 58 where, as before, all the obtained values are plotted, and not only the average ones.

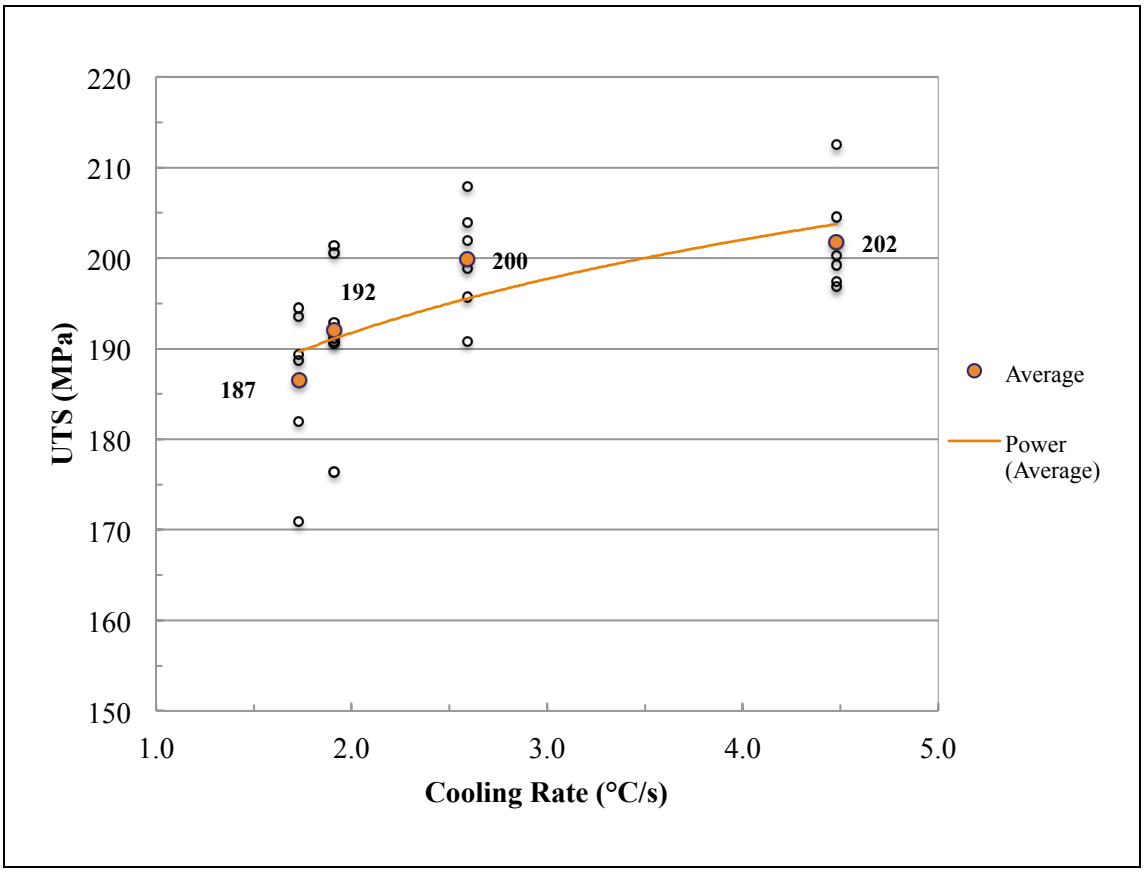

Figure 58 - Ultimate tensile strength values for the castings produced using the 20 ppi filters.

The average UTS values for these trials are shown by the orange points, for different cooling conditions, and the trend is highlighted by the orange curve.

Tensile Yield Strength

Regarding the tensile yield strength analysis, the resulting values are specified in Table 36 for the first castings, and in Table 37 for the second series.

Table 36 - Tensile yield strength resulting from the investigation on the 10 ppi tests castings.

Step thickness (mm)	Average tensile yield strength (MPa)	Standard deviation
20	70	6.06
15	72	2.07
10	74	2.55
5	79	2.59

The tests executed on the tensile specimens, obtained from the first casting campaign castings, led to TYS values between 70 MPa and 79 MPa, as visible in Figure 59.

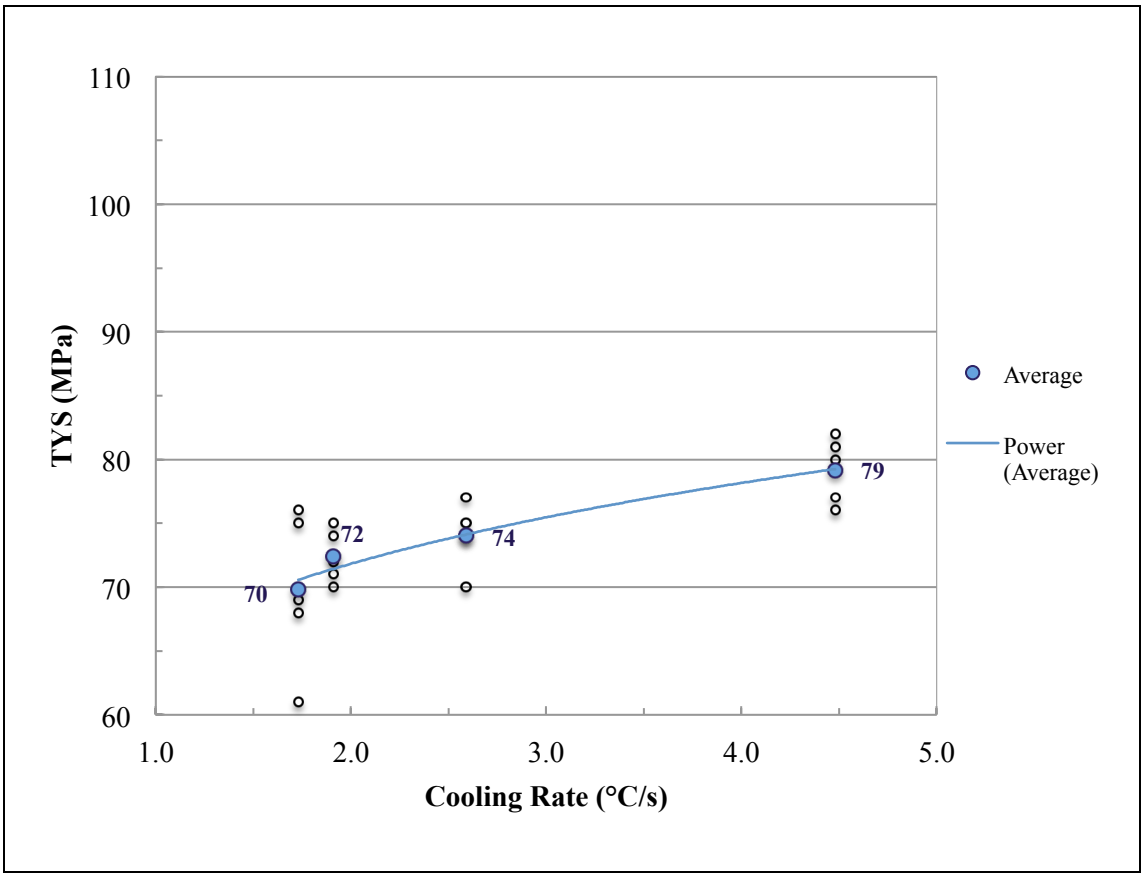

Figure 59 - Tensile yield strength values relative to the castings produced using the 10 ppi filters.

As for the UTS value, also for the TYS values all the data are reported into the chart, and the blue point stand for the average values for each thickness. The blue curve represents the TYS values trend varying the cooling rate.
The results coming from the tests on the specimens retrieved from the castings produced by using the 20 ppi filters are listed in Table 37.

Table 37 - Tensile yield strength resulting from the investigation on the 20 ppi tests castings.

Step thickness (mm)	Average tensile yield strength (MPa)	Standard deviation
20	93	2.97
15	96	1.72
10	99	3.39
5	101	4.34

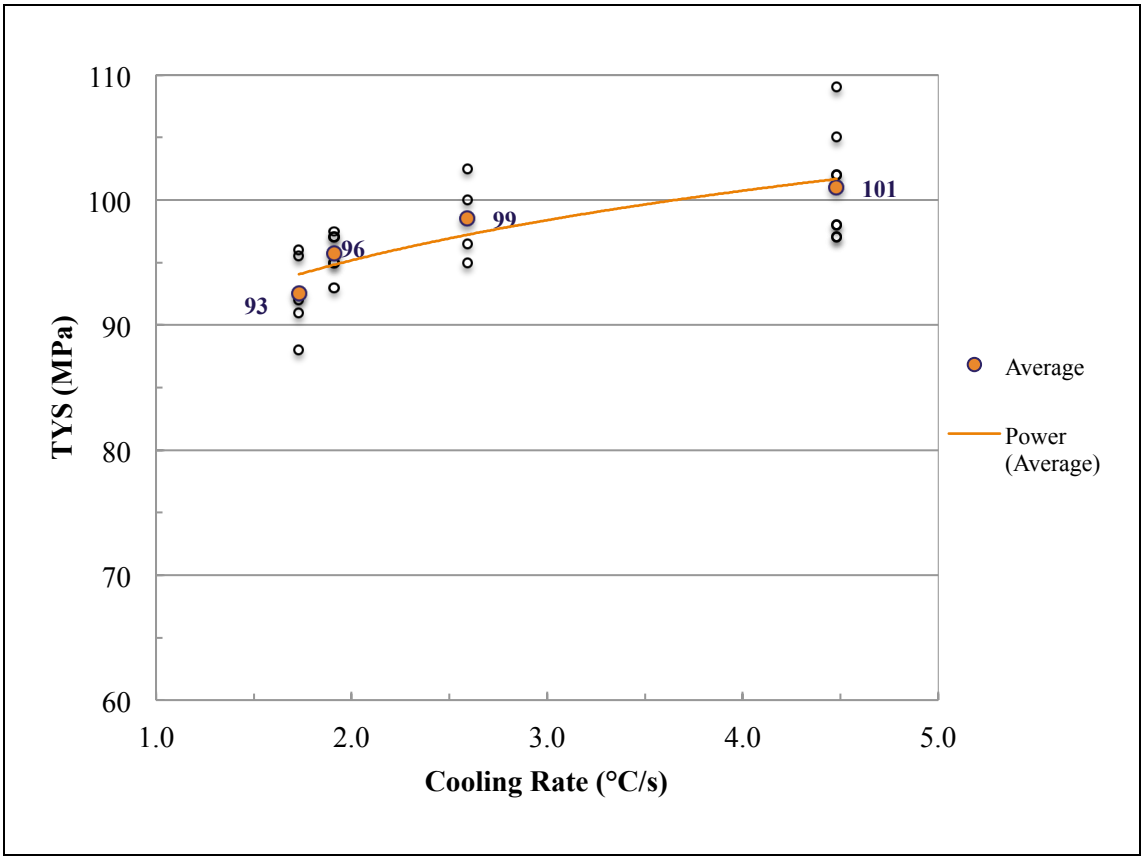

Figure 60 - Tensile yield strength values relative to the castings produced using the 10 ppi filters.

In this case, the average TYS is between 93 MPa and 101 MPa, as indicated by the orange dots in Figure 60. Finally, the standard deviation values are tiny for both the series and this confirms the reliability of the calculated TYS values.

Percentage Elongation

The tests which has just discussed have allowed also to derive data referred to the elongation to fracture for the analysed specimens. The average elongation values, for the first casting series, are reported in Table 38.

Table 38 - Elongation to fracture regarding the castings obtained by using 10 ppi filters.

Step thickness (mm)	Average elongation (%)	Standard deviation
20	5.3	0.86
15	5.5	0.68
10	6.0	1.25
5	-	-

For the first casting campaign, the elongation values are between 5.3 % and 6.0 %. The related standard deviations are significant (up to 1.25) when compared to the elongation values. These results are schematically drawn in Figure 61, where it can be noticed the great dispersion of the data.

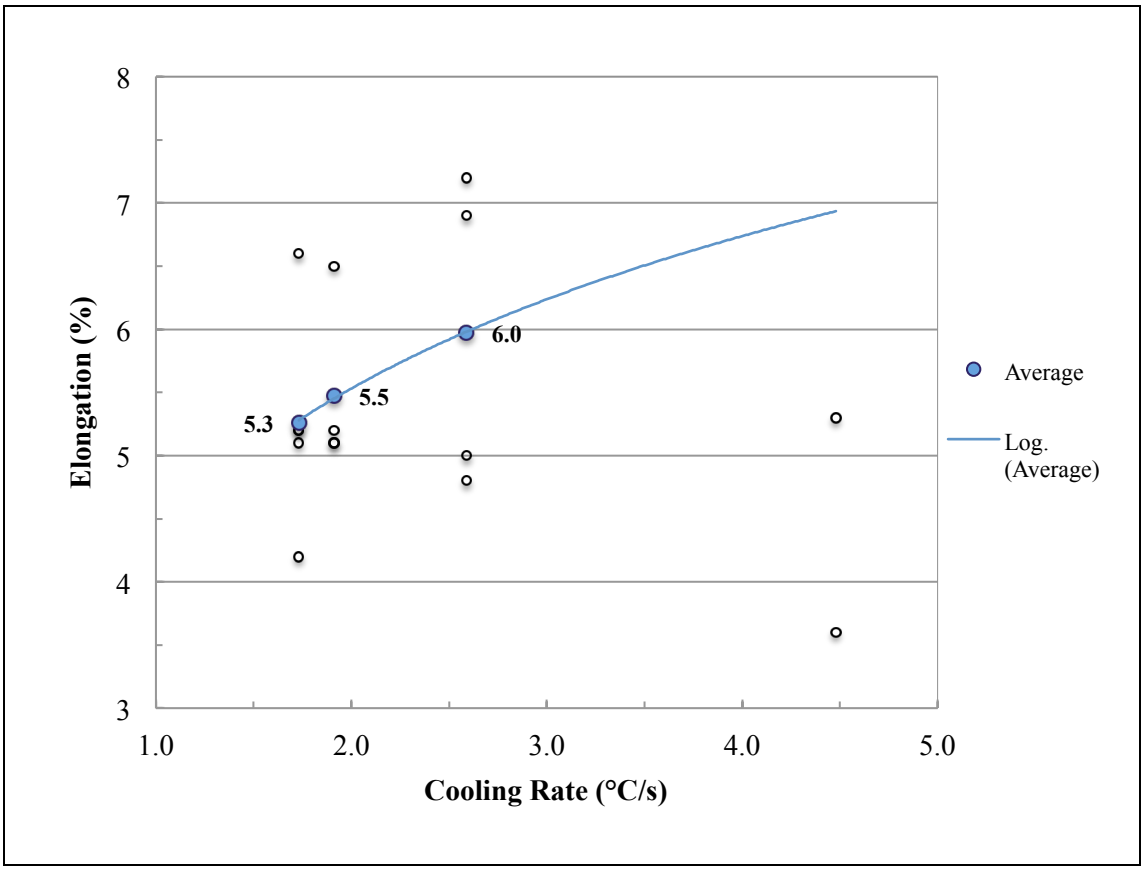

Figure 61 - Summary of percentage elongation for the castings produced using 10 ppi filters.

The values of the maximum elongation to rupture, coming from the analysis of the castings produced by using the 20 ppi filters, are listed in Table 39.

Table 39 - Elongation to fracture regarding the castings obtained by using 20 ppi filters.

Step thickness (mm)	Average elongation (%)	Standard deviation
20	4.5	0.39
15	4.6	0.48
10	4.9	0.65
5	5.1	0.76

For this series the average elongation values are between 4.5 % and 5.1 %, associated to small standard deviations (from 0.39 to 0.76). Figure 62 shows these data and the related trend while varying the cooling conditions.

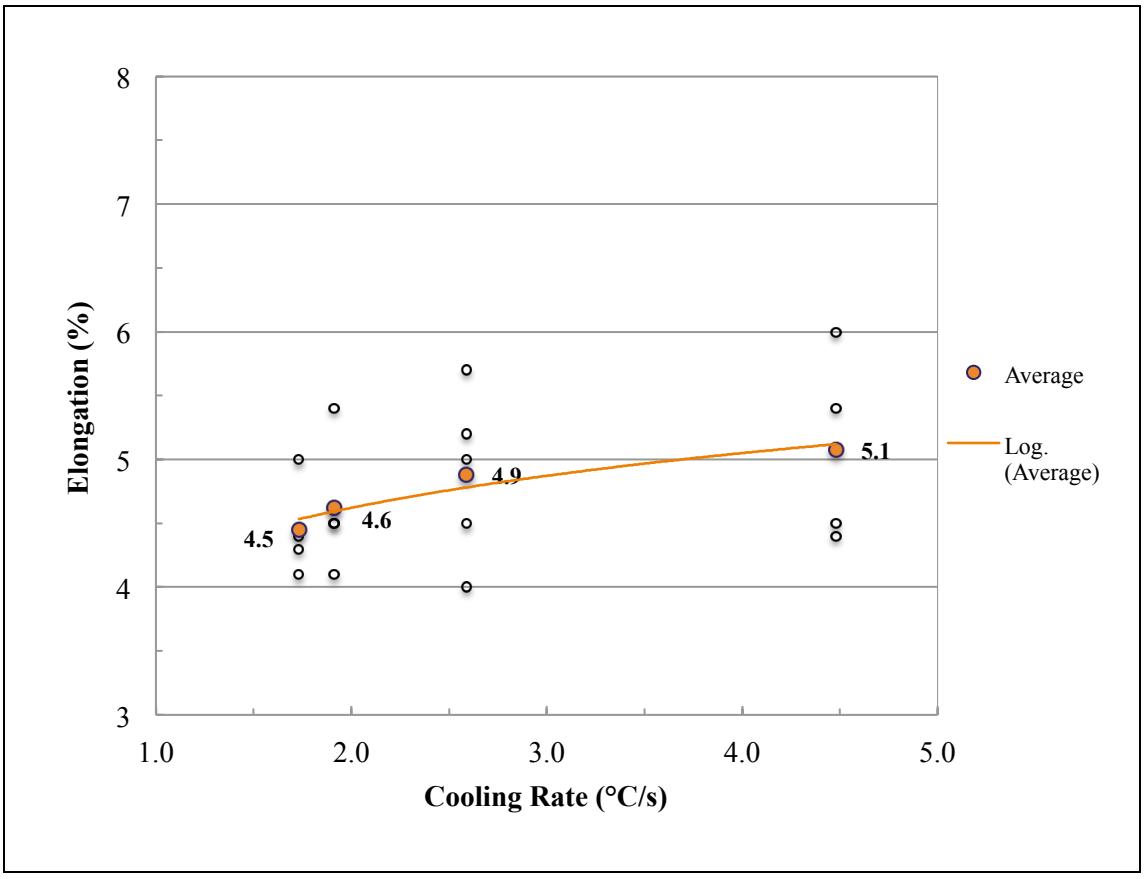

Figure 62 - Summary of percentage elongation for the castings produced using 20 ppi filters.

Expressly, for both the graphs (Figure 61 and Figure 62) has been maintained the same scale for the y-axis to highlight the different "inclination" of the two series' trends. If the first castings provided elongation data more increasing with the cooling rate than the second series, it's true the same that the standard deviations associated to the second campaign castings are smaller than the ones related to the first series, letting suppose more accurate results.

Discussion

With the aim of investigating the relations occurring between the process parameters and the castings' final properties, some correlations can be studied. Now will be considered the results coming from the study of the second campaign castings, produced by using a denser mesh filters to ensure a more efficient impurities retention. These castings have generally reported better mechanical properties if compared with the ones obtained during the first trial.

Correlation between Process Parameters and Resulting Microstructure

In Figure 63 it is reported the trend of the average grain size as function of the cooling rate.

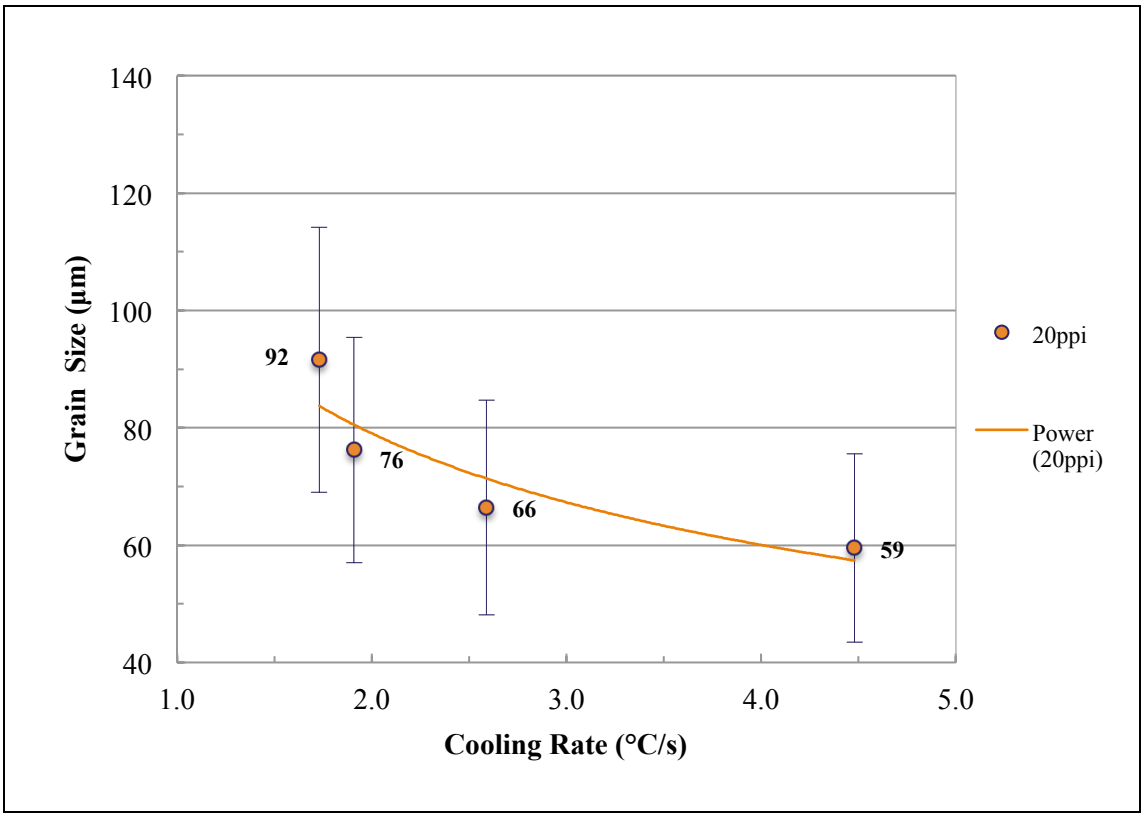

Figure 63 - Equivalent grain size, related to the cooling conditions, for the second campaign castings.

As suggested by Flemings [56], the dendrite arm spacing (DAS) can be related to the cooling rate (CR) by the following equation:

$$DAS = a*(CR)^{-n} \quad (1)$$

Since the DAS can be taken as the equivalent grain size, the cooling rate and the grain size results coming from the microstructural analysis can be correlated, making

possible to define the coefficients *a* and *n* in the (1) by looking for an exponential relation. The equation describing the power trend curve in Figure 63 is:

$$y = 104*(x)^{-0.4} \quad (2)$$

This leads to estimate the grain size (d) by knowing the cooling rate (CR), as following:

$$d = 104*(CR)^{-0.4} \quad (3)$$

Correlation between Microstructure and Final Mechanical Properties

It is now appropriate to treat the inverse of the square of the grain size (indicated with the letter *d* in Figure 64) and the tensile yield strength, and looking for a relationship of the Hall-Petch type:

$$TYS = YS_0 + k*d^{-½} \quad (4)$$

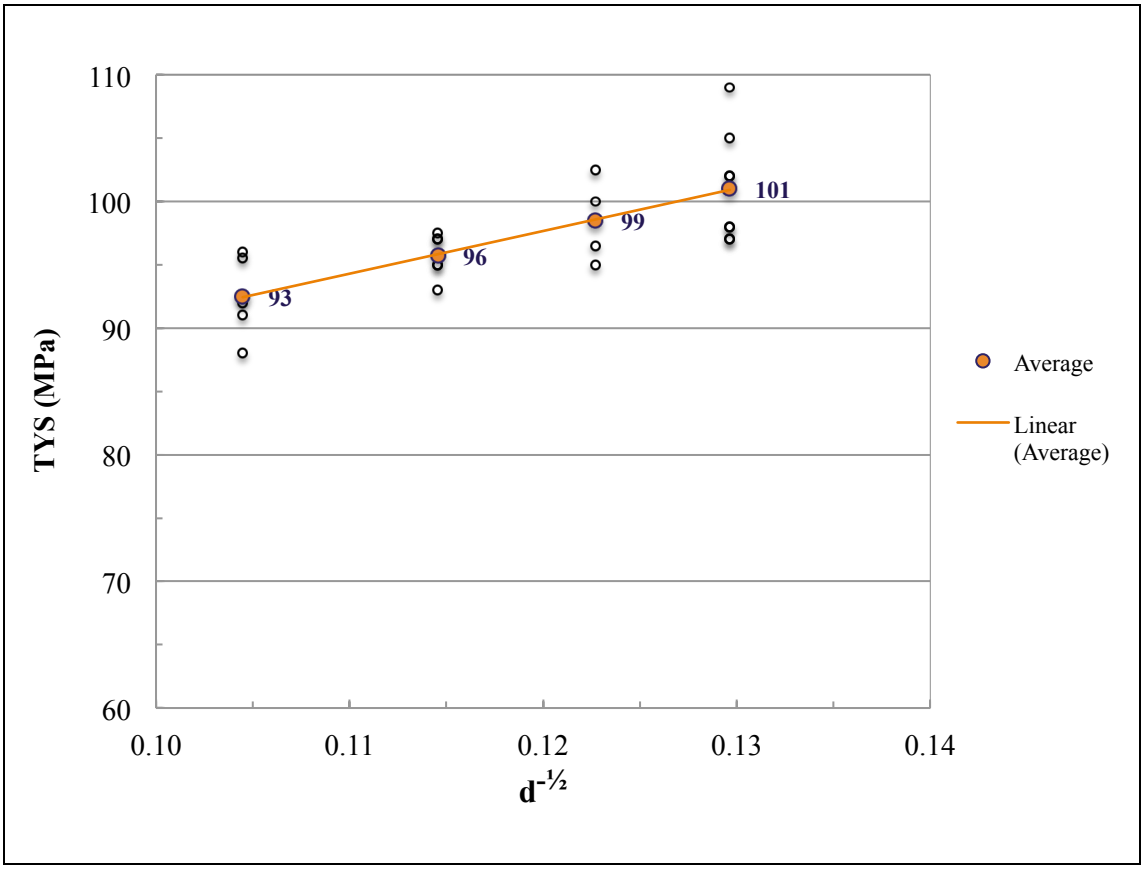

Figure 64 - Tensile yield strength as function of the grain size, considering the second casting campaign.

Calculating the equation associated to the orange linear trend highlighted in Figure 64, the YS_0 and k coefficients can be definite too:

$$TYS = 57.2 + 337*(d)^{-½} \quad (5)$$

Correlation between Process Parameters and Final Mechanical Properties

So, TYS can be related to grain size by the well known Hall-Petch law (4):

$$TYS = YS_0 + k*d^{-½} \quad (4)$$

where d is the equivalent grain size, related by Flemings (1) to the cooling rate as:

$$d = DAS = a*(CR)^{-n} \quad (1)$$

The result is that TYS can be estimated by knowing only the cooling conditions, and the specific relation valid for the alloy studied in this work is:

$$TYS = 57.2 + 337*(104*CR^{-0.4})^{-½} \quad (6)$$

Considering the theoretical laws mentioned above, as well as the experimental results coming from this study, a semi-empirical model for predicting the final mechanical properties of AM60B alloys can thus be established.

Conclusions

Static tensile tests have been carried out on AM60B magnesium alloy specimens obtained from reference steps castings, produced by gravity die casting process. Numerical simulation of the overall casting process have been performed to design an optimised mould, to minimise the defects' content and to potentially produce sound magnesium alloy castings. Microstructural investigations have been executed on these castings, to analyse the relations with the final mechanical properties. Based on the results obtained in the present study, the following conclusions can be drawn:

- Using thermal field data coming from the simulation, it's possible to reliably predict the castings' final properties.
- Prediction reliability can be achieved with a controlled amount of defects, and the numerical simulation of the casting process contributes to the identification of criticisms and optimal variables.
- Tensile yield strength, ultimate tensile strength and elongation values resulting from the tensile tests are according to literature for the alloy considered: this confirms the castings' soundness and consequently the innovative mould goodness.
- Mechanical properties have been related to microstructural ones.
- Combining the casting process numerical simulation results with the empirical ones it is possible to setup a semi-empirical model to predict the castings' final properties.
- The laboratory scale casting equipment showed its reliability and the obtained results can be easily extended to the industrial scale.
- The model, as a predicting tool, can be extended to more complex geometries.
- An operating protocol to predict the castings' final properties has been established, and it can be employed also with similar alloys commonly used in industries.

References

1) International Magnesium Association Statistics (2012), IMA, Virginia, USA.
2) S. SCHUMANN and H. FRIEDRICH, The Use of Magnesium in Cars - Today and in the Future, Werkstroff Informationsgesellschaft, Frankfurt (1998), pp.3-13.
3) H. FRIEDRICH and S. SCHUMANN, Research for a "New Age of Magnesium" in the Automotive industry. J.Mater.Process.Technol. 117 (2001), p.276.
4) E. OHSHIMA, Application of Die Cast Magnesium to AVCC. International Magnesium Association, IMA, Proceedings of Annual World Magnesium Conference, Japan (1996), pp.1-16.
5) T.K. AUNE, D.L. ALBRIGHT and H. WESTENGEN, Properties of Die Cast Magnesium Alloys of Varying Aluminium Content. SAE 900792 (1990).
6) T.K. AUNE, D.L. ALBRIGHT, O. ORJASAETER and O.K. NERDAHL, Elements of the Fatigue Process in Magnesium Die Casting Alloys. TMS, Proceedings of Magnesium Technology, USA (2000), pp.319-323.
7) T.K. AUNE and H. WESTENGEN, High Performance Die Castings - Utilising Magnesium's Properties. Magnesium Alloys and their Applications, K.U. Kainer (Ed). Wiley-WCH Weinheim, Germany (2000), pp.540-547.
8) T.K. AUNE, H. WESTENGEN and T. RUDEN, Mechanical Properties of Energy Absorbing Magnesium Alloys. SAE 930418 (1993).
9) M.H. MAJ and T.N. MEYER, Ultra-Large Castings of Aluminum and Magnesium, Ford Motor Company, USA (2005).
10) J.F. KING, Development of Practical High Temperature Magnesium Casting Alloys. Magnesium Alloys and their Applications, K.U. Kainer (Ed). Wiley-VCH Weinheim, Germany (2000), pp.14-22.
11) A. ANTONACI, Analisi delle Caratteristiche e delle Possibilità Applicative di Leghe di Magnesio, Trento (2003).
12) M. KASCHEL and A. BOCKHORN, Magnesium Industry and Applications, Presentation Husky (2008).
13) D. COLOMBO, Metallurgia dei Metalli non Ferrosi, Trento (2001).
14) E.J. VINARCIK, High Integrity Die Casting Processes. Springer, USA (2003), p.67.
15) Y.C. LEE, A.K. DAHLE and D.H. STJOHN, Grain Refinement of Magnesium. H.I. Kaplan, J.N. Hryn and B.B. Clow (Eds). TMS, Proceedings of Magnesium Technology, Pennsylvania, USA (2000), pp.211-218.
16) A. BECK, The Technology of Magnesium and its Alloys. FA Hughes & Co. Ltd, London, UK (1940).
17) M. FLEMINGS, R. MARTINEZ, A. FIGUEREDO and J.A. YURKO, Metal Alloy Compositions and Process. United States Patent no.6645323 (2003).
18) I.J. POLMEAR, Light Alloys: Metallurgy of Light Metals. Halsted Press (1996), p.88.
19) B.L. MORDIKE and T. EBERT, Magnesium: Properties, Application, Potential. Mater.Sci.Eng.A 302 (2001), pp.37-45.
20) M. LESSITER, Casting in Action. Engineered Casting Solutions, Winter (1999), p.55.
21) A. STEVENSON, Selection and Application of Magnesium and Magnesium Alloys. ASM Handbook 2, ASTM Publication, USA (1995).

22) K. WEISS and C. HONSEL, Influence of Physical Data and Cooling Conditions on the Solidification in Mg Die Castings. TMS, Proceedings of Magnesium Technology (2003), pp.109-114.
23) F. BONOLLO and G. TIMELLI, Modelling Microstructure, Defects & Properties. Proceedings of 12th International Summer School - Light Alloy Castings: from Innovative Design to Advanced Applications, Vicenza, Italy (2011).
24) R. SHIBATA, T. KANEUCHI, T. SOUDA and Y. LIZUKA, New Semi Solid Metal Casting Process. Proceedings of 4th.Int.Conf. Semi-Solid Processing of Alloys and Composites, England (1996), pp.296-300.
25) D. APELIAN, Semi-Solid Processing Routes and Microstructure Evolution. Proceedings of 7th.Int.Conf. Semi-Solid Processing of Alloys and Composites, Japan (2002), pp.25-30.
26) S.E. LEBEAU, M.W. WALUKAS and R.F. DECKER, Semi-Solid Processing of Magnesium Alloy Components., Proceedings of 61st.Annual.World.Magn.Conf., USA (2004).
27) F. CZERWINSKI, The Basics of Modern Semi-solid Metal Processing. J.Min.Met.Mater.Soc. 58 (2006), pp.17-20.
28) D. DOUTRE, J. LANGLAIS and S. ROY, Process for Semi-Solid Forming. Alcan International Ltd, Proceedings of 8th.Int.Conf. SemiSolid Processing of Alloys and Composites, Cyprus (2004).
29) F. CZERWINSKI, Semisolid Processing - Origin of Magnesium Molding. Magnesium Injection Molding. Springer Verlag, USA (2008), pp.81-148.
30) F. CZERWINSKI, Fundamentals of Semisolid Magnesium Molding. J.Met. 60 (2008), p.83.
31) D.H. KIRKWOOD, M. SUERY, P. KAPRANOS and K.P. YOUNG, Semi-solid Processing of Alloys. Springer, USA (2010), p.96.
32) Z. FAN, Semisolid Metal Processing. Int.Mat.Rev. 47 (2002).
33) Q. HAN, E.A. KENIK, S.R. AGNEW and S. VISWANATHAN, Solidification Behavior of Commercial Magnesium Alloys. Metals & Materials Society The Minerals, Proceedings of Magnesium Technology (2001).
34) D.H. STJOHN, A.K. DAHLE, T. ABBOTT, M.D. NAVE and M. QIAN, Solidification of Cast Magnesium Alloys. Metals & Materials Society The Minerals, Proceedings of Magnesium Technology (2003).
35) F. BONOLLO, G. TIMELLI, G. MAZZACAVALLO and R. MOLINA, AIM, Proceedings of Convegno Nazionale AIM, Vicenza (2004).
36) F. GROSSELLE, G. TIMELLI, F. BONOLLO, A. TIZIANI and E. DELLA CORTE, Correlation Between MIicrostructure and Mechanical Properties of Al-Si Cast Alloys. La Metallurgia Italiana 6/2009 (2009), pp.25-32.
37) N. FACCHINELLI, G. TIMELLI and L. TREVISAN, Optimizing a Step Casting Geometry to Evaluate the Mechanical Properties of AM60B Magnesium Alloys. Proceedings of EnginSoft International Conference 2011, Verona, Italy (2011).
38) N. FACCHINELLI, G. TIMELLI and L. TREVISAN, Optimization of a Step Casting Die Geometry to Evaluate the Potential Mechanical Performance of AM60B Magnesium Alloys. Proceedings of 5th International Conference High Tech Die Casting, Vicenza, Italy (2012).
39) F. BONOLLO and S. ODORIZZI, Numerical Simulation of Foundry Processes. S.G.E., Padua, Italy (2001).
40) J. RUNYORO, S.M. BOUTORABI and J. CAMPBELL, Critical Gate Velocity for Film Forming Casting Alloys. AFS Trans. 37 (1992), pp.225-239.
41) J. CAMPBELL, Castings. Elsevier, UK (2003).

42) K.D. CARLSON and C. BECKERMANN, Prediction of Shrinkage Pore Volume Fraction Using a Dimensionless Niyama Criterion. Met.Mater.Trans.A 40A (2009), pp.163-175.
43) M. JOLLY, Prof. John Campbell's Ten Rules for Making Reliable Castings. J.Met. (2005), pp.19-28.
44) F.Y. HSU, M. JOLLY and J. CAMPBELL, The Design of L-Shaped Runners for Gravity Casting. Metals & Materials Society The Minerals, Proceedings of Shape Casting: 2nd International Symposium, Orlando, FL, USA (2007).
45) A. ZADEH and J. CAMPBELL, Metal Flow Through a Filter System. AFS Trans. 2 (2002), pp.1-17.
46) J. CAMPBELL, Casting Practice: The 10 Rules of Castings. Elsevier, UK (2004).
47) ASM International, Casting, ASM Metals Handbook 15. Ohio, USA (1998).
48) G. CHADHA, J.E. ALLISON and J.W. JONES, The Role of Microstructure and Porosity in Ductility of Die Cast AM50 and AM60 Magnesium Alloys. Metals & Materials Society The Minerals, Proceedings of Magnesium Technology (2004).
49) E. AGHION, B. BRONFIN and D. ELLEZER, The Role of Magnesium Industry in Protecting Environment. J.Mater.Process.Technol. 117 (2001), pp.381-385.
50) ASTM, Standard Test Methods for Tension Testing of Metallic Materials. E 8M – 04. ASTM International, 100 Barr Harbor Drive, PO Box C700, West Conshohocken, PA 19428-2959, United States
51) S.K. ISKANDER, R.K. NANSTAD, S. VISWANATHAN, R.L. SWAIN and J.F. WALLACE, Fracture Toughness of Magnesium Alloy AM60B. H.I. Kaplan, J.N. Hryn and B.B. Clow, The Minerals, Metals & Materials Society, Proceedings of Magnesium Technology 2000, Nashville, Tennessee, USA (2000).
52) H.E. FRIEDRICH and B.L. MORDIKE, Magnesium Technology: Metallurgy, Design Data, Applications. Springer, Berlin, Germany (2006).
53) Magnesium. K.U. Kainer, Wiley-VCH, Proceedings of 7th International Conference on Magnesium Alloys and Their Applications, Dresden, Germany (2006).
54) Y.W. RIDDLE, L.P. BARBER and M.M. MAKHLOUF, Characterization of Mg Alloy Solidification and As-Cast Microstructures. Metals & Materials Society The Minerals, Proceedings of Magnesium Technology (2004).
55) H. PROFFITT, Magnesium and Magnesium Alloys. ASM Handbook 15, ASTM Publication, USA (1996).
56) M.C. FLEMINGS, Solidification Processing. McGraw-Hill, New York, London and Sydney (1974).

Appendix - List of Publications

1) G. TIMELLI, N. FACCHINELLI, A. TIZIANI, Processi di Colata allo Stato Semisolido di Leghe di Magnesio, Parte 1 - Rassegna delle Tecnologie di Formatura, In Conference Proceedings of 33th Convegno Nazionale AIM, Brescia (2010).

2) G. TIMELLI, N. FACCHINELLI, A. TIZIANI, Processi di Colata allo Stato Semisolido di Leghe di Magnesio, Parte 2 - Caratteristiche Microstrutturali e Difettologiche, In Conference Proceedings of 33th Convegno Nazionale AIM, Brescia (2010).

3) N. FACCHINELLI, Improvements in Production Processes and Microstructural Characteristics of Magnesium Alloys Components, In Conference Proceedings of 12th International Summer School on Aluminium Alloy Technology, Light Alloys Casting: from Innovative Design to Advanced Applications, DTG, Vicenza (2011).

4) N. FACCHINELLI, G. TIMELLI, L. TREVISAN, Optimizing a Step Casting Geometry to Evaluate the Mechanical Properties of AM60B Magnesium Alloys, In Conference Proceedings of EnginSoft International Conference 2011, CAE Technologies for Industry, Verona (2011).

5) N. FACCHINELLI, G. TIMELLI, L. TREVISAN, Optimization of a Step Casting Die Geometry to Evaluate the Potential Mechanical Performance of AM60B Magnesium Alloys, In Conference Proceedings of 5th International Conference High Tech Die Casting, AIM, Vicenza (2012).

6) N. FACCHINELLI, F. BONOLLO, G. TIMELLI, G. MUNERATTI, L. TREVISAN, Correlation Between Numerical Simulation Results and Empirical Ones in Permanent Mould Gravity Casting of AM60B Magnesium Alloys, In Conference Proceedings of EnginSoft International Conference 2012, CAE Technologies for Industry, Lazise-Verona (2012).